A Selection of published/presented papers

Volume V (1)
(2008)

Papers 1-11

S Lee

A Selection of published/presented papers
Volume IV Part 1
(2008)
S Lee

1 Pinch current limitation effect in plasma focus (This version includes an Erratum)
S. Lee and S. H. Saw, Appl. Phys. Lett. 92, 021503 (2008), DOI:10.1063/1.2827579

2 Neutron Scaling Laws from Numerical Experiments (This version includes an Erratum)
S Lee and S H Saw, J of Fusion Energy, 27 292-295 (2008) DOI: 10.1007/s10894-008-9132-7
published first online 20 February 2008 at **http://dx.doi.org/10.1007/s10894-008-9132-7**

3 Numerical Experiments on Plasma Focus Pinch Current Limitation
S Lee, P Lee, S H Saw and R S Rawat, Plasma Phys. Control. Fusion 50 (2008) 065012
available at **http://stacks.iop.org/0741-3335/50/065012.**

4 Computing Plasma Focus Pinch Current from Total Current Measurement
S. Lee, S. H. Saw, P. C. K. Lee, R. S. Rawat and H. Schmidt, Appl Phys Letters 92, 111501 (2008) DOI:10.1063/1.2899632

5 Current and Neutron Scaling for Megajoule Plasma Focus Machines
S Lee, Plasma Phys. Control. Fusion, 50 (2008) 105005
available at http://stacks.iop.org/PPCF/50/105005

6 Research Results of Plasma Focus Numerical Experiments

S Lee & S H Saw, Keynote address delivered by S H Saw at International Workshop on Plasma Computations & Applications IWPCA2008, Kuala Lumpur, 14 July 2008

7 Results of the Internet-based Workshop on Plasma Focus Numerical Experiments
S Lee, Keynote address International Workshop on Plasma Computations & Applications IWPCA2008, Kuala Lumpur, 14 July 2008

8 Numerical Experiments on PF400 Neutron Yield
S Lee & S H Saw, delivered at International Workshop on Plasma Computations & Applications IWPCA2008, Kuala Lumpur, 14 July 2008

9 Compact sub-kilojoule range fast miniature plasma focus as portable neutron source
Rishi Verma, M V Roshan, F Malik, P Lee, S Lee, S V Springham, T L Tan, M Krishnan and R S Rawat, Plasma Sources Sci Technol 17 (2008) 045020

10 Order of magnitude enhancement with deuterium-krypton admixture operation in miniature plasma focus device
Rishi Verma, P Lee, S Lee, S V Springham, T L Tan, R S Rawat and M Krishnan
Appl Phys Lett 93, 101501 (2008)

11 11. Nano-phase titanium dioxide thin film deposited by repetitive plasma focus: Ion Irradiation and Annealing Based Phase Transformation and Agglomeration
R.S. Rawat, V. Aggarwal, M. Hassan, P. Lee, S.V. Springham, T.L. Tan and S. Lee Appl Surface Sci 255, pages 2932-2941 (2008)

Pinch current limitation effect in plasma focus

S. Lee[a)]
Nanyang Technological University, National Institute of Education, Singapore 637616 and INTI International University College, 71800 Nilai, Malaysia

S. H. Saw
INTI International University College, 71800 Nilai, Malaysia

(Received 8 November 2007; accepted 3 December 2007; published online 17 January 2008)

The Lee model couples the electrical circuit with plasma focus dynamics, thermodynamics, and radiation. It is used to design and simulate experiments. A beam-target mechanism is incorporated, resulting in realistic neutron yield scaling with pinch current and increasing its versatility for investigating all Mather-type machines. Recent runs indicate a previously unsuspected "pinch current limitation" effect. The pinch current does not increase beyond a certain value however low the static inductance is reduced to. The results indicate that decreasing the present static inductance of the PF1000 machine will neither increase the pinch current nor the neutron yield, contrary to expectations. © *2008 American Institute of Physics*. [DOI: 10.1063/1.2827579]

This model in its two-phase form was described in 1984.[1] It was used to assist in the design and interpretation of several experiments.[2–4] An improved five-phase model and code incorporating finite small disturbance speed,[5] radiation and radiation coupling with dynamics assisted several projects,[6–8] and was web published[9] in 2000 and in 2005.[10] Plasma self-absorption was included[9] in 2007. It has been used extensively as a complementary facility in several machines, for example, UNU/ICTP PFF,[2,6] the NX2,[7,8] NX1,[7] and DENA.[11] It has also been used[12] in other machines for design and interpretation including Soto's subkilojoule plasma focus machines,[13] FNII,[14] and the UBA hard x-ray source.[15] Information obtained from the model includes axial and radial velocities and dynamics,[1,7,12,11] soft x-ray (SXR) emission characteristics and yield,[5,7,8,16] design of machines,[13,16] optimization of machines, and adaptation to other machine types such as the Filippov-type DENA.[11] A study of speed-enhanced neutron yield[4,13] was also assisted by the model code.

A detailed description of the model is already available on the internet.[9,10] A recent development in the code is the inclusion of neutron yield using a phenomenological beam-target neutron generating mechanism,[17] incorporated in the present RADPFV5.13. A beam of fast deuteron ions is produced by diode action in a thin layer close to the anode, with plasma disruptions generating the necessary high voltages. The beam interacts with the hot dense plasma of the focus pinch column to produce the fusion neutrons. In this modeling, each factor contributing to the yield is estimated as a proportional quantity and the yield is obtained as an expression with proportionality constant. The yield is then calibrated against a known experimental point.

The beam-target yield is written in the form $Y_{b-t} \sim n_b n_i (r_p^2 z_p)(\sigma v_b)\tau$ where n_b is the number of beam ions per unit plasma volume, n_i is the ion density, r_p is the radius of the plasma pinch with length z_p, σ is the cross section of the D–D fusion reaction, n branch,[18] v_b is the beam ion speed, and τ is the beam-target interaction time assumed proportional to the confinement time of the plasma column.

Total beam energy is estimated[17] as proportional to $L_p I_{\text{pinch}}$,[2] a measure of the pinch inductance energy, L_p being the focus pinch inductance. Thus, the number of beam ions is $N_b \sim L_p I_{\text{pinch}}^2 / v_b^2$ and n_b is N_i divided by the focus pinch volume. Note that $L_p \sim \ln(b/r_p) z_p$, that[4] $\tau \sim r_p \sim z_p$, and that $v_b \sim U^{1/2}$ where U is the disruption-caused diode voltage.[17] Here, b is the cathode radius. We also assume reasonably that U is proportional to $V_{\max}$, the maximum voltage induced by the current sheet collapsing radially toward the axis.

Hence, we derive $$Y_{b-t} = C_n I_{\text{pinch}}^2 z_p^2 [(\ln b/r_p)] \sigma / V_{\max}^{1/2}, \quad (1)$$

where I_{pinch} is the current flowing through the pinch at start of the slow compression phase; r_p and z_p are the pinch dimensions at end of that phase. Here, C_n is a constant which, in practice, we will calibrate with an experimental point.

The D–D cross section is highly sensitive to the beam energy so it is necessary to use the appropriate range of beam energy to compute σ. The code computes $V_{\max}$ of the order of 20–50 kV. However, it is known[17] from experiments that the ion energy responsible for the beam-target neutrons is in the range of 50–150 keV,[17] and for smaller lower-voltage machines the relevant energy[19] could be lower at 30–60 keV. Thus, to align with experimental observations the D–D cross section σ is reasonably obtained by using beam energy equal to three times $V_{\max}$.

A plot of experimentally measured neutron yield Y_n vs I_{pinch} was made combining all available experimental data.[2,4,11,13,17,19–22] This gave a fit of $Y_n = 9 \times 10^{10} I_{\text{pinch}}^{3.8}$ for I_{pinch} in the range 0.1–1 MA. From this plot, a calibration point was chosen at 0.5 MA, $Y_n = 7 \times 10^9$ neutrons. The model code[23] RADPFV5.13 was thus calibrated to compute Y_{b-t} which in our model is the same as Y_n.

From experience, it is known that the current trace of the focus is one of the best indicators of gross performance. The axial and radial phase dynamics and the crucial energy transfer into the focus pinch are among the important information that is quickly apparent from the current trace. Numerical experiments were carried out for machines for which reliable current traces and neutron yields are available. Figure 1 shows a comparison of the computed total current trace

a)Electronic mail: leesing@optusnet.com.au.

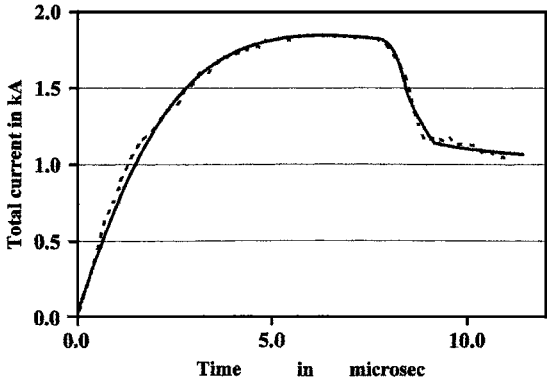

FIG. 1. PF1000 at 27 kV measured (dashed line) vs computed (smooth line) current traces.

(solid smooth line) with the experimental trace (dotted line) of the PF1000 at 27 kV (Ref. 17), 3.5 torr deuterium, with outer/inner radii $b=16$ cm, $a=11.55$ cm, and anode length $z_o=60$ cm. In the numerical experiments we fitted external (or static) inductance $L_o=33$ nH and stray resistance $r_o=6$ mΩ with model parameters mass factor, current factor, and radial mass factor as $f_m=0.14$, $f_c=0.7$, and $f_{mr}=0.35$. The computed current trace agrees very well with the experiment, a typical performance of this code.

Each numerical experiment is considered satisfactory when the computed current trace matches the experiment in current rise profile and peak current, in time position of the current dip, in slope, and absolute value of the dip (see Fig. 1). The results were obtained for the PF400, the UNU/ICTP PFF, the NX2, and PF1000 at 35 kV; for which current traces and neutron yields are available. We thus established these reliable points for our computed Y_n data. To make the results less sketchy, additional points were obtained for the PF1000 from 13.5 to 40 kV though these additional points are not supported by published results. More work will need to be done. However, even with the results obtained, it is clear that the model code is producing a scaling of $Y_n \sim I_{\text{pinch}}{}^{4.7}$; and $Y_n \sim I_{\text{peak}}{}^{3.9}$. These computed scaling laws are in reasonable agreement with those put up from time to time by experimental compilations,[20,21] considering that in the experimental results, I_{pinch} is seldom properly measured, in many cases, only estimated from I_{peak}. Such estimates are dicey since the relationship between the peak total current I_{peak} (measured in the external circuit) and the pinch current I_{pinch} flowing in the tube is variable. Our code is consistent in that I_{pinch} is rigorously computed by fitting the total current trace. This gives confidence in the scaling ability of the code for Y_n as well.

An important question is how to improve the neutron yields of experiments. One obvious strategy is to increase I_{pinch} by reducing L_o. For example, the 30 μF, 110 nH UNU/ICTPPFF (Refs. 2, 4, 12, and 19) had its L_o reduced to 20 nH evolving, as it were, into the NX2.[7,16,22] I_{peak} more than doubled. More importantly, though less than doubled, I_{pinch} increased from 120 to 220 kA. Neutron yields increased three to five times, as did S*X*R yields.

What about a bank such as the PF1000? With C_o at 1332 μF, its L_o of 30 nH (fitted by the code) is already low relative to its huge C_o. We have run the code using the machine and model parameters determined from Fig. 1, modified by information about values of I_{peak} at 35 kV. Operating the PF1000 at 35 kV and 3.5 torr, we varied the anode radius a (with corresponding adjustment to b to maintain a constant $c=b/a$) to keep the peak axial speed at 10 cm/μs. The anode length z_o was also adjusted to maximize I_{pinch}.

L_o was decreased from 100 nH progressively to 5 nH. As expected, I_{peak} increased from 1.66 to 4.4 MA. As L_o was reduced from 100 to 35 nH, I_{pinch} also increased, from 0.96 to 1.05 MA. However, then unexpectedly on further reduction from 35 to 5 nH, I_{pinch} stopped increasing, instead decreasing slightly to 1.03 MA at 20 nH, to 1.0 MA at 10 nH, and to 0.97 MA at 5 nH. Y_n also had a maximum value of 3.2×10^{11} at 35 nH.

To explain this unexpected result, we examine the energy distribution in the system at the end of the axial phase (see Fig. 1) just before the current drops from peak value I_{peak} and then again near the bottom of the almost linear drop to I_{pinch}. The energy equation describing this current drop is written as follows:

$$0.5I_{\text{peak}}{}^2(L_o + L_a f_c{}^2) = 0.5I_{\text{pinch}}{}^2(L_o/f_c{}^2 + L_a + L_p) + \delta_{\text{cap}} + \delta_{\text{plasma}}, \quad (2)$$

where L_a is the inductance of the tube at full axial length z_o. δ_{plasma} is the energy imparted to the plasma as the current sheet moves to the pinch position and is the integral of $0.5(dL/dt)I^2$. We approximate this as $0.5L_pI_{\text{pinch}}{}^2$ (which is an underestimate) for this case. δ_{cap} is the energy flow into or out of the capacitor during this period of current drop. If the duration of the radial phase is short compared to the capacitor time constant, the capacitor is effectively decoupled and δ_{cap} may be put as zero. From this consideration we obtain

$$I_{\text{pinch}}{}^2 = I_{\text{peak}}{}^2(L_o + 0.5L_a)/(2L_o + L_a + 2L_p), \quad (3)$$

where we have taken $f_c=0.7$ and approximated $f_c{}^2$ as 0.5.

Taking the example of PF1000 at 35 kV we obtain for each L_o the corresponding L_a ($\sim$0.65 nH/cm of z_o) and L_p [$\sim$3.8 nH/cm of (Ref. 4) $z_p \sim a$]. For example, at $L_o=100$ nH, $L_a=52$ nH, and $L_p=29$ nH giving $I_{\text{pinch}}/I_{\text{peak}}$ as 0.63. This ratio drops progressively as L_o decreases. For $L_o=5$ nH, $L_a=13$ nH, and $L_p=77$ nH giving the ratio as 0.25. The results show that as L_o is reduced from 100 nH, at first, the increase in I_{peak} more than compensates for the drop in $I_{\text{pinch}}/I_{\text{peak}}$ and I_{pinch} increases from $L_o=100$ nH to $L_o=40$ nH. Below $L_o=40$ nH, the drop in $I_{\text{pinch}}/I_{\text{peak}}$ catches up with the increase in I_{peak} leading to the numerically observed flat maximum of I_{pinch}. Y_n also has a flat maximum of 3.2×10^{11} at $L_o=40-30$ nH.

The current limitation can now be seen as firstly a consequence of Eq. (3). Generally, as L_o is reduced, I_{peak} increases; a is necessarily increased leading (Ref. 4) to a longer pinch length z_p, hence a bigger L_p. Lowering L_o also results in a shorter rise time, hence a necessary decrease in z_o, reducing L_a. Thus, from Eq. (3), lowering L_o decreases the fraction $I_{\text{pinch}}/I_{\text{peak}}$. Secondly, this situation is compounded by another mechanism. As L_o is reduced, the *L*-*C* interaction time of the capacitor bank reduces while the duration of the current drop increases due to an increasing a. This means that as L_o is reduced, the capacitor bank is more and more coupled to the inductive energy transfer processes with the accompanying induced large voltages that arise from the radial compression. Looking again at the derivation of Eq. (3) from Eq. (2) a nonzero δ_{cap}, in this case, of positive value, will act to decrease I_{pinch} further. The lower L_o the more pronounced is this effect.

Summarizing this discussion, the pinch current limitation is not a simple effect, but is a combination of the two complex effects described above, namely, the interplay of the various inductances involved in the plasma focus processes abetted by the increasing coupling of C_o to the inductive energetic processes, as L_o is reduced.

We carried out several sets of experiments on the PF1000, each set with a different damping factor. In every case, an optimum inductance was found around 30–60 nH with I_{pinch} decreasing as L_o was reduced below the optimum value. We also carried out another set of experiments with a planned focus with C_o of 300 μF. For that device, optimum L_o was found to be 20 nH. More sets of experiments need to be run to gain further experience and insight to understand better the complex interactions of the several parameters that conspire to determine the optimum L_o. The results of these ongoing studies will be published in more detail in due course.

In the meantime, enough information has been obtained from the numerical experiments to enable a statement that for PF1000, reducing L_o from its present 20–30 nH will increase neither the observed I_{pinch}, nor the neutron yield.

The prevailing thinking seems to be that the lower L_o is made, the higher performance a plasma focus would have in terms of driving current and Y_n. This paper shows that, on the contrary, given a fixed C_o powering a plasma focus, there exists an optimum L_o for maximum I_{pinch}. Reducing L_o further will increase neither I_{pinch} nor Y_n. Plasma focus research now has to meet the challenges posed by this "pinch current limitation" effect.

[1]S. Lee in *Laser and Plasma Technology*, edited by S. Lee, B. C. Tan, C. S. Wong, and A. C. Chew (World Scientific, Singapore, 1985), pp. 387–420.
[2]S. Lee, T. Y. Tou, S. P. Moo, M. A. Elissa, A. V. Gholap, K. H. Kwek, S. Mulyodrono, A. J. Smith, Suryadi, W. Usala, and M. Zakaullah, Am. J. Phys. **56**, 62 (1988).
[3]T. Y. Tou, S. Lee, and K. H. Kwek, IEEE Trans. Plasma Sci. **17**, 311 (1989).
[4]S. Lee and A. Serban, IEEE Trans. Plasma Sci. **24**, 1101 (1996).
[5]D. E. Potter, Phys. Fluids **14**, 1911 (1971).
[6]M. H. Liu, X. P. Feng, S. V. Springham, and S. Lee, IEEE Trans. Plasma Sci. **26**, 135 (1998).
[7]S. Lee, P. Lee, G. Zhang, X. Feng, V. A. Gribkov, M. Liu, A. Serban, and T. Wong, IEEE Trans. Plasma Sci. **26**, 1119 (1998).
[8]S. Bing, "Plasma dynamics and x-ray emission of the plasma focus," Ph.D. thesis, NIE, 2000 (in ICTP Open Access Archive: http://eprints.ictp.it/99/)
[9]S. Lee, in http://ckplee.myplace.nie.edu.sg/plasmaphysics/ (2000 and 2007).
[10]S. Lee in ICTP Open Access Archive: http://eprints.ictp.it/85/ (2005).
[11]V. Siahpoush, M. A. Tafreshi, S. Sobhanian, and S. Khorram, Plasma Phys. Controlled Fusion **47**, 1065 (2005).
[12]S. Lee, Twelve Years of UNU/ICTP PFF-A Review (1998) IC, 98 (231); A. Salam ICTP, Miramare, Trieste (in ICTP OAA: http://eprints.ictp.it/31/).
[13]L. Soto, P. Silva, J. Moreno, G. Silvester, M. Zambra, C. Pavez, L. Altamirano, H. Bruzzone, M. Barbaglia, Y. Sidelnikov, and W. Kies, Braz. J. Phys. **34**, 1814 (2004).
[14]H. Acuna, F. Castillo, J. Herrera, and A. Postal, International Conference on Plasma Sci, 3–5 June 1996 (unpublished), p. 127.
[15]C. Moreno, V. Raspa, L. Sigaut, and R. Vieytes, Appl. Phys. Lett. **89**, 15 (2006).
[16]D. Wong, P. Lee, T. Zhang, A. Patran, T. L. Tan, R. S. Rawat, and S. Lee, Plasma Sources Sci. Technol. **16**, 116 (2007).
[17]V. A. Gribkov, A. Banaszak, B. Bienkowska, A. V. Dubrovsky, I. Ivanova-Stanik, L. Jakubowski, L. Karpinski, R. A. Miklaszewski, M. Paduch, M. J. Sadowski, M. Scholz, A. Szydlowski, and K. Tomaszewski, J. Phys. D **40**, 3592 (2007).
[18]J. D. Huba, 2006 Plasma Formulary, p. 44. http://wwwppd.nrl.navy.mil/nrlformulary/NRL_FORMULARY_07.pdf
[19]S. V. Springham, S. Lee, and M. S. Rafique, Plasma Phys. Controlled Fusion **42**, 1023 (2000).
[20]W. Kies, in *Laser and Plasma Technology*, Proceedings of Second Tropical College, edited by S. Lee, B. C. Tan, C. S. Wong, A. C. Chew, K. S. Low, H. Ahmad, and Y. H. Chen (World Scientific, Singapore, 1988), pp. 86–137.
[21]H. Herold, in *Laser and Plasma Technology*, Proceedings of Third Tropical College, edited by C. S. Wong, S. Lee, B. C. Tan, A. C. Chew, K. S. Low, and S. P. Moo (World Scientific, Singapore, 1990), pp. 21–45.
[22]A. Patran, R. S. Rawat, J. M. Koh, S. V. Springham, T. L. Tan, P. Lee, and S. Lee, 31st EPS Conference on Plasma Physics London, 2004 (unpublished), Vol. 286, p. 4.213.
[23]http://www.intimal.edu.my/school/fas/UFLF/

Erratum

The published paper contains 2 errors on page 1 which are corrected by this note. The relevant paragraph is reproduced here in parenthesis with the corrections highlighted in bold red:

"Total beam energy is estimated[17] as proportional to $L_p I_{pinch}^2$, a measure of the pinch inductance energy, L_p being the focus pinch inductance. Thus the number of beam ions is $N_b \sim L_p I_{pinch}^2 / v_b^2$ and n_b is **N_b** divided by the focus pinch volume. Note that $L_p \sim \ln(b/r_p) z_p$, that[4] $\tau \sim r_p \sim z_p$, and that $v_b \sim U^{1/2}$ where U is the disruption-caused diode voltage[17]. Here 'b' is the cathode radius. We also assume reasonably that U is proportional to V_{max}, the maximum voltage induced by the current sheet collapsing radially towards the axis.

Hence we derive: $Y_{b\text{-}t} = C_n$ **n_i** $I_{pinch}^2 z_p^2 ((\ln b/r_p)) \sigma / V_{max}^{1/2}$
(1)

where I_{pinch} is the current flowing through the pinch at start of the slow compression phase; r_p and z_p are the pinch dimensions at end of that phase. Here C_n is a constant which in practice we will calibrate with an experimental point."

There is another error on page 2, Fig 1. The vertical axis should be labeled 'Total Current in MA'.

Journal of Fusion Energy first online 20 February 2008 DOI : 10.1007/s10894-008-9132-7

Neutron Scaling Laws from Numerical Experiments

S Lee[1,2] & S H Saw[1]

[1]INTI International University College, 71800 Nilai, Malaysia
[2]Nanyang Technological University, National Institute of Education, Singapore 637616

leesing@optusnet.com.au

Abstract

Experimental data of neutron yield Y_n against pinch current I_{pinch} is assembled to produce a more global scaling law than available. From the data a mid-range point is obtained to calibrate the neutron production mechanism of the Lee Model code. This code is then used for numerical experiments on a range of focus devices to derive neutron scaling laws. The results are the following: $Y_n=2x10^{11}I_{pinch}^{4.7}$ and $Y_n=9x10^{9}I_{peak}^{3.9}$. It is felt that the scaling law with respect to I_{pinch} is rigorously obtained by these numerical experiments when compared with that obtained from measured data, which suffers from inadequacies in the measurements of I_{pinch}.

Keywords: Plasma Focus Neutron Scaling Pinch Current Focus modelling Lee Model

Introduction

A major feature of the plasma focus is its fusion neutron yield. Even a simple trolley mounted 3kJ device such as the UNU/ICTP PFF routinely produces[1] a yield of $Y_n=10^8$ neutrons, operating in deuterium. A big machine such as the PF1000 typically produces 10^{11} neutrons per shot[2]. Moreover since the neutrons are produced in a short pulse of the order of 10ns, the rate of neutron production is 10^{16} neutrons/s even for a small machine and can go up to 10^{20} for a large machine.

From a compilation of experimental data over a wide range of energies a scaling law of $Y_n \sim I_{pinch}^{3.3}$ was presented by Bernard[3], where I_{pinch} is the current flowing through the dense pinch in the focused plasma. Kies[4] presented another compilation showing $Y_n \sim I_{pinch}^{4}$ whilst Herold[5] had results showing $Y_n \sim I_{pinch}^{3.2}$. Gribkov has recently[2] suggested that the experimental data can be interpreted with the power law as high as 5 in particular when dealing with the same device.

One significant uncertainly in compiling such a scaling law is the interpretation of I_{pinch}. The current most conveniently measured in most experiments is the total current flowing into the tube (usually measured with a Rogowski coil placed at the collector plate

just outside the tube). This total current has a maximum value I_{peak}. If one estimates I_{pinch} from the total current measurement there are two difficulties: 1. it is difficult to determine the point on the current waveform where the plasma has gone into the pinch phase, and 2. even after estimating this point, it still remains to estimate the fraction of total current that in fact flows into the pinch. One way is to use small magnetic coils to probe the pinch region. For small machines this method is not suitable because of the amount of space available and the small size of the pinch so that the probes inevitably interfere with the pinching current sheet. For large machines, results have been obtained[5] but with large errors quoted as 20%. Moreover the shot-to-shot variability of focus performance means that the final presentation of results relies greatly on how the particular research group chooses to present the results. For example the yield may be presented as a range, with some shots considered not representative discarded, and perhaps the biggest values of observed yield also presented. It is quite remarkable that despite all these difficulties there is a consensus of opinion that the index in this power scaling law has the value in the range of 3 to 5.

Compilation of experimental results

In this paper we have combined the laboratory data that we have[1-7], which includes recent results from some smaller machines e.g. Soto's[6] PF400 and the large[2] PF1000 as well as a high performance repetitive device[7], the NX2. This gives a good fit of $Y_n=9x10^{10}I_{pinch}^{3.8}$. The main reason for this compilation of experimental results is to provide a calibration point for setting the neutron yield mechanism of the Lee Model code, described below. A calibration point is chosen at around the middle of the current range at $I_{pinch}=0.5MA$, $Y_n=6x10^9$ neutrons. This point is close to the PF1000's machine parameters with properly adjusted dimensions if it could be fired at 13.5kV.

The results of the compilation are shown in Fig 1.

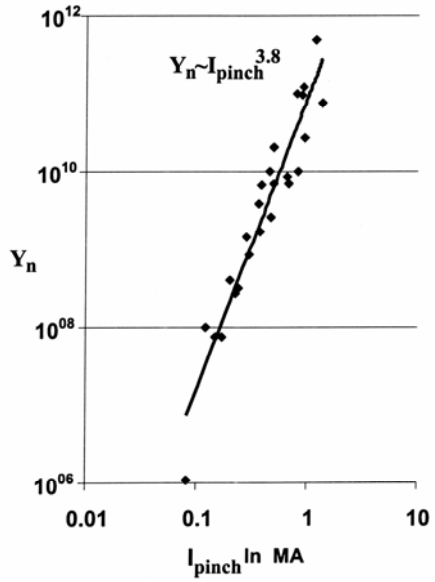

Fig 1. Y_n scaling with I_{pinch} from laboratory data

The Model used for the numerical experiments

The Lee Model has been widely used to simulate axial and radial phase dynamics, temperatures and thermodynamic properties and radiation yields. To realistically simulate any plasma focus all that is needed is a measured current trace of that plasma focus. Recently the model code[8] has been extended to include a phenomenological beam-target mechanism based partially on that proposed by Gribkov[2].
The main mechanism producing the neutrons is a beam of fast deuteron ions interacting with the hot dense plasma of the focus pinch column. The fast ion beam is produced by diode action in a thin layer close to the anode with plasma disruptions generating the necessary high voltages. This mechanism, described in some details in a recent paper[9], results in the following expression used for the model code:

$$Y_{b\text{-}t} = \text{calibration constant} \times \mathbf{n_i}\, I_{pinch}^{2}\, z_p^{2} (\ln(b/r_p))\sigma / V_{max}^{0.5}$$

where I_{pinch} is the current at the start of the slow compression phase, r_p and z_p are the pinch radius and pinch length at the end of the slow compression phase, V_{max} is the maximum value attained by the inductively induced voltage, σ is the D-D fusion cross section (n branch)[10] corresponding to the beam ion energy **and n_i is the pinch ion density**. The D-D cross section σ is obtained by using beam energy equal to 3 times V_{max}, to conform to experimental observations.

Scaling Laws derived from the numerical experiments

This paper applies the code to several machines including the PF400, UNU/ICTP PFF, the NX2 and Poseidon. The PF1000 which has a current curve published at 27kV and Y_n published at 35kV provided an important point. Moreover using parameters for the PF1000 established at 27 kV and 35 kV, additional points were taken at different voltages ranging from 13.5kV upwards to 40kV.

These machines were chosen because each has a published current trace and hence the current curve computed by the model code could be fitted to the measured current trace. Once this fitting is done our experience is that the other computed properties including dynamics, energy distributions and radiation are all realistic. This gives confidence that the computed Y_n for each case is also realistic. Moreover since each chosen machine also has measured Y_n corresponding to the current trace, the computed Y_n could also be compared with the measured to ensure that the computed results are not incompatible with the measured values.

The results are shown in Table 1 and Fig 2.

In Table 1, corresponding to each laboratory device, the operating voltage V_o and pressure P_o are typical of the device, as is the capacitance C_o. It was found that the static inductance L_o usually needed to be adjusted from the value provided by the laboratory. This is because the value provided could be for short circuit conditions, or an estimate including the input flanges and hence that value may not be sufficiently close to L_o. The

dimensions b (outer radius), a (anode radius) and z_o (anode length) are also the typical dimensions for the specific device. The speed factor[11] S is also included. All devices except Poseidon have typical S values. Poseidon is the exceptional high speed device in this respect. The minimum pinch radius is also tabulated as $k_{min}=r_p/a$. It is noted that this parameter increases from 0.14 for the smaller machines towards 0.2 for the biggest machines. The ratio I_{pinch}/I_{peak} is also tabulated showing a trend of decreasing from 0.65 for small machines to 0.4 for the biggest machines.

Table 1. Computed values of I_{peak}, I_{pinch} and Y_n for a range of Plasma Focus Machines

Machine	V_o (kV)	P_o (torr)	L_o (nH)	C_o (μF)	b (cm)	a (cm)	Z_o (cm)	I_{peak} (MA)	I_{pinch} (MA)	S	Y_n	k_{min}	I_{pinch}/I_{peak}
PF400	28	6.6	40	0.95	1.55	0.60	1.7	0.126	0.082	82	1.1×10^{06}	0.14	0.65
UNU	15	4	110	30	3.2	0.95	16	0.182	0.123	96	1.2×10^{07}	0.14	0.68
NX2 T	15	5	20	28	5	2	7	0.386	0.225	86	2.5×10^{08}	0.16	0.58
Calibration	16	5	24	308	7	4	30	0.889	0.496	99	5.6×10^{09}	0.17	0.56
NX2 T-2	12.5	10.6	19	28	3.8	1.55	4	0.357	0.211	71	2.4×10^{08}	0.16	0.59
PF1000	13.5	3.5	33	1332	8.00	5.78	60	0.924	0.507	89	9.6×10^{09}	0.17	0.55
	18	3.5	33	1332	10.67	7.70	60	1.231	0.636	89	2.9×10^{10}	0.18	0.52
	23	3.5	33	1332	13.63	9.84	60	1.574	0.766	89	6.8×10^{10}	0.19	0.49
	27	3.5	33	1332	16	11.60	60	1.847	0.862	89	1.2×10^{11}	0.19	0.47
	30	3.5	33	1332	17.77	12.80	60	2.049	0.929	89	1.6×10^{11}	0.20	0.45
	35	3.5	33	1332	20.74	15.00	60	2.399	1.037	89	2.7×10^{11}	0.20	0.43
	40	3.5	33	1332	23.70	17.10	60	2.736	1.137	89	4.1×10^{11}	0.21	0.42
Poseidon	60	3.8	18	156	9.50	6.55	30	3.200	1.260	251	3.3×10^{11}	0.20	0.39

Fig 2. Y_n scaling with I_{pinch} and I_{peak} from numerical experiments

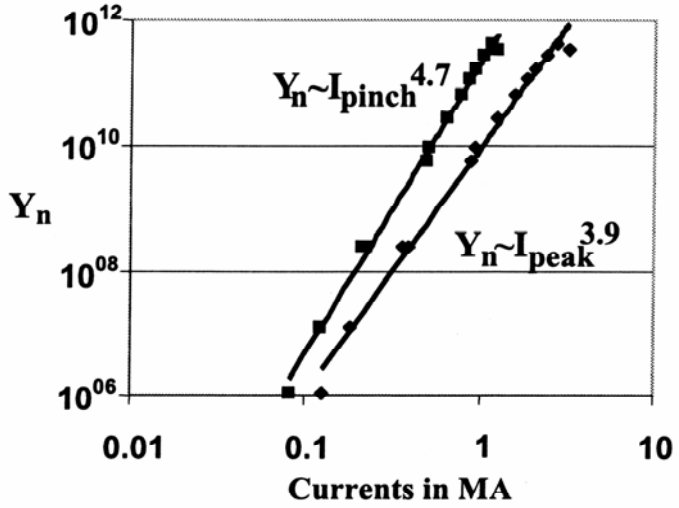

The resultant data with improved optimization yield more up to date scaling laws: $Y_n \sim I_{pinch}^{4.7}$ and $Y_n \sim I_{peak}^{3.9}$. It is necessary to emphasize again that the I_{pinch} may be considered to be computed rigorously especially for those cases where an experimental current curve is available. Once the computed current curve is fitted accurately to the experimental current curve, the resultant pinch position is pinpointed as well as the fraction of current going into the pinch.

This is in contrast to the laboratory data where I_{pinch} is usually only estimated and if measured is subject to large errors. A study of the data suggests that in most cases I_{pinch} is overestimated by experimentalists. With all these considerations it would appear that the scaling laws arising from the code are not inconsistent with experimental observations and may complement the more conventionally compiled scaling laws to provide comprehensive database for experiments.

Conclusion

Neutron scaling laws have been derived from computation using the Lee Model code. These are: $Y_n \sim I_{pinch}^{4.7}$ and $Y_n \sim I_{peak}^{3.9}$. In these numerical experiments I_{pinch} is rigorously computed whereas in compilation of laboratory results I_{pinch} is usually just guessed at or at best estimated. These numerically derived scaling laws are not inconsistent with compilation from laboratory experiments. The numerically derived scaling law against I_{pinch} has an index of 4.7 which is higher than the usually accepted scaling law with index of 3.2 to 4. The indications are that the numerically derived scaling laws being more rigorous and consistent in derivation may actually be more realistic and more reliable for use in interpreting, designing or planning experiments.

References

[1]S Lee, T.Y. Tou, S.P. Moo, M.A. Elissa, A.V. Gholap, K.H. Kwek, S. Mulyodrono, A.J. Smith, Suryadi, W.Usala & M. Zakaullah. Amer J Phys **56**, 62 (1988)

[2]V.A.Gribkov, A. Banaszak, B. Bienkowska, A.V. Dubrovsky, I. Ivanova-Stanik, L. Jakubowski, L. Karpinski, R.A.Miklaszewski, M. Paduch, M.J. Sadowski, M. Scholz, A. Szydlowski & K. Tomaszewski. J Phys D: Appl.Phys.40,3592 (2007)

[3]A Bernard, A Coudeville, J P Garconnet, A Jolas, J de Mascureau & C Nazet, Journal de Physique Colloque C1, supplement no 5, **39**, C1 (1978)

[4]W Kies in *Laser and Plasma Technology*, Procs of Second Tropical College Ed by S Lee et al, World Scientific, Singapore ISBN 9971-50-767-6 (1988) p86-137

[5] H Herold in *Laser and Plasma Technology*, Procs of Third Tropical College Ed by C S Wong et al, World Scientific, Singapore ISBN 981-02-0168-0 (1990) p21-45

[6] L. Soto, P. Silva, J. Moreno, G. Silvester, M. Zambra, C. Pavez, L. Altamirano, H. Bruzzone, M. Barbaglia, Y. Sidelnikov & W. Kies. Brazilian J Phys 34, 1814 (2004)

[7] A. Patran, R. S. Rawat, J. M. Koh, S. V. Springham, T. L. Tan, P. Lee & S. Lee. *31st EPS Conference on Plasma Phys. London, 2004 ECA Vol.**28G**, P-4.213 (2004)*

[8]S Lee, Radiative Dense Plasma Focus Computation Package: RADPF, in http://www.intimal.edu.my/school/fas/UFLF
[9]S Lee & S H Saw *Pinch Current Limitation Effect in Plasma Focus*, Applied Phys Lett. **92**, 021503 (2008)
[10]J.D.Huba. 2006 Plasma Formulary pg44
http://wwwppd.nrl.navy.mil/nrlformulary/NRL_FORMULARY_07.pdf
[11]S Lee & A Serban, IEEE Trans Plasma Sci **24**, 1101-1105 (1996)

Erratum

This version of the paper contains two additions to the published paper on pg 3.
The paragraph containing the additions is reproduced here in parenthesis, with the additions highlighted in bold red:

$$"Y_{b\text{-}t} = \text{calibration constant} \times \mathbf{n_i}\, I_{pinch}^{2}\, z_p^{2} (\ln(b/r_p))\sigma / V_{max}^{0.5}$$

where I_{pinch} is the current at the start of the slow compression phase, r_p and z_p are the pinch radius and pinch length at the end of the slow compression phase, V_{max} is the maximum value attained by the inductively induced voltage and σ is the D-D fusion cross section (n branch)[10] corresponding to the beam ion energy **and n_i is the pinch ion density**. The D-D cross section σ is obtained by using beam energy equal to 3 times V_{max}, to conform to experimental observations."

Plasma Phys. Control. Fusion **50** (2008) 065012 (8pp) doi:10.1088/0741-3335/50/6/065012

Numerical experiments on plasma focus pinch current limitation

S Lee[1,2,3], P Lee[2], S H Saw[3] and R S Rawat[2]

[1] Institute for Plasma Focus Studies, 32 Oakpark Drive, Chadstone, VIC 3148, Australia
[2] Nanyang Technology University, National Institute of Education, Singapore 637616, Singapore
[3] INTI International University College, 71800 Nilai, Malaysia

E-mail: leesing@optusnet.com.au

Received 18 February 2008
Published 11 April 2008
Online at stacks.iop.org/PPCF/50/065012

Abstract

Contrary to the general expectation that performance of a plasma focus would progressively improve with progressive reduction of its static inductance L_o, a recent paper suggests that there is in fact an optimum L_o below which although the peak total current increases progressively the pinch current and consequently the neutron yield of that plasma focus would not increase, but instead decreases. This paper describes the numerical experiments and results that led to this conclusion.

1. Introduction

A recent paper [1] suggests that for any plasma focus with a fixed capacitance C_o, there is an optimum static inductance L_o, below which the focus pinch current I_{pinch} no longer increases. This paper describes the numerical experiments and results leading to this conclusion of a plasma focus pinch current limitation effect.

We need to say right at the beginning that this I_{pinch} limitation effect is not the same[4] as the I_{max}-related mechanism proposed by Nukulin and Polukhin [2] to explain an observed neutron saturation effect. In [2] it is postulated that in large plasma focus devices the peak total discharge current I_{peak} (which they denote as I_{max}) hardly increases with increase in storage energy through increase in bank capacitance C_o. This 'tardiness' of I_{peak} leads to an equation which in the limit of large storage energies E tends towards a constant neutron yield Y_n. We state here that [2] deals with a special, though important, class of plasma focus discharge conditions where an increase in C_o needs a corresponding increase in anode length z_o. This in turn leads to a situation where the effective discharge impedance, which determines I_{peak} for any given operating voltage V_o, seems to tend towards a constant value as E increases with C_o, thus limiting I_{peak}. This work delves deeper into the problem. We show that in another

[4] The authors thank a reviewer for stressing that this comparison of our work with that of [2] should be made.

class of plasma focus discharges, as static inductance L_o is progressively reduced to lower and lower values it is I_{pinch} (as distinct from and not representative of I_{peak}) which becomes limited whilst I_{peak} continues to increase progressively with no sign at all of reaching a constant value. This remarkable divergence of the values of I_{pinch} from I_{peak} indicates then that generally for all classes of plasma focus there is a need to distinguish between the total discharge current I_{total}, which has a peak value I_{peak}, and the actual current driving the plasma dynamics which we call the plasma sheath current I_p, denoting its value at the start of the focus pinch phase as I_{pinch}.

2. Distinguishing the I_{total} waveform from the I_p waveform

A measured trace of I_{total} is commonly obtained with a Rogowski coil wrapped around the plasma focus flange through which is fed I_{total} discharged from the capacitor bank between the coaxial electrodes across the back wall. A part of I_{total}, being the plasma sheath current I_p, lifts off the back-wall insulator and drives a shock wave axially down the coaxial space. We denote f_c as the current fraction I_p/I_{total} for the axial phase and f_{cr} for the radial phases. In modeling it is found that a reasonable value for initial trial for f_c is 0.7 with a similar first trial value for f_{cr}. However in a DPF78 experiment [3,4] f_c was found to vary from 0 at the start of the axial phase rising rapidly above 0.6 for the rest of the axial phase. In the radial phase f_{cr} was found to stay above 0.6 before dropping to 0.48 at the start of the pinch and then towards 0.4 as the pinch phase progressed. These Stuttgart results confirm a complex relationship between the waveforms of I_{total} and I_p.

The performance of a plasma focus is closely linked to the current I_{pinch} actually participating in the focus pinch phase rather than the total current flowing in the circuit. It is a common practice to take I_{peak} or some representative fraction of it as I_{pinch}. Another practice is to take the value of I_{total} at the time of the pinch as I_{pinch} [2,5]. Whilst in their special cases this practice could be justifiable, the distinction of I_p from I_{total} should generally be clearly made. We emphasize that it should be the value of I_p at the time of pinch which is the relevant value for the purpose of yield scaling. The practice of associating yield scaling with the total current waveform (i.e. taking I_{peak} or I_{total} at estimated pinch time) would be justifiable if there were a linear relationship between the waveforms of I_{total} and I_p. However as shown by the Stuttgart experiments [3, 4] the actual relationship is a very complex one which we may ascribe to the interplay of the various electro-dynamical processes including the relative values of static inductance L_o, tube inductance and the dynamic resistances which depend on the tube geometry and plasma sheath speeds. This relationship may change from one machine to the next. Whilst these electro-dynamical processes and other relevant ones such as radiation are amenable to modeling there are other machine effects such as back wall restriking (for example due to high induced voltages during the pinch phase) which can almost unpredictably affect the relationship between I_{total} and I_p during the crucial radial phases. Hence it is not only simplistic to discuss scaling in terms of the I_{total} waveform (i.e. taking I_{peak} or the value of I_{total} at the estimated time of pinch) but also inconsistent.

One of the most important features of a plasma focus is its neutron production recently reviewed by Vikhrev and Korolev [6]. The well-known neutron yield scaling, with respect to current, based on various compilations of experimental data, is $Y_n \sim I_{pinch}^x$ where x is varied [5, 7–9] in the range 3–5. In a recent paper [10], numerical experiments using a code was used to derive a scaling with $x = 4.7$. Difficulties in the interpretation of experimental data ranging across big and small plasma focus devices include the assignment of the representative neutron yield Y_n for any specific machine and the assignment of the value of I_{pinch}. In a few larger machines attempts were made to measure I_{pinch} using magnetic probes placed

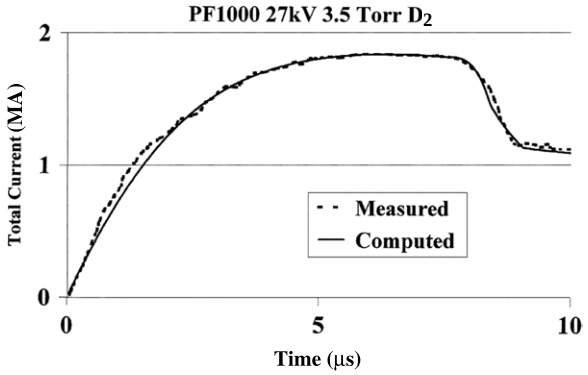

Figure 1. Computed (solid line) versus measured (dotted line) current traces for PF1000 at 27 kV, 3.5 Torr D_2.

near the pinch region [3, 4, 9], with uncertainties of 20%. Moreover the probes would have affected the pinching processes. In most other cases related to yield scaling data compilation or interpretation I_{pinch} is simply assigned a value based on the measurement of peak total current I_{peak} or the value of total current at the observed current dip.

The difficulties in distinguishing I_{pinch} from I_{total} are obviated in numerical experiments using the Lee Model [11–15]. In a typical simulation, the I_{total} trace is computed and fitted to a measured I_{total} trace from the particular focus. Three model parameters for fitting are used: axial mass swept-up factor f_{m}, current factor f_{c} and radial mass factor f_{mr}. A fourth model parameter, radial current factor, f_{cr} may also be used. When correctly fitted the computed I_{total} trace agrees with the measured I_{total} trace in peak amplitude, rising slope profile and topping profile (see figure 1) which characterize the axial phase electro-dynamics. The radial phase characteristics are reflected in the roll-over of the current trace from the flattened top region, and the subsequent current drop or dip. Any machine effects, such as restrikes, current sheath leakage and consequential incomplete mass swept up, not included in the simulation physics is taken care of by the final choice of the model parameters, which are fine-tuned in the feature-by-feature comparison of the computed I_{total} trace with the measured I_{total} trace. Then there is confidence that the computed gross dynamics, temperature, density, radiation, plasma sheath currents, pinch current and neutron yield may also be realistically compared with experimental values.

One simplifying feature of the method is that the ratio $I_{\text{p}}/I_{\text{total}}$ is fitted as an average value f_{c} over the axial phase and separately as another average value f_{cr} over the radial phase. Whilst an improvement would be to fit some time function of f_{c} and f_{cr}, our experience is that the present method is adequate to give good agreement for the axial and radial phases up to the end of the plasma focus pinch phase. This ability to fit well has been demonstrated for all classes of machines from the sub-kJ PF400 to high repetition kJ plasma focus NX2 to the medium energy DPF78 all the way through Poseidon and up to the MJ PF1000. The excellent agreement between computed and measured current waveforms for all these machines are available for download from [15].

In a recent paper [5] there was expectation that the large MJ plasma focus PF1000 in Warsaw could increase its discharge current, and its pinch current, and consequently neutron yield by a reduction of its external inductance L_{o}. To investigate this point experiments were carried out using the Lee Model [15]. Unexpectedly, the results indicated that whilst I_{peak} indeed progressively increased with reduction in L_{o}, no improvement may be achieved due

to a pinch current limitation effect [1]. This paper reports on the detailed results of these numerical experiments.

3. The model code used for the experiments

The Lee Model couples the electrical circuit with plasma focus dynamics, thermodynamics and radiation enabling realistic simulation of all gross focus properties.

The basic model, described in 1984 [11], was successfully used to assist several experiments [16–18]. An improved 5-phase model and code incorporating small disturbance speed [19], and radiation coupling with dynamics assisted other research projects [20–22], and was web-published in 2000 [13] and 2005 [14]. Plasma self-absorption was included in 2007 [13]. It has been used extensively in several machines including UNU/ICTP PFF [16–18, 20, 23], NX2 [21, 22], NX1 [21], and adapted for the Filippov-type plasma focus DENA [24]. A recent development is the inclusion of neutron yield, Y_n, using a beam–target mechanism [5], incorporated in the present version [15] of the code RADPFV5.13, resulting in realistic Y_n scaling with I_{pinch} [10]. The description, theory, code and a broad range of results of this 'Universal Plasma Focus Laboratory Facility' is available for download from [15].

4. The numerical experiments and discussions

A measured current trace of the PF1000 with $C_o = 1332\,\mu$F, operated at 27 kV, 3.5 Torr deuterium, has been published [5], with cathode/anode radii $b = 16$ cm, $a = 11.55$ cm and anode length $z_o = 60$ cm. In the numerical experiments we fitted external (or static) inductance $L_o = 33$ nH and stray resistance $r_o = 6.3\,\text{m}\Omega$ with model parameters: $f_m = 0.14$, $f_c = 0.7 = f_{cr}$ and $f_{mr} = 0.35$. The computed current trace (see figure 1 solid line) agrees very well with the measured trace (figure 1 dotted line) through all the phases, axial and radial, right down to the bottom of the current dip indicating the end of the pinch phase. This agreement confirms the model parameters for the PF1000.

Once the model parameters have been fitted to a machine for a given gas, these model parameters may be used with some degree of confidence when operating parameters such as the voltage are varied. We kept these model parameters constant and ran numerical experiments for PF1000 with $C_o = 1332\,\mu$F, operating at 35 kV and 3.5 Torr deuterium. We varied L_o, from 100 nH in steps of 5 nH.

At each L_o, 'a' was adjusted, whilst keeping $c = b/a = 1.385$, so that the peak axial speed is fixed at 10.2 cm μs^{-1} to conform with optimal focus operation in terms of speed factor [18] $S = (I_{peak}/a)/p^{0.5}$, where p is the operating pressure. Decreasing L_o changes the current rise time as well as effective drive time as shown in figure 2, which shows three current waveforms corresponding to $L_o = 100$ nH (current peaking at 1.66 MA), $L_o = 30$ nH (current peaking at 2.6 MA) and $L_o = 5$ nH (current peaking at $I_{peak} = 4.4$ MA). The experiment for $L_o = 5$ nH was optimized with $z_o = 20$ cm and corresponds to the current trace with current drop starting at around 3 μs. A fourth trace (for $L_o = 5$ nH but non-optimal $z_o = 40$ cm) is shown with rise time and peak current almost exactly coincidental with the optimal $L_o = 5$ nH trace but with a longer drooping top and with current drop starting just after 5 μs.

As L_o was reduced, I_{peak} increased; and hence 'a' needed to be increased to maintain optimum S. At the same time because of the reducing current drive time, z_o needed to be reduced. The geometry inevitably moved from a long thin Mather-type to a shorter fatter geometry (see table 1). Thus whilst L_o and axial section inductance L_a reduced, the pinch inductance L_p increased due to increased pinch length [1, 18].

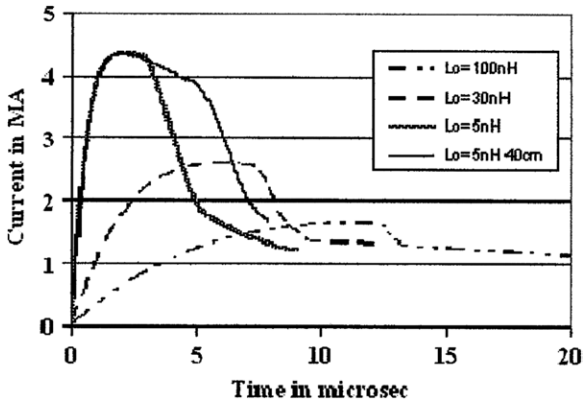

Figure 2. PF1000 current waveforms (computed) at 35 kV, 3.5 Torr D_2 for a range of L_o.

Table 1. Effect on currents and ratio of currents I_{pinch}/I_{peak} (computed) as L_o is reduced-PF1000 at 35 kV, 3.5 Torr D_2.

L_o (nH)	b (cm)	a (cm)	z_o (cm)	I_{peak} (MA)	I_{pinch} (MA)	Y_n 10^{11}	I_{pinch}/I_{peak}
100	15.0	10.8	80	1.66	0.96	2.44	0.58
80	16.0	11.6	80	1.81	1.00	2.71	0.55
60	18.0	13.0	70	2.02	1.03	3.01	0.51
40	21.5	15.5	55	2.36	1.05	3.20	0.44
35	22.5	16.3	53	2.47	1.05	3.20	0.43
30	23.8	17.2	50	2.61	1.05	3.10	0.40
20	28.0	21.1	32	3.13	1.03	3.00	0.33
10	33.0	23.8	28	3.65	1.00	2.45	0.27
5	40.0	28.8	20	4.37	0.97	2.00	0.22

With large $L_o = 100$ nH it is seen (figure 2) that the rising current profile is flattened from what its waveform would be if unloaded; and peaks at around 12 μs (before its unloaded rise time, not shown, of 18 μs) as the current sheet goes into the radial phase. The current drop, less than 25% of peak value, is sharp compared with the current rise profile. At $L_o = 30$ nH the rising current profile is less flattened, reaching a flat top at around 5 μs, staying practically flat for some 2 μs before the radial phase current drop to 50% of its peak value in a time which is still short compared with the rise time. With L_o of 5 nH, the rise time is now very short, there is hardly any flat top; as soon as the peak is reached, the current waveform droops significantly. There is a small kink on the current waveform of both the $L_o = 5$ nH, $z_o = 20$ cm and the $L_o = 5$ nH, $z_o = 40$ cm. This kink corresponds to the start of the radial phase which, because of the large anode radius, starts with a relatively low radial speed, causing a momentary reduction in dynamic loading.

Looking at the three types of traces it is seen that for $L_o = 100$ nH to 30 nH, there is a wide range of z_o that may be chosen so that the radial phase may start at peak or near peak current, although the longer values of z_o tend to give better energy transfers into the radial phase. Incidentally, this type of trace is the special class considered by Nukulin and Polukhin [2]. For this type of discharge there is sufficient L_o to limit the value of the discharge current until the inductance of the tube, around 1.1 nH cm^{-1}, gets to sufficient value, to in combination with L_o and the dynamic resistance (about 0.6 Ohm per cm/μs), determine the value of I_{peak}. In such

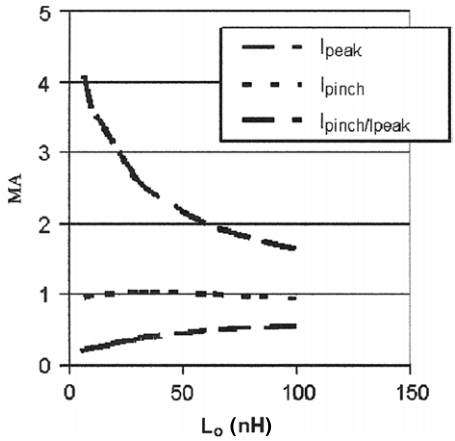

Figure 3. Effect on currents and current ratio (computed) as L_o is reduced-PF1000, 35 kV, 3.5 Torr D_2.

a case it may be justified in a very rough approximation, by ignoring L_o, to say that I_{peak} is controlled by the full tube inductance, which approximation then results in their conclusion [2] of I_{peak} (their I_{max}) tending towards a constant value with capacitance increase.

At $L_o = 5$ nH, another class of discharge, the situation is quite different. I_{peak} is much bigger than that calculated using the full tube inductance. This is because with such a small L_o, there is a short rise time, 'over-shooting' as it were to a value of current beyond that eventually set when the full tube inductance comes into play (see figure 2). There is hardly any flat top, the current drooping almost immediately from its peak value as the tube inductance increases progressively. For this type of trace, clearly one would not increase length z_o proportionately to increase in C_o; since the radial phase should not be delayed too long after early occurrence of I_{peak}. Length matching becomes more critical, although because of the small rate of drop, in terms of optimizing energy transfer to the pinch, a balance has to be sought between increasing storage volume as the axial current sheath advances and the falling current. The computation shows that for $L_o = 5$ nH, $z_o = 20$ cm is optimum, and that $z_o = 40$ cm is already significantly off optimum because of the current droop.

At each L_o, after 'a' was adjusted for optimum S, the computed shape of the current waveform was used as a guide to fine-tune z_o for optimum performance, which was finally indicated by the largest I_{pinch} which corresponds closely to the largest Y_n.

The optimized situation for each value of L_o is shown in table 1. The table shows that as L_o is reduced, I_{peak} rises with each reduction in L_o with no sign of any limitation. However, I_{pinch} reaches a broad maximum of 1.05 MA around 40–30 nH. Neutron yield Y_n also shows a similar broad maximum peaking at 3.2×10^{11} neutrons. Figure 3 shows a graphical representation of this I_{pinch} limitation effect. The curve going up to 4 MA at low L_o is the I_{peak} curve. Although we have numerical data down to $L_o = 1$ nH, in table 1 we only present data from $L_o = 5$–100 nH. At $L_o = 1$ nH, I_{peak} reached beyond 6 MA whilst I_{pinch} dropped further to around 0.95 MA.

Thus I_{peak} shows no sign of limitation as L_o is progressively reduced. However I_{pinch} reaches a broad maximum. From figure 3 there is a stark and important message. One must distinguish clearly between I_{pinch} and I_{peak}. In general one cannot take I_{peak} to be representative of I_{pinch}.

One may also wish to reflect briefly about the effect on the distribution of energies in the inductances as L_o is lowered. As L_o is lowered from 100 to 1 nH, the optimum L_a also

decreases from around 90 nH to around 6 nH. Thus the percentage of energy stored in L_a compared with the total stored inductive energy just before the radial phase has increased from some 47% to some 86%. It is unfortunate that this increase in available energy is prevented by the interplay of all the physical processes from acting to increase the pinch current. We note that the current fitting process gives us confidence that the computed pinch current is as reliable as if we had measured it; the reliability being the same degree as the reliability of the measurement of the total discharge current, which we used for the current fitting during the computation process. A recent comparison of a numerical experiment with laboratory measurements confirms the reliability of this numerical technique [25].

The above numerical experiments were conducted using a factor RESF = stray resistance/surge impedance of 1.16, fitted for the PF1000. This is a high resistive damping factor for a capacitor bank. We repeated the experiments for PF1000 at 40 kV keeping everything the same except changing RESF to a lower 0.21. Again I_{pinch} limitation is clearly seen; at $L_o = 60$ nH with I_{pinch} of 1.59 MA and a corresponding Y_n maximum of 8.2×10^{11} neutrons.

We carried out several more sets of experiments of which one was with a smaller $C_o = 300\ \mu$F, operated at 15 kV, 6 Torr D2, with $c = 2$ and RESF = 0.1. We used $f_m = 0.08$, $f_c = 0.7$, $f_{mr} = 0.16$ which are the parameters typically fitted for smaller plasma focus such as the NX2 [21, 22]. The peak axial speed was kept at $10.3\,\text{cm}\,\mu\text{s}^{-1}$ for optimal S. L_o was reduced from 40 to 1 nH. Again a broad maximum was found for I_{pinch} at 0.455 MA in the range 25–15 nH, with a broad maximum for Y_n of 4.4×10^9 neutrons around $L_o = 25$ nH.

Comparing the energy distribution in the circuit elements at the start of the radial phase at the time of I_{peak} to that near the bottom of the almost linear drop to the time of pinch (see figure 1) the ratio I_{pinch}/I_{peak} was derived as a function of L_o, L_a and L_p [1]. This equation and the increasing coupling of the remnant capacitor energy to the pinch were shown to be the physical mechanisms responsible for the decrease in the fraction I_{pinch}/I_{peak} and for the pinch current limitation as L_o is progressively reduced, despite the progressive increase in I_{peak}. That theoretical consideration and the results of these numerical experiments together clearly show the importance of distinguishing clearly I_{pinch} from I_{peak}; and to use I_{pinch} rather than I_{peak} as a more consistent quantity for scaling focus yields.

It is also clear that design of new experiments should consider the optimum value of L_o, rather than the more wasteful practice, technologically speaking, of designing for as low a value of L_o as possible. Moreover, this limitation may now require consideration of new technology to overcome the limitation of I_{pinch}, for example by some form of current stepping [26, 27].

5. Conclusions

The results of these sets of numerical experiments indicate that generally corresponding to each plasma focus capacitance of C_o, there is an optimum value for L_o below which performance in terms of I_{pinch} and Y_n does not improve. These experiments confirm the pinch current limitation effect in a plasma focus.

References

[1] Lee S and Saw S H 2008 *Appl. Phys. Lett.* **92** 021503
[2] Nukulin V Ya and Polukhin S N 2007 *Plasma Phys. Rep.* **33** 271–7
[3] Oppenländer T 1981 *PhD Dissertation* University of Stuttgart, Germany
[4] Decker G, Flemming L, Kaeppeler H J, Oppenlander T, Pross G, Schilling P, Schmidt H, Shakhatre M and Trunk M 1980 *Plasma Phys.* **22** 245–60

[5] Gribkov V A *et al* 2007 *J. Phys. D: Appl. Phys.* **40** 3592
[6] Vikhrev V V and Korolev V D 2007 *Plasma Phys. Rep.* **33** 356–80
[7] Bernard A, Coudeville A, Garconnet J P, Jolas A, Mascureau J de and Nazet C 1978 *J. Physique Colloque* C1 (suppl 5) **39** C1
[8] Kies W 1988 *Laser and Plasma Technology, Proc. 2nd Tropical College* (Kuala Lumpur, Malaysia) ed S Lee *et al* (Singapore: World Scientific) pp 86–137
[9] Herold H 1990 *Laser and Plasma Technology, Proc. 3rd Tropical College* (Kuala Lumpur, Malaysia) ed C S Wong *et al* (Singapore: World Scientific) pp 21–45
[10] Lee S and Saw S H Neutron scaling laws from numerical experiments *J. Fusion Energy* at press
[11] Lee S 1984 *Radiations in Plasmas* ed B McNamara (Singapore: World Scientific) pp 978–87
[12] Lee S 1991 *IEEE Trans. Plasma Sci.* **19** 912
[13] Lee S 2000/2007 http://ckplee.myplace.nie.edu.sg/plasmaphysics/
[14] Lee S 2005 ICTP Open Access Archive: http://eprints.ictp.it/85/
[15] Lee S Radiative Dense Plasma Focus Computation Package: RADPF http://www.intimal.edu.my/school/fas/UFLF/
[16] Lee S *et al* 1988 *Am. J. Phys.* **56** 62
[17] Tou T Y, Lee S and Kwek K H 1989 *IEEE Trans. Plasma Sci.* **17** 311
[18] Lee S and Serban A 1996 *IEEE Trans. Plasma Sci.* **24** 1101–5
[19] Potter D E 1971 *Phys. Fluids* **14** 1911
[20] Liu M H, Feng X P, Springham S V and Lee S 1998 *IEEE Trans. Plasma Sci.* **26** 135–40
[21] Lee S, Lee P, Zhang G, Feng X, Gribkov V A, Liu M, Serban A and Wong T 1998 *IEEE Trans. Plasma Sci.* **26** 1119
[22] Bing S 2000 Plasma dynamics and x-ray emission of the plasma focus *PhD Thesis* NIE ICTP Open Access Archive: http://eprints.ictp.it/99/
[23] Lee S 1998 Twelve Years of UNU/ICTP PFF—A Review IC, 98 (231) Abdus Salam ICTP, Miramare, Trieste; *ICTP OAA*: http://eprints.ictp.it/31/
[24] Siahpoush V, Tafreshi M A, Sobhanian S and Khorram S 2005 *Plasma Phys. Control. Fusion* **47** 1065
[25] Lee S, Saw S H, Lee P C K, Rawat R S and Schmidt H 2008 *Appl. Phys. Lett.* **92** 111501
[26] Lee S 1984 *J. Phys. D: Appl. Phys.* **17** 733
[27] Saw S H 1991 Experimental studies of a current-stepped pinch *PhD Thesis* Universiti Malaya

Computing plasma focus pinch current from total current measurement

S. Lee,[1,2,3,a] S. H. Saw,[2] P. C. K. Lee,[3] R. S. Rawat,[3] and H. Schmidt[4]
[1]*Institute for Plasma Focus Studies, 32 Oakpark Dr, Chadstone, Victoria 3148, Australia*
[2]*INTI International University College, 71800 Nilai, Malaysia*
[3]*Nanyang Technological University, National Institute of Education, Singapore 637616, Singapore*
[4]*International Centre for Dense Magnetized Plasmas, 00-908 Warsaw, Poland*

(Received 12 February 2008; accepted 25 February 2008; published online 18 March 2008)

The total current I_{total} waveform in a plasma focus discharge is the most commonly measured quantity, contrasting with the difficult measurement of I_{pinch}. However, yield laws should be scaled to focus pinch current I_{pinch} rather than the peak I_{total}. This paper describes how I_{pinch} may be computed from the I_{total} trace by fitting a computed current trace to the measured current trace using the Lee model. The method is applied to an experiment in which both the I_{total} trace and the plasma sheath current trace were measured. The result shows good agreement between the values of computed and measured I_{pinch}. © *2008 American Institute of Physics*. [DOI: 10.1063/1.2899632]

The total current I_{total} waveform in a plasma focus discharge is easily measured using a Rogowski coil. The peak value I_{peak} of this trace is commonly taken as a measure of the drive efficacy and is often used to scale the yield performance of the plasma focus.[1,2] This is despite the fact that yields[3–5] should more consistently be scaled to focus pinch current I_{pinch}, since it is I_{pinch} which directly powers the emission processes. The reason many researchers use I_{peak} instead of I_{pinch} for scaling is simply that while I_{peak} is easily measured, I_{pinch}, which is the value of the plasma sheath current I_p at time of pinch, is very difficult to measure even in large devices where it is possible to place magnetic probes near the pinch.[3–5] This measurement is also inaccurate and perturbs the pinch. In a small device, there is no space for such a measurement. A simpler method was tried to compute the I_p waveform using measured waveforms of I_{total} and tube voltage.[6,7] This was achieved only up to the start of the radial phase thereby missing the crucial I_{pinch}. To date, I_{pinch} is still one of the least measured and often misunderstood quantities. In this connection, an attempt was made[8] to compute the time of pinch. However, in that work, I_{pinch} was assumed to be I_{total} at pinch time.

The relationship between I_{pinch} and I_{peak} is not simple and has only been recently elaborated.[9] It primarily depends on the value of the static inductance L_0 compared to the dynamic inductances of the plasma focus. As L_0 is reduced, the ratio $I_{\text{pinch}}/I_{\text{peak}}$ drops. Thus, yield laws scaled to I_{peak} will not consistently apply when comparing two devices with all parameters equal but differing significantly in L_0. Better consistency is achieved when yield laws are scaled to I_{pinch}.

In this paper, we propose a numerical method to consistently deduce I_{pinch} from any measured trace of I_{total}. This method will improve the formulation and interpretation of focus scaling laws. Specifically, we define I_{pinch} as the value of I_p at the start of the quiescent (or pinch) phase of the plasma focus radial dynamics. We now discuss the distinction between I_{total} and the plasma sheath current I_p.

A measured trace of I_{total} is commonly obtained with a Rogowski coil wrapped around the plasma focus flange[10] through which is fed I_{total} discharged from the capacitor bank between the coaxial electrodes across the back wall. A part of I_{total}, being the plasma sheath current I_p, lifts off the back-wall insulator and drives a shock wave axially down the coaxial space. At the end of the anode, the plasma sheath turns from axial into radial motion. The previously axially moving I_p becomes a radial inward moving cylindrical sheath, driving a radially collapsing cylindrical shock front. When this shock front arrives on axis, because the plasma is collisional, a reflected shock (RS) moves radially outwards[11] until it meets the incoming driving current sheath. The increased pressure of the RS region then rapidly slows down the sheath. This is the start of the pinch phase. All the dynamics dominating the axial and radial phases is determined by I_p. A proportion of the current, the difference between I_{total} and I_p, does not take part in the dynamics. This leakage current stays at the back wall,[4–7,12] but parts of it may be diffusely distributed.

We define for the axial phase f_c as I_p/I_{total} and distinguish it from f_{cr} for the radial phase. Likewise, it had been shown that only a fraction of the mass[6,12] encountered by the axial sheath is swept up. This fraction we call f_m, distinguishing the radial phase fraction as f_{mr}. The rest of the mass either leaks through the sheath or is swept outwards due to the canting of the sheath.

The exact time profile of the I_{total} trace is governed by the bank, tube, the operational parameters, and by the mass and current fractions and variation of these fractions through the axial and radial phases. Although we may expect these fractions to vary, for simplicity, we average these model parameters as f_m, f_c and f_{mr} and f_{cr}.

The Lee model couples the electrical circuit with plasma focus dynamics, thermodynamics, and radiations enabling realistic simulation of all gross focus properties. The basic model was described in 1984 (Ref. 13) and used to assist projects.[6,7,10,11,14–16] An improved five-phase code crucially incorporating small disturbance speed,[17] and radiation coupling with dynamics, assisted further projects,[8,18–23] and was published in the internet in 2000 (Ref. 24) and 2005.[25] Plasma self-absorption was included[24] in 2007. It has been used in machines including UNU/ICTP PFF,[10,11,15,16,21] NX2,[18–20] and NX1,[18] and has been adapted to the Filippov-type DENA.[8,22,23] Neutron yield Y_n using a beam-target mechanism,[1] is included in the present version RADPFV5.13, (Ref. 26) resulting in realistic Y_n scaling[27] with I_{pinch}. Since

[a]Electronic mail: leesing@optusnet.com.au.

the detailed theory of the model and the code are given in the websites,[24–26] we proceed to the proposed method to compute I_{pinch}.

The method requires a measured I_{total} waveform from a discharge in which the bank parameters, the tube geometry, and operating parameters are known. The Lee model code[26] is used to simulate this discharge using the model parameters for fitting. The model parameters are varied until the simulated I_{total} trace agrees with the measured I_{total} trace. The start of the quiescent or pinch phase is pinpointed from the computation and the computed value of I_p at this time is obtained as I_{pinch}.

For the actual fitting process, the bank parameters L_0, C_0 (capacitance), and r_0 (resistance) are put into the active sheet of the EXCEL code. If r_0 is not available, a trial value of $0.1(L_0/C_0)^{1/2}$ is used. Next, the tube parameters b (cathode radius), a (anode radius), and z_0 (anode length) and the operational parameters V_0 (voltage) and P_0 (pressure) are entered. The fill gas is indicated by its atomic weight and number in the cells provided. Trials values of f_m, f_c, f_{mr}, and f_{cr} are then entered, e.g., 0.08, 0.7, 0.1, and 0.7, respectively The code is then run. The computed I_{total} trace which is one of the graphical outputs is transferred onto a comparison active sheet and plotted onto a graph together with the preloaded measured I_{total} trace. Detailed comparison, feature by feature, of the traces is made.

The first step is fitting the axial phase. This involves variation of f_m and f_c while observing the changes that appear on the resulting computed I_{total} trace in respect to the rise time, rising shape, and I_{peak} and how these features compare with the corresponding features of the measured I_{total} trace. During this fitting an increase in f_c increases axial speed which increases dynamic resistance, thus, lowering current magnitude on the rising slope. The greater rate of increase of tube inductance flattens out the rising slope. A decrease in f_m has almost the same effect. However, a change in f_c has an additional subtle effect of changing the relative effect of the tube inductance. This means that increasing the speed by a certain amount by increasing f_c, then reducing it by exactly the same amount by a corresponding increase in f_m will not bring the I_{total} shape and magnitude back to the shape and value before either change is made. Thus, one has to get each of f_m and f_c separately correct to get both the current shape and magnitude correct in the rising current profile.

The value of r_0 may need to be adjusted. An increase of r_0 lowers the current trace at all points proportionately. Adjustment to nominally given values of L_0, sometimes even C_0, may need to be made before a good fit is achieved. When all values are properly adjusted and when f_m and f_c are correctly fitted, the measured rising profile of the computed I_{total}, usually up to the peak value I_{peak}, is found to fit the measured rising profile well in both shape and magnitude.

Two other points need to be noted.[6,7] The measured I_{total} profile usually has a starting portion which seems to rise more slowly than the computed trace. This is due to the switching process during which, until fully switched, the spark gap presents additional resistance. It could also be compounded by the lift-off delay.[21] Practically, this effect is compensated by shifting the whole computed trace forward in time, usually by a small amount around 50 ns. A related note is that z_0 may need to be reduced to account for the shape of the back-wall insulator.

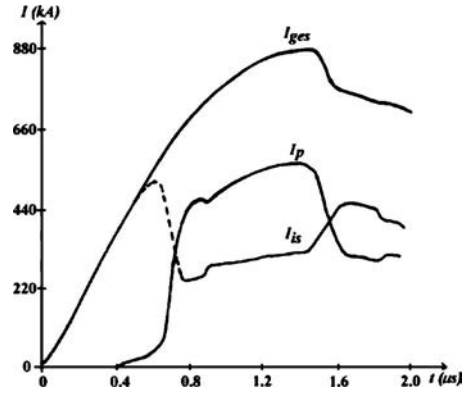

FIG. 1. DPF78 measured I_{total} (labeled as I_{ges}) and measured I_p waveforms. The third trace I_{is} is the difference of I_{total} and I_p.

The next step is fitting the radial phases. We need to understand the transition from the axial to the radial phase. For a plasma focus to work well, it is usually operated with a speed such that its axial run-down time is about equal to the rise time of the circuit with the device short circuited across its back wall. With the focus tube connected, the current rise time will be larger. At the same time, the current trace is flattened out. In most cases this increased rise time will be cut short by the start of the radial phase. As this phase starts, the current trace starts to roll over, at first imperceptibly, then clearly dipping and then sharply dips as the focus dynamics enters the severe pinch phase which absorbs a significant portion of the energy from the driving magnetic field. Thus, the second step in the fitting consists of adjusting f_{mr} and f_{cr} so that the computed current roll over and the dip agree in shape, slope, and extent of dip with the measured waveform.

We now describe how we tested the validity of this method. In an experiment in Stuttgart using the DPF78,[4,5] a Rogowski coil measured the I_{total} trace, and magnetic probes measured the I_p waveform. The bank parameters were $C_0 = 15.6\ \mu$F (nominal) and $L_0 = 45$ nH (nominal), tube parameters were $b = 50$ mm, $a = 25$ mm, and $z_0 = 150$ mm, and operating parameters were $V_0 = 60$ kV, and $P_0 = 7.6$ Torr deuterium. Figure 1 shows these measured I_{total} (labeled as I_{ges} in Fig. 1) and I_p waveforms. The third trace is the difference of I_{total} and I_p.

These parameters were put into the code. The best fit for the computed I_{total} with the measured I_{total} waveform was obtained with the following: bank parameters were $C_0 = 17.2\ \mu$F, $L_0 = 55$ nH, and $r_0 = 3.5\ \text{m}\Omega$; tube parameters were $b = 50$ mm, $a = 25$ mm, and $z_0 = 137$ mm; and operating parameters were $V_0 = 60$ kV and $P_0 = 7.6$ Torr deuterium. Model parameters of $f_m = 0.06$, $f_c = 0.57$, $f_{mr} = 0.08$, and $f_{cr} = 0.51$ were fitted.

With these parameters, the computed I_{total} trace compared well with the measured I_{total} trace, as shown in Fig. 2. The computed dynamics, currents, and other properties of this plasma focus discharge were deemed to be correctly simulated.

From the computation results the start of the pinch phase was obtained as 1.551 μs. At this time I_{pinch} was computed as $0.51 \times 778 = 396.8$ kA. The value of I_{pinch} from the measured I_p trace was not immediately obvious since there was no striking feature that marked this moment on the measured I_p trace. We used the following procedure to obtain it, at the

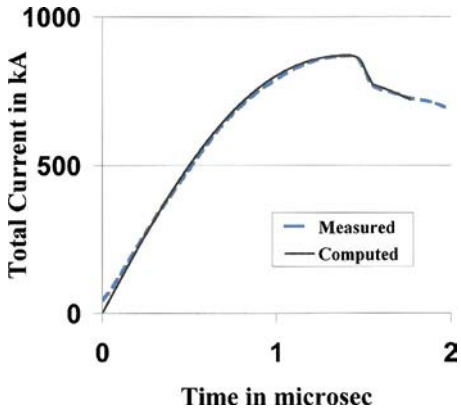

FIG. 2. (Color online) Comparison of computed (solid line) and measured (dashed line) I_{total} waveforms.

same time to get further insight into f_c and f_{cr}.

The ratio I_p/I_{total} (digitized from Fig. 1) was plotted as a function of time and shown in Fig. 3. At time=1.551 μs, the ratio was found to be 0.49, and I_{total} was measured to be 778 kA. Hence, I_{pinch}=381.2 kA was measured in the Stuttgart DPF78 experiment. The computed I_{pinch} was 4% larger than the measured I_{pinch}. This difference was to be expected considering that the modeled f_{cr} was an average value of 0.51; while the laboratory measurement showed (Fig. 3) that in the radial phase I_p/I_{total} varied from 0.63 to 0.4, and at the start of the pinch phase this ratio was 0.49 and rapidly dropping. Thus, one would expect the computed value of I_{pinch} to be somewhat higher than the measured, which turned out to be the case. Nevertheless, the difference of 4% is better than the typical error of 20% estimated for I_{pinch} measurements using magnetic probes.[3]

The conclusion is that the numerical method is a good alternative, being more accurate and convenient and only needing a commonly measured I_{total} waveform.

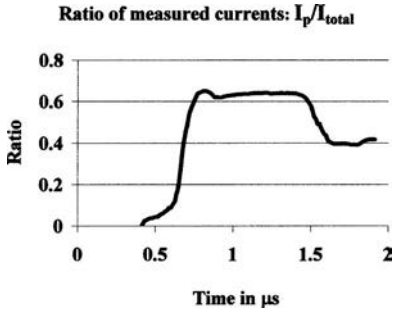

FIG. 3. Ratio of measured I_p to I_{total} as a function of time.

[1]V. A. Gribkov, A. Banaszak, B. Bienkowska, A. V. Dubrovsky, I. Ivanova-Stanik, L. Jakubowski, L. Karpinski, R. A. Miklaszewski, M. Paduch, M. J. Sadowski, M. Scholz, A. Szydlowski, and K. Tomaszewski, J. Phys. D **40**, 3592 (2007).
[2]L. Soto, P. Silva, J. Moreno, G. Silvester, M. Zambra, C. Pavez, L. Altamirano, H. Bruzzone, M. Barbaglia, Y. Sidelnikov, and W. Kies, Braz. J. Phys. **34**, 1814 (2004).
[3]H. Herold, in *Laser and Plasma Technology*, Proceedings of Third Tropical College, edited by C. S. Wong, S. Lee, B. C. Tan, A. C. Chew, K. S. Low, and S. P. Moo (World Scientific, Singapore, 1990), pp. 21–45.
[4]T. Oppenländer, Ph.D. thesis, University of Stuttgart, Germany, 1981.
[5]G. Decker, L. Flemming, H. J. Kaeppeler, T. Oppenlander, G. Pross, P. Schilling, H. Schmidt, M. Shakhatre, and M. Trunk, Plasma Phys. **22**, 245 (1980).
[6]T. Y. Tou, "Pinch radius ratio of the plasma focus," Ph.D. Thesis, University of Malaya, 1986.
[7]T. Y. Tou, S. Lee, and K. H. Kwek, IEEE Trans. Plasma Sci. **17**, 311 (1989).
[8]V. Siahpoush, S. Sobhanian, S. Khorram, and M. A. Tafreshi, ICOPS 2003, IEEE Conference Record, 2003 (unpublished), 444.
[9]S. Lee and S. H. Saw, Appl. Phys. Lett. **92**, 021503 (2008).
[10]S. Lee, T. Y. Tou, S. P. Moo, M. A. Elissa, A. V. Gholap, K. H. Kwek, S. Mulyodrono, A. J. Smith, S. Suryadi, W. Usala, and M. Zakaullah, Am. J. Phys. **56**, 62 (1988).
[11]S. Lee and A. Serban, IEEE Trans. Plasma Sci. **24**, 1101 (1996).
[12]S. P. Chow, S. Lee, and B. C. Tan, J. Plasma Phys. **8**, 21 (1972).
[13]S. Lee, in *Radiations in Plasmas*, edited by B. McNamara (World Scientific, Singapore, 1984), pp. 978–987.
[14]S. Lee, IEEE Trans. Plasma Sci. **19**, 912 (1991).
[15]M. H. Liu, X. P. Feng, S. V. Springham, and S. Lee, IEEE Trans. Plasma Sci. **26**, 135 (1998).
[16]S. Lee, "Twelve years of UNU/ICTP PFF—A review," ICTP OAA report, 1998 (unpublished).
[17]D. E. Potter, Phys. Fluids **14**, 1911 (1971).
[18]S. Lee, P. Lee, G. Zhang, X. Feng, V. A. Gribkov, M. Liu, A. Serban, and T. Wong, IEEE Trans. Plasma Sci. **26**, 1119 (1998).
[19]S. Bing, "Plasma dynamics and x-ray emission of the plasma focus," Ph.D. thesis, Nanyang Technological University, Singapore, 2000.
[20]D. Wong, P. Lee, T. Zhang, A. Patran, T. L. Tan, R. S. Rawat, and S. Lee, Plasma Sources Sci. Technol. **16**, 116 (2007).
[21]T. Zhang, X. Lin, K. A. Chandra, T. L. Tan, S. V. Springham, A. Patran, P. Lee, S. Lee, and R. S. Rawat, Plasma Sources Sci. Technol. **14**, 368 (2005).
[22]V. Siahpoush, M. A. Tafreshi, S. Sobhanian, and S. Khorram, Comments Plasma Phys. Controlled Fusion **47**, 1065 (2005).
[23]S. Goudarzi, R. Amrollahi, and R. Saberi Moghaddam, J. Fusion Energy (to be published).
[24]S. Lee, Radiative Dense Plasma Focus Computation Package RADPF, (http://ckplee.myplace.nie.edu.sg/plasmaphysics/).
[25]S. Lee, in ICTP Open Access Archive, 2005 (http://eprints.ictp.it/85/).
[26]S. Lee, Radiative Dense Plasma Focus Computation Package RADPF, (http://www.intimal.edu.my/school/fas/UFLF).
[27]S. Lee and S. H. Saw, J. Fusion Energy (to be published).

Plasma Phys. Control. Fusion **50** (2008) 105005 (14pp) doi:10.1088/0741-3335/50/10/105005

Current and neutron scaling for megajoule plasma focus machines

S Lee

Institute for Plasma Focus Studies, 32 Oakpark Drive, Chadstone, VIC 3148, Australia
and
Nanyang Technological University, National Institute of Education, Singapore 637616, Singapore
and
INTI International University College, 71800 Nilai, Malaysia

E-mail: leesing@optusnet.com.au

Received 20 June 2008, in final form 22 July 2008
Published 21 August 2008
Online at stacks.iop.org/PPCF/50/105005

Abstract

In a 2007 paper Nukulin and Polukhin surmised from electrodynamical considerations that, for megajoule dense plasma focus devices, focus currents and neutron yield Y_n saturate as the capacitor energy E_0 is increased by increasing the capacitance C_0. In contrast, our numerical experiments show no saturation; both pinch currents and Y_n continue to rise with C_0 although at a slower rate than at lower energies. The difference in results is explained. The Nukulin and Polukhin assumption that the tube inductance and length are proportional to C_0 is contrary to laboratory as well as numerical experiments. Conditions to achieve Y_n of 10^{13} in a deuterium plasma focus are found from our numerical experiments, at a storage energy of 3 MJ with a circuit peak current of 7.6 MA and focus pinch current of 2.5 MA.

1. Introduction

In a 2007 paper Nukulin and Polukhin [1] surmised that the peak discharge current I_{peak} in a plasma focus reaches a limiting value when the storage energy of its capacitor bank is increased to the megajoule level by increasing the bank capacitance C_0 at a fixed charging voltage V_0. The crux of their argument is that for such large banks, increasing C_0 increases the discharge current risetime which then requires an increase in the length of the focus tube in order for the axial transit time to match the current risetime. According to their reasoning the axial tube inductance $L_a = 2 \times 10^{-7} \ln(b/a) z_0$ (their equation (5)) where b and a are the outer and inner radii, respectively, and the length of the coaxial section is $z_0 = (\pi/2)(L_a C_0)^{0.5} v_a$ (their equation (4)). We rewrite their equations in SI units throughout except where stated otherwise. Here v_a is the average axial speed in the rundown stage which in experimental situations is known to be best kept at a value around 10^5 (or 10 cm μs^{-1}). This argument leads

to $L_a = (10^{-7}\pi v_a \ln(b/a))^2 C_0$. That is, L_a is proportional to C_0, resulting in, for fixed V_0, a saturated $I_{peak} = V_0/(L_a/C_0)^{0.5}$ for megajoule banks, where L_a is so large as to make the static bank inductance insignificant. We shall refer to this chain of argument as the Nukulin and Polukhin (N&P) scenario. Saturation of Y_n then follows in that scenario.

A careful consideration of the above argument reveals two factors that need to be re-examined. Firstly, matching the transit time to the 'rise time' of $(L_a C_0)^{0.5}$ (as required by their equation (4)) is a hypothetical situation assuming the circuit inductance has the value of L_a from the beginning of the discharge. In actual fact the circuit starts with a much smaller value of L_0 and only attains the value of L_a towards the end of the axial transit. Secondly, the dynamic resistance loading the circuit due to current sheet motion at instantaneous speed v_z is $(1/2)(dL/dt) = 10^{-7}\ln(b/a)v_z$ and has the same value, 3.3 mΩ, for $v_z = 10^5$ and $b/a = 1.39$, independent of the value of C_0. This dynamic resistance becomes increasingly dominant and controlling in the early stage of the discharge for larger and larger C_0, since at the early stage of the discharge the tube inductance has not grown to large values yet.

Because of these two factors, for large devices with large C_0, we will show that the current peaks early in the discharge and then exhibits a slight drooping, nearly flat-top behavior as seen in the published discharge current waveform of the PF1000 [2, 3]. This early peaking changes the situation from the N&P scenario, resulting in much smaller optimized L_a with correspondingly shorter z_0. This invalidates their equation (4). Laboratory and also numerical experiments are not carried out with the values of L_a and z_0 envisaged by the N&P scenario, simply because these N&P values are far too large for optimum conditions. Using optimized values of L_a and z_0, in contrast to the saturation envisaged by the N&P scenario, the optimized I_{pinch} and Y_n continue to rise with E_0, as C_0 is increased, although the rates of increase indeed slow down. In the case of Y_n the scaling is $Y_n \sim E_0^2$ at small E_0 and becomes $Y_n \sim E_0$ in the higher energy ranges.

We would like to state here that we are not disputing the experimental observations [1,4,5] that have led to the idea of a neutron saturation effect in plasma focus operation. What we dispute in this paper is the N&P scenario, which is erroneous in its conclusion that the cause of neutron saturation is electrodynamical (electrotechnical in their words) in nature. Our numerical experiments show that from electrodynamical considerations, the currents I_{peak} and I_{pinch} do not saturate, nor does the neutron yield. The cause of saturation needs to be looked for elsewhere, beyond electrodynamical considerations, which is outside the scope of this paper. This paper continues to present our numerical experiments.

Although the analytic and intuitive approach is useful in attempts to understand this electrodynamic problem it could also lead to oversimplified, indeed erroneous, conclusions. The underlying physics is simple, requiring only the charge and energy conservation conditions imposed into the time-varying circuit equations, for example, in the form often expressed by Kirchhoff's current and voltage rules, and an equation of motion for the axial phase. These equations are coupled to reflect the physics that the plasma current I_p drives the motion, and the resistive and inductive loading of the motion in turn affect the magnitude and temporal behavior of the total discharge current, I_{total}. The solution of such a coupled set of equations will take into account all of the subtle interplay of current drive and motional impedances and the temporal relationships among early and late discharge characteristics imposed by a large capacitance C_0, coupled to a static inductance L_0 and a growing tube inductance L_z. This electrodynamic situation is very well handled by the Lee model code [6] which after the axial phase goes on to compute the radial, including the pinch phase. This paper describes numerical experiments carried out with the code to uncover the scaling of I_{pinch} and Y_n up to tens of megajoules.

2. The Lee model code

The Lee model couples the electrical circuit with plasma focus dynamics, thermodynamics and radiation, enabling realistic simulation of all gross focus properties.

The basic model, described in 1984 [7], was successfully used to assist several projects [8–11]. An improved 5-phase model and code incorporating a small disturbance speed [12] and radiation coupling with dynamics assisted other research projects [13–15] and was web-published in 2000 [16] and 2005 [17]. Plasma self-absorption was included in 2007 [16] improving soft x-ray yield simulation. The code has been used extensively in several machines including UNU/ICTP PFF [8, 11, 13, 14, 18], NX2 [14, 15], NX1 [14] and adapted for the Filippov-type plasma focus DENA [19]. A recent development is the inclusion of the neutron yield, Y_n, using a beam–target mechanism [3, 20, 22], incorporated in the present version [6] of the code RADPFV5.13, resulting in realistic Y_n scaling with I_{pinch} [20]. The versatility and utility of the model is demonstrated in its clear distinction of I_{pinch} from I_{peak} [21] and the recent uncovering of a plasma focus pinch current limitation effect [3, 22]. The description, theory, code and a broad range of results of this 'Universal Plasma Focus Laboratory Facility' is available for download from [6].

The last sections of this paper discuss the scaling of the neutron yield with increasing voltage. In that discussion it is found that there is little advantage for D–D beam–target fusion, and indeed a disadvantage for D–T beam–target fusion, to exceed 90 kV charging voltage. To understand that situation it is necessary to revisit the neutron production mechanism used in the model. The neutron yield is computed using a phenomenological beam–target neutron generating mechanism [2]. A beam of fast deuteron ions is produced by diode action in a thin layer close to the anode, with plasma disruptions generating the necessary high voltages. The beam interacts with the hot dense plasma of the focus pinch column to produce the fusion neutrons. The beam–target yield is derived [3] as

$$Y_{b\text{-}t} = C_n n_i I_{pinch}^2 z_p^2 (\ln b/r_p)\sigma / V_{max}^{0.5},$$

where n_i is the ion density, r_p is the radius of the plasma pinch with length z_p, σ the cross-section of the D–D fusion reaction, n-branch and V_{max} the maximum voltage induced by the current sheet collapsing radially towards the axis. C_n is treated as a calibration constant combining various constants in the derivation process. The model uses a value of C_n obtained by calibrating the yield [3, 20] at an experimental point of 0.5 MA.

The D–D cross-section is highly sensitive to the beam energy so it is necessary to use the appropriate range of beam energy to compute σ. The code computes V_{max} of the order of 20–50 kV. However, it is known from experiments that the ion energy responsible for the beam–target neutrons is in the range 50–150 keV [2], and for smaller lower-voltage machines the relevant energy [18] could be lower at 30–60 keV. Thus, to align with experimental observations the D–D cross section σ is reasonably fitted by using beam energy equal to three times V_{max}. With this fitting it is found [20] that the computed neutron yield agrees with experimental measurements over a wide range of plasma focus machines from the small (sub-kJ) PF400 to the large (MJ) PF1000.

3. Procedures for the numerical experiments

The Lee code is configured to work as any plasma focus by inputting the bank parameters L_0, C_0 and stray circuit resistance r_0, the tube parameters b, a and z_0 and operational parameters V_0 and P_0 and the fill gas. The standard practice is to fit the computed total current waveform to an experimentally measured total current waveform [3, 16, 17, 20–22] using four model

parameters representing the mass swept-up factor f_m, the plasma current factor f_c for the axial phase and factors f_{mr} and f_{cr} for the radial phases.

From experience it is known that the current trace of the focus is one of the best indicators of gross performance. The axial and radial phase dynamics and the crucial energy transfer into the focus pinch are among the important information that is quickly apparent from the current trace.

The exact time profile of the total current trace is governed by the bank parameters, by the focus tube geometry and the operational parameters. It also depends on the fraction of the mass swept up and the fraction of sheath current and the variation of these fractions through the axial and radial phases. These parameters determine the axial and radial dynamics, specifically the axial and radial speeds which in turn affect the profile and magnitudes of the discharge current. The detailed profile of the discharge current during the pinch phase also reflects the Joule heating and radiative yields. At the end of the pinch phase the total current profile also reflects the sudden transition of the current flow from a constricted pinch to a large column flow. Thus, the discharge current powers all dynamic, electrodynamic, thermodynamic and radiation processes in the various phases of the plasma focus. Conversely all the dynamic, electrodynamic, thermodynamic and radiation processes in the various phases of the plasma focus affect the discharge current. It is then no exaggeration to say that the discharge current waveform contains information on all the dynamic, electrodynamic, thermodynamic and radiation processes that occur in the various phases of the plasma focus. This explains the importance attached to matching the computed current trace to the measured current trace in the procedure adopted by the Lee model code.

A measured current trace of PF1000 with $C_0 = 1332\,\mu$F, operated at 27 kV, 3.5 Torr deuterium, has been published [2], with cathode/anode radii $b = 16$ cm, $a = 11.55$ cm and anode length $z_0 = 60$ cm. In the numerical experiments we fitted the external (or static) inductance $L_0 = 33.5$ nH and the stray resistance $r_0 = 6.1\,\text{m}\Omega$ (damping factor RESF = stray resistance/$(L_0/C_0)^{0.5} = 1.22$). The fitted model parameters are $f_m = 0.13$, $f_c = 0.7$, $f_{mr} = 0.35$ and $f_{cr} = 0.65$. The computed current trace [20, 22] agrees very well with the measured trace through all the phases, axial and radial, right down to the bottom of the current dip indicating the end of the pinch phase. This agreement confirms the model parameters for PF1000. Once the model parameters have been fitted to a machine for a given gas, these model parameters may be used with some degree of confidence when operating parameters such as the voltage are varied [6]. With no measured current waveforms available for the higher megajoule numerical experiments, it is reasonable to keep the model parameters that we have got from the PF1000 fitting.

4. Discrepancies between the N&P scenario and our numerical experiments

We now examine the case of PF1000 at $C_0 = 1332\,\mu$F, which has an E_0 of 0.82 MJ at 35 kV. According to the N&P scenario, for this case with $b/a = 1.39$ and $v_a = 10^5\,\text{m s}^{-1}$, the final tube inductance works out at $L_a = (10^{-7}\pi v_a \ln(b/a))^2 C_0 = 144$ nH, and since the coaxial section with $b/a = 1.39$ has an inductance per unit length of $2 \times 10^{-7}\ln(b/a) = 0.66 \times 10^{-7}\,\text{H m}^{-1}$ or $0.66\,\text{nH cm}^{-1}$, then $z_0 = 218$ cm using the N&P scenario. In the actual case PF1000 is operated in the laboratory at a typical experimentally optimized length of 60 cm [2].

Our numerical experiments show an optimum length of $z_0 = 50$ cm, in near agreement with the laboratory operation. In the numerical experiments if z_0 is taken to be the N&P scenario value of 218 cm, both the pinch current and the Y_n are far below optimum. The difference becomes even clearer in the next example.

Table 1. Numerical experiments to optimize Y_n by varying z_0 for fixed $C_0 = 399\,60\,\mu$F.

z_0 (cm)	a (cm)	I_{peak} (kA)	I_{pinch} (kA)	Y_n (10^{10})
6480	11.95	4227	933	53.4
1000	21.50	5463	2208	1102
800	22.29	5548	2282	1211
600	23.12	5634	2345	1298
500	23.55	5678	2368	1320
400	23.91	5715	2378	1307
350	24.05	5729	2375	1280
274	24.15	5739	2355	1206

We look at another case of even larger $C_0 = 39960\,\mu$F, 30 times bigger than PF1000, with an E_0 of 24.5 MJ at 35 kV. According to the N&P scenario $L_a = 4278$ nH and $z_0 = 64.8$ m. We note that these figures for L_a and z_0 are 30 times bigger than for PF1000, since the crux of the N&P scenario is simply that L_a is proportional to C_0.

We carried out numerical experiments which show that the matching conditions proposed by Nukulin and Polukhin give very poor results. We compute that the length for optimum Y_n is $z_0 = 500$ cm, which practically corresponds to the optimum length for I_{pinch}. Table 1 shows the results of this series of experiments with $C_0 = 39960\,\mu$F, varying z_0 to find the optimum. For each z_0, 'a' is varied so that the end axial speed is 10 cm μs^{-1}. It is clear that one would not operate at the N&P scenario $z_0 = 6480$ cm, for which case the current has dropped so low that I_{pinch} only attains 933 kA with Y_n of only 5.3×10^{11}, compared with the numerically computed optimum Y_n of 1.32×10^{13} at $z_0 = 500$ cm with I_{pinch} of 2.37 MA.

5. Explaining the discrepancy

We look for the explanation of the discrepancy between the N&P scenario and our numerical experiments. To do this we plot in figure 1 Case 1 which depicts the time scale for the case in which a discharge occurs with $C_0 = 39960\,\mu$F and a constant inductance $L = 4260$ nH according to the N&P scenario. In the same figure we plot Case 2 which is the discharge current computed from our model code with $C_0 = 39960\,\mu$F and a length of $z_0 = 6480$ cm, the required matching length as envisaged by the N&P scenario. Case 3 is the computed discharge current for $z_0 = 500$ cm, corresponding to line 5 of table 1, which is the optimum length, producing maximum Y_n of 1.3×10^{13} and a nearly optimum I_{pinch} of 2.37 MA. In both Case 2 and Case 3 the anode radius 'a' has been adjusted to give a final axial speed (end axial phase) of 10 cm us^{-1}.

If the discharge current were to have the time profile as shown in Case 1 of figure 1, then an axial rundown time of 600 μs would be appropriate, with a corresponding z_0 of around 6480 cm, reaching the radial phase just when the current was peaking. Such a situation would justify the N&P scenario. However, computation using the model code shows that the actual current profile using a matching $z_0 = 6480$ cm as envisaged by the N&P scenario is that of Case 2 with the current peaking at 4.2 MA at just 19 μs; thereafter the current profile droops, dropping to below 2 MA as the current sheet moves into the radial phase. Because of the severe drop in the total current, I_{pinch} is only 0.93 MA producing Y_n of 5.3×10^{11}. With such a current profile it is clearly better to have a shorter z_0, so that the pinch could be allowed to occur much earlier before the current has dropped too much. As seen in the results of table 1, the optimum z_0 is in fact found to be 500 cm with $Y_n = 1.3 \times 10^{13}$. The current profile corresponding to

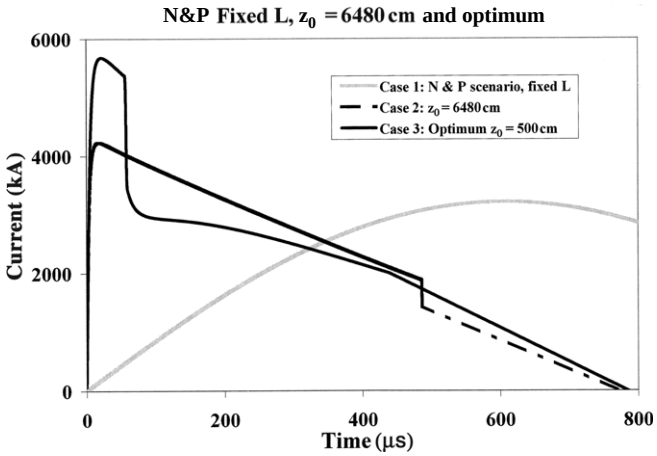

Figure 1. Current waveform for the N&P scenario (Case 1) compared with computed waveform using N&P matching $z_0 = 6480$ cm (Case 2). Also shown is the computed current waveform for optimum $z_0 = 500$ cm (Case 3).

this optimum is shown in Case 3 of figure 1. Thus, figure 1 shows that the conclusion of the N&P scenario that the tube inductance and tube length should grow proportionately with C_0, for large C_0, is not correct. This effectively invalidates their argument for I_{peak} saturation and hence also Y_{n} saturation.

Looking more closely at the numerical results we note that the risetime to I_{peak} is only 19 μs, which is less than the short circuit rise time of $(\pi/2)(L_0C_0)^{0.5} \sim 58\,\mu$s. At this time of 19 μs, the axial speed has already reached 9.9 cm us^{-1}. At that speed, the dynamic resistance $0.5(\mathrm{d}L/\mathrm{d}t) = 10^{-7}\ln(b/a)v_z = 3.3\,\text{m}\Omega$, which is dominant when compared with the bank stray resistance of 1.1 mΩ and short circuit surge impedance of 0.9 mΩ, even if we consider that at this time the current sheet has traveled 140 cm adding another 92 nH to the circuit, so that at this time the effective surge impedance is 1.7 mΩ. It can then be seen that the dynamic resistance is the controlling factor and it is the small initial inductance coupled with the rapid increase in dynamic resistance which causes this early peaking and subsequent flattening and droop of the discharge current. We also note that this dominance of the dynamic resistance occurs only at large C_0; and the larger the C_0, the more the dominance. At small C_0, for example, at 100 μF, the short circuit impedance is 18 mΩ, whilst the dynamic resistance is unchanged at 3.3 mΩ. In those cases of lower C_0, no early peaking followed by subsequent drooping flat-top is observed.

This early peaking and subsequent current droop invalidate the N&P scenario.

We now describe the numerical experiments which show how I_{peak}, I_{pinch} and Y_{n} vary with C_0.

6. Numerical experiments at 35 kV, 10 Torr, L_0 = 33.5 nH, RESF = 1.22 and b/a = 1.39, varying C_0- No saturation observed

The numerical experiments are then carried out for a range of C_0. The pressure is fixed at $P_0 = 10$ Torr deuterium. The results are shown in figures 2–5. From these figures we see that as E_0 is increased by increasing C_0, from 8.5 kJ to 25 MJ, there is no saturation in I_{peak}, I_{pinch} or Y_{n} as functions of C_0 or E_0.

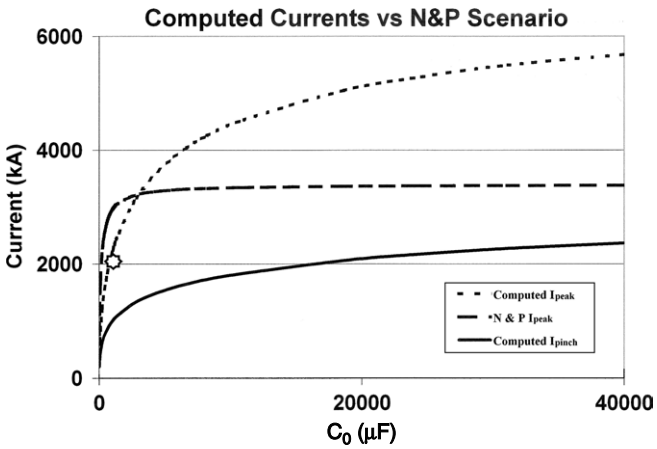

Figure 2. I_{peak} (top trace) computed from numerical experiments as a function of C_0, compared to I_{peak} envisaged by N&P scenario (middle trace). Also shown is the I_{pinch} curve (lower trace). The single point at the 2 MA level is an experimental PF1000 point [23].

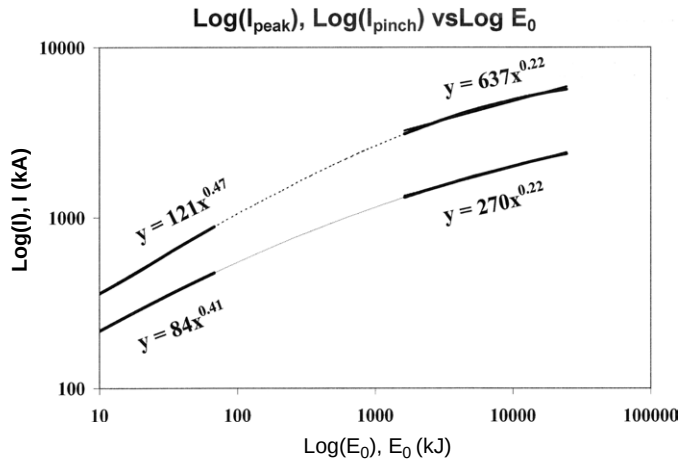

Figure 3. Log I_{peak} (top curve) and Log I_{pinch} versus Log E_0, showing no saturation for E_0 up to 25 MJ.

Figure 2 shows the computed I_{peak} as a function of C_0, from our numerical experiments compared with that postulated by the N&P scenario. The important difference is that whereas the N&P scenario shows I_{peak} saturation, our numerical experiments show no saturation; although there is a scaling shift from $I_{peak} \sim E_0^{0.47}$ to $I_{peak} \sim E_0^{0.22}$ which is seen when plotted on log–log scale (see figure 3).

More importantly, the I_{pinch} scaling with E_0 shows a similar slowdown from $I_{pinch} \sim E_0^{0.41}$ to $I_{pinch} \sim E_0^{0.22}$ (see figure 3), but again no saturation. As was shown in earlier papers [3, 20–22] it is the I_{pinch} scaling, rather than I_{peak} , which directly affects the neutron yield scaling.

For this series of experiments we find that the Y_n scaling changes from $Y_n \sim E_0^{2.0}$ at tens of kJ to $Y_n \sim E_0^{0.84}$ at the highest energies (up to 25 MJ) investigated in this series. This is shown in figure 4(*a*). Figure 4(*b*) shows the values of z_0, optimized for the neutron yield and

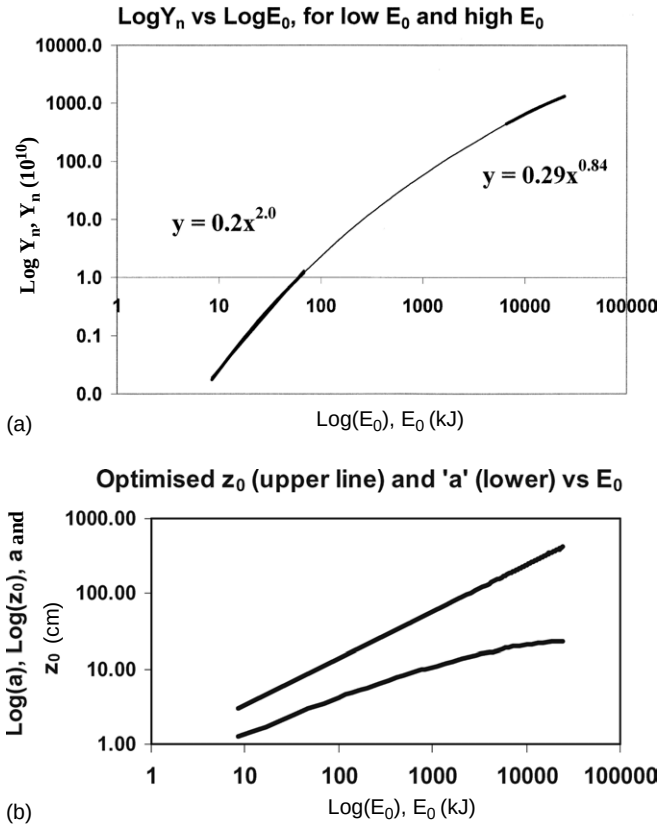

Figure 4. (*a*) Y_n plotted as a function of E_0 in log–log scale, showing no saturation of the neutron yield up to 25 MJ, the highest energy investigated. (*b*). Optimized z_0 and '*a*' versus E_0 for the numerical experiments of (*a*).

the corresponding value of '*a*' for an end axial speed of 10 cm μs^{-1}. These anode dimensions are used in the numerical experiments recorded in figure 4(*a*).

Because of the way Y_n versus E_0 scaling slows down at the megajoule level and the corresponding way I_{peak} and I_{pinch} scaling also slow down, the scaling of Y_n with I_{peak} and I_{pinch} over the whole range of energies investigated up to 25 MJ (figure 5) is as follows:

$Y_n = 3.2 \times 10^{11} I_{pinch}^{4.5}$; $\quad Y_n = 1.8 \times 10^{10}\, I_{peak}^{3.8}$ where I_{peak} and I_{pinch} are in MA.

In this scaling, I_{peak} ranges from 0.3 to 5.7 MA and I_{pinch} ranges from 0.2 to 2.4 MA.

7. Numerical experiments to attain $Y_n = 10^{13}$ D–D neutrons per shot, using a less resistive bank of RESF = 0.12

Gribkov *et al* [24] had pointed out that $Y_n = 10^{13}$ in deuterium is a desired landmark to achieve in a plasma focus device, from the point of view of possible exploitation as a powerful source of *fusion* neutrons for testing of prospective materials for the first wall components and construction elements in magnetic confinement fusion and, especially, in inertial confinement fusion reactors. Converting such a plasma focus yield to operation in D–T with $Y_n = 10^{15}$ could produce, during a one-year run, an overall fluence of the order of 0.1–1.0 dpa for such

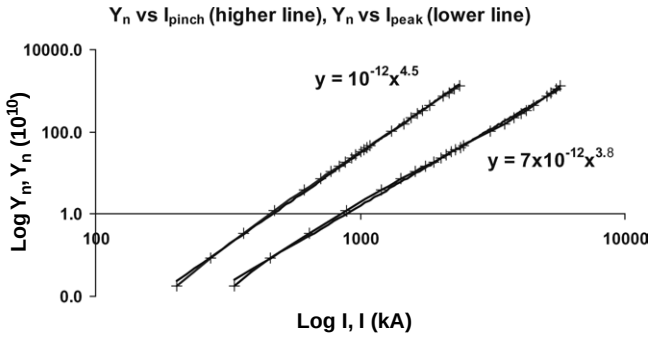

Figure 5. Log(Y_n) scaling with Log(I_{peak}) and Log(I_{pinch}), for the range of energies investigated, up to 25 MJ.

testing purposes, at a very low cost relative to other methods currently being considered. We now examine the requirements to reach this landmark.

In the above series of numerical experiments we have shown that Y_n does not saturate with increasing E_0 at the megajoule level. The scaling does deteriorate from $Y_n \sim E^2$ to a relationship closer to $Y_n \sim E_0$ Nevertheless, because of the non-saturation, $Y_n = 10^{13}$ is achieved at 18–19 MJ (see figure 4(*a*)) with I_{peak} and I_{pinch} of 5.5 MA and 2.3 MA, respectively.

However, in the above experiments the capacitor bank was assigned a relatively large resistance r_0 with RESF $= r_0/(L_0/C_0)^{0.5}$ of 1.22, which is an unusually high damping factor associated with PF1000. With a modern bank we should be able to have a less highly damped bank with an RESF of say 0.12.

We repeat the above experiments with the RESF changed to 0.12, representative of a higher performance modern capacitor bank. We keep $c = b/a = 1.39$ and $P_0 = 10$ Torr Deuterium. We obtain results which are summarized in figure 6(*a*).

These results show that using a less resistive modern bank reduces the E_0 required to reach $Y_n = 10^{13}$ in deuterium to some 8 MJ with I_{peak} and I_{pinch} of 6 MA and 2.3 MA, respectively. Figure 6(*b*) shows the optimized geometry required for the numerical experiments of figure 6(*a*).

8. Investigating the role of pressure, electrode ratios and static inductance L_0

We want to investigate the effect of increase in V_0 [1, 2]. A preliminary run at $C_0 = 1332\,\mu$F under the conditions of figure 6(*a*) shows that as V_0 is increased from 35 to 90 kV, Y_n increases substantially to above 2×10^{13}. The indications are that at 90 kV, C_0 in the region 700–800 μF would be sufficient to produce $Y_n = 10^{13}$ in deuterium. However, before we finalise these numerical experiments, varying V_0, we need to fix practical optimum conditions in pressure, radius ratio and static inductance L_0.

We vary the pressure from 1 Torr upwards in suitable steps, adjusting z_0 and 'a' for optimum Y_n at each P_0, with the requirement that the end axial speed is maintained at 10 cm us^{-1}. Then we look for the optimum over the range of pressures. We find the following. At $E_0 = 1332\,\mu$F, Y_n peaks at 10 Torr. As E_0 is increased, the optimum P_0 increases. At the highest energy investigated there is a factor of 3 in Y_n between 10 and 60 Torr, with Y_n still increasing above 60 Torr. However, at this point we consider the technical situation [25] regarding the current per unit radius, I_{peak}/a. The factor controlling speed is $S = (I_{peak}/a)/P_0^{0.5}$ [11]. Hence, at any I_{peak}, as P_0 is increased, to maintain the end axial speed

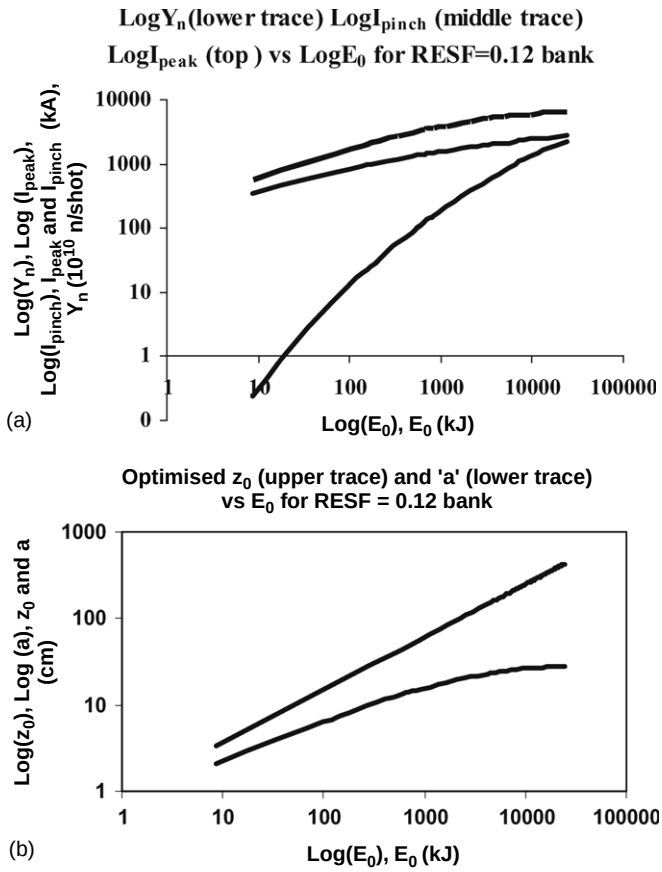

Figure 6. (*a*) Log–log plots of Y_n (lower trace), I_{pinch} (middle trace) and I_{peak} (top trace) versus E_0 for a high performance bank up to 25 MJ; computed from numerical experiments. (*b*) Optimised electrode geometry used in numerical experiments of (*a*).

of 10 cm us^{-1}, (I_{peak}/a) has to be increased by reducing 'a'. At 10 Torr, (I_{peak}/a) is in the region 250–300 kA cm^{-1} over the range of energies investigated. At $P_0 = 60$ Torr, (I_{peak}/a) needs to be increased by a factor nearly 2.5. From this technical aspect, for this exercise, we set a limit of 300 kA cm^{-1}. Hence, from this point of view we keep the pressure at 10 Torr for all our higher E_0 experiments, knowing that to go lower in P_0 would move the operational point further from optimum and sacrificing the move closer to optimum at higher P_0 in order not to exceed (I_{peak}/a) of 300 kA cm^{-1}. We make a note here that if we can improve anode materials technology to withstand (I_{peak}/a) greater than 300 kA cm^{-1}, then, in that case, the following results would be conservative and may be upgraded accordingly.

We next vary the radius ratio $c = b/a$. We start with the optimum condition which we have found for $C_0 = 1332\,\mu$F. At each value of 'c', we adjusted the values of 'a' and z_0 for optimum. We vary 'c' from 1.2 to 1.6 and find that 1.39 is at the optimum. It appears that the radius ratio $c = 1.39$ used in PF1000 [2] had already been very well chosen.

We next examine the choice of L_0. It had been shown [3, 22] that for a fixed C_0, if L_0 is reduced, there is a range of L_0 at which I_{pinch} reaches a flat maximum. There is no advantage lowering L_0 below this range; indeed I_{pinch} would suffer a slight decrease, due to

Table 2. Numerical experiments on effect of increasing V_0, at fixed C_0 of 777 μF.

V_0 (kV)	E_0 (kJ)	b (cm)	a (cm)	z_0 (cm)	I_{peak} (kA)	I_{pinch} (kA)	Y_n (10^{10})
90	3147	39.92	27.65	25	7580	2483	1228
70	1904	31.14	22.40	30	5955	2091	631
50	971	23.44	16.86	35	4365	1652	246
35	476	16.69	12.01	37	3074	1286	88

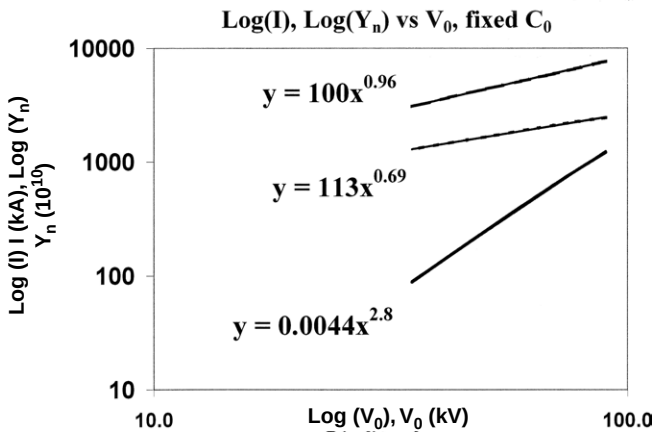

Figure 7. Scaling of currents and Y_n as functions of operating voltage V_0. Top curve: Log(I_{peak}), middle curve: Log(I_{pinch}) and bottom curve: Log(Y_n).

this focus pinch current limitation. Looking at the range of large E_0 we are dealing with in these experiments we find that a good compromise value of L_0 is 36 nH which ensures optimum I_{pinch}.

In consideration of the above we fixed optimum values of $L_0 = 36$ nH, $c = b/a = 1.39$ and settled on $P_0 = 10$ Torr (for the highest pressure whilst keeping the technical condition of not exceeding 300 kA cm^{-1}). We consider these as the practical optimum conditions.

9. Investigating the effect on Y_n as operating voltage is increased from 35 to 90 kV, at C_0 = 777 μF

We next run numerical experiments at practical optimum conditions $c = b/a = 1.39$, $L_0 = 36$ nH, $P_0 = 10$ Torr. We keep C_0 at 777 μF and vary V_0 from 35 to 90 kV. The results are summarized in table 2. The results are also plotted in figure 7 in log–log scale.

Figure 7 shows that $Y_n \sim V_0^{2.8}$ over the range of voltages examined from 35 to 90 kV.

Looking at this scaling, it may at first sight be tempting to think in terms of increasing the voltage further. However, it is then necessary to look more closely at that prospect. An examination of the computed results shows that the computed effective beam energy [3,20,22] for 90 kV is already at the 330 keV level. Looking at data for the D–D cross-section [26] as a function of the beam energy, it is seen that above 300 keV, the rise in the D–D fusion cross-section is very slow. Hence, there is little advantage operating above 90 kV. In fact, the situation is actually disadvantageous to increasing the operating voltage if one considers changing to D–T operation. The D–T fusion cross-section [26] has already peaked at 120 keV,

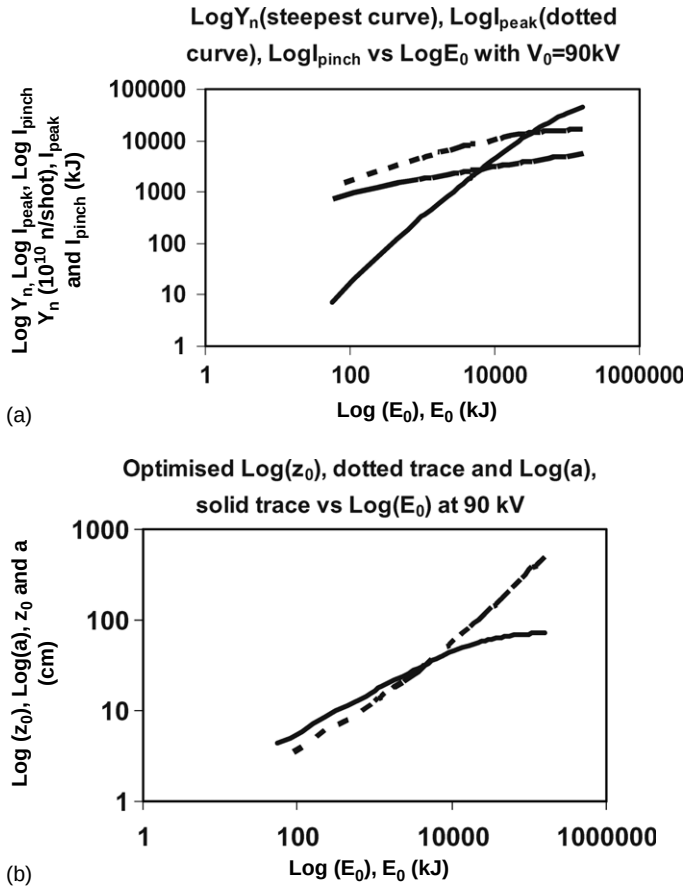

Figure 8. (*a*) Numerical experiments at 90 kV, varying C_0, to obtain scaling of I_{peak}, I_{pinch} and Y_{n} with E_0. Log(Y_{n}): steepest curve; Log(I_{peak}): dotted curve; Log(I_{pinch}): other curve. Y_{n} in units of 10^{10} D–D neutrons/shot; I_{peak} and I_{pinch} in kA. (*b*) Optimized geometry corresponding to numerical experiments for (*a*).

and operating at 90 kV with the beam energy at 330 keV, the beam energy is already too high, the D–T cross-section having dropped by a factor of around 3.6 from its peak. It seems then that from this point of view there is no advantage in operating a plasma focus at higher than 90 kV. For conversion to D–T operation it would probably be better to operate at a lower voltage. It would then be necessary to increase C_0 until 10^{15} D–T neutrons is reached.

10. Investigating operation at 90 kV, varying E_0, by varying C_0; at 10 Torr, L_0 = 36 nH and b/a = 1.39; RESF = 0.12

We consider the effect of operating at 90 kV. We run experiments at 90 kV with increasing E_0 (by increasing C_0) to obtain the energy required to reach $Y_{\text{n}} = 10^{13}$ D–D neutrons per shot. At each C_0, z_0 is varied whilst adjusting 'a' for an end axial speed of 10 cm us^{-1}. The optimum z_0 is thus found for each C_0 (E_0). The results are shown in figure 8(a). Again at this higher voltage, no saturation is found for I_{peak}, I_{pinch} or Y_{n}. At 90 kV we confirm we are able to reduce the E_0 required for $Y_{\text{n}} = 10^{13}$ D–D fusion neutrons per shot to 3 MJ, with $C_0 = 777\,\mu$F as

shown in figure 8(*a*). The values of I_{peak} and I_{pinch} are, respectively, 7.6 MA and 2.5 MA. The required anode geometry is also shown in figure 8(*b*).

Furthermore, at 90 kV with the highest value of C_0 investigated as 39960 μF, the storage energy is 162 MJ. At that storage energy, optimized Y_{n} is 4.5×10^{14} D–D neutrons/shot with $I_{\text{peak}} = 17.3$ MA and $I_{\text{pinch}} = 5.7$ MA.

11. Conclusion

This paper shows that the N&P scenario is erroneous in its conclusion regarding the saturation of Y_{n} at megajoule energies as E_0 is increased by the increase in C_0. The N&P scenario contends that this saturation is due to electrodynamic effects. Our numerical experiments show that the scaling of L_{a} and z_0 envisaged by the N&P scenario is far from the optimum. Laboratory experiments at the 1 MJ level as reported in the literature have been carried out close to the optimum as confirmed by our numerical experiments. The numerical experiments show no saturation in I_{peak}, I_{pinch} or Y_{n} that may be traced to the electrodynamics governing the system, although there is a slowing down of scaling at high E_0, e.g. $Y_{\text{n}} \sim E_0^2$ at low energies and $Y_{\text{n}} \sim E_0^{0.84}$ at high megajoule levels. Thus, any saturation of Y_{n} with E_0 (as C_0 is increased) cannot be ascribed to the physics governing the electrodynamics of the system. Other, possibly machine-related, effects outside the scope of this paper may have to be investigated to account for the apparently observed saturation effects. In connection with this it may be pointed out that the drop in scaling for Y_{n} below E_0 is a significant disappointment from the point of view of scaling for fusion energy production purposes.

This paper finds that scaling up from a PF1000-like capacitor bank requires close to 19 MJ to reach a target D–D neutron yield of 10^{13} per shot. However, the numerical experiments also find that a modern bank with typical lower damping may achieve the same target D–D neutron yield of 10^{13} at 8 MJ operating at a typical voltage of 35 kV. The energy requirement is further reduced to 3 MJ by increasing the operational voltage to 90 kV. Because of the high effective beam energy already at 90 kV, there is little advantage in operating at voltages above 90 kV for the D–D neutron yield.

References

[1] Nukulin V Ya and Polukhin S N 2007 *Plasma Phys. Rep.* **33** 271–7
[2] Gribkov V A *et al* 2007 *J. Phys. D: Appl. Phys.* **40** 3592
[3] Lee S and Saw S H 2008 *Appl. Phys. Lett.* **92** 021503
[4] Gourland C *et al* 1978 *Preprint No* 78.12/cc (Roma: CNEN Frascati Center)
[5] Bernard A *et al* 1978 *J. Physique Coll. C1 (Suppl. 5)* **39** C1
[6] Lee S *Radiative Dense Plasma Focus Computation Package: RADPF* http://www.intimal.edu.my/school/fas/UFLF/
[7] Lee S 1984 *Radiations in Plasmas* ed B McNamara (Singapore: World Scientific) pp 978–87
[8] Lee S *et al* 1988 *Am. J. Phys.* **56** 62
[9] Tou T Y, Lee S and Kwek K H 1989 *IEEE Trans. Plasma Sci.* **17** 311
[10] Lee S 1991 *IEEE Trans. Plasma Sci.* **19** 912
[11] Lee S and Serban A 1996 *IEEE Trans. Plasma Sci.* **24** 1101–5
[12] Potter D E 1971 *Phys. Fluids* **14** 1911
[13] Liu M H, Feng X P, Springham S V and Lee S 1998 *IEEE Trans. Plasma Sci.* **26** 135–40
[14] Lee S, Lee P, Zhang G, Feng X, Gribkov V A, Liu M, Serban A and Wong T 1998 *IEEE Trans. Plasma Sci.* **26** 1119
[15] Bing S 2000 Plasma dynamics and x-ray emission of the plasma focus *PhD Thesis* NIE ICTP Open Access Archive: http://eprints.ictp.it/99/
[16] Lee S 2000–2007 http://ckplee.myplace.nie.edu.sg/plasmaphysics/
[17] Lee S 2005 ICTP Open Access Archive: http://eprints.ictp.it/85/

[18] Lee S 1998 *Twelve Years of UNU/ICTP PFF—A Review IC* 98 (231) Abdus Salam ICTP, Miramare, Trieste; *ICTP OAA*: http://eprints.ictp.it/31/
[19] Siahpoush V, Tafreshi M A, Sobhanian S and Khorram S 2005 *Plasma Phys. Control. Fusion* **47** 1065
[20] Lee S and Saw S H 2008 Neutron scaling laws from numerical experiments *J. Fusion Energy* at press
[21] Lee S, Saw S H, Lee P C K, Rawat R S and Schmidt H 2008 *Appl. Phys. Lett.* **92** 111501
[22] Lee S, Lee P, Saw S H and Rawat R S 2008 *Plasma Phys. Control. Fusion* **50** 065012
[23] Sadowski M J and Scholz M 2002 *Nukleonika* **47** 31–7
[24] Gribkov V A *et al* 2007 *J. Phys. D: Appl. Phys.* **40** 1977
[25] Gribkov V A 2003 private communication
[26] Huba J D 2006 *Plasma Formulary* p 44 http://wwwppd.nrl.navy.mil/nrlformulary/NRL_FORMULARY_07.pdf

Research Results of Plasma Focus Numerical Experiments

S LEE[1,2,3], S H SAW[2,4]
[1]*Institute for Plasma Focus Studies, 32 Oakpark Drive, Chadstone, VIC 3148, Australia*
[2]*INTI International University College, 71800 Nilai, Malaysia*
[3]*Nanyang Technology University, National Institute of Education, Singapore 637616*
[4]*University of Malaya, Kuala Lumpur, Malaysia*

e-mail: leesing@optusnet.com.au

Abstract

The Lee Model couples the electrical circuit with plasma focus dynamics, thermodynamics, and radiation. A phenomenological beam-target neutron generating mechanism is included in the code to provide information on the neutron yield. The Lee Model is extensively used to design and simulate experiments. This paper provides an overview of recent published results from numerical experiments carried out using the Lee Model. The results are: (1) a previously unsuspected "pinch current limitation" effect; (2) the existence of an optimum L_o below which the pinch current and neutron yield of that plasma focus would not increase, but instead decreases; (3) a realistic neutron yield scaling with pinch current; and (4) an innovative tool to obtain the pinch current. A dominant thread running through the research papers is that the pinch current has to be distinguished from the discharge peak current in the analysis and scaling of plasma focus experiments.

1. Introduction

The Lee Model in its two-phase form was described in 1984 [1]. It was used to assist in the design and interpretation of several experiments [2–4]. An improved five-phase model and code incorporating finite small disturbance speed [5] and radiation coupling with dynamics assisted several projects [6–8] and was web published [9] in 2000 and in 2005 [10]. Plasma self-absorption was included [9] in 2007. It has been used extensively as a complementary facility in several machines, for example, UNU/ICTP PFF [2,6] the NX2 [7,8] NX1 [7] and DENA [11]. It has also been used [12] in other machines for design and interpretation including Soto's sub-kilojoule plasma focus machines [13] FNII [14] and the UBA hard x-ray source [15]. Information obtained from the model includes axial and radial velocities and dynamics [1,7,11,12], soft x-ray (SXR) emission characteristics and yield [6-8,16], design of machines [13,16], optimization of machines, and adaptation to other machine types such as the Filippov-type DENA [11]. A study of speed-enhanced neutron yield [17] was also assisted by the Lee Model code.

A detailed description of the Lee Model is already available on the internet [9,10]. A recent development in the code is the inclusion of neutron yield using a phenomenological beam-target neutron generating mechanism [18] incorporated in the present RADPFV5.13 [19]. This improved model has been used to discover the pinch limitation effect [20], the existence of an optimum L_o below which the pinch current and neutron yield of that plasma focus would not increase, but instead decrease [21], a realistic neutron yield scaling with pinch current [22] and has been proven to be an innovative tool to obtain the pinch current [23].

2. The numerical experiments

Numerical experiments were carried out on plasma focus machines for which reliable current traces and neutron yields are available. The experiment was applied to several machines including the PF400, UNU/ICTP PFF, the NX2 and Poseidon. The PF1000 which has a current curve published at 27kV and Y_n published at 35kV provided an important point.

Keynote address delivered by S H Saw at International Conference on Plasma Computation and Applications IWPCA2008, Kuala Lumpur on 14 July 2008

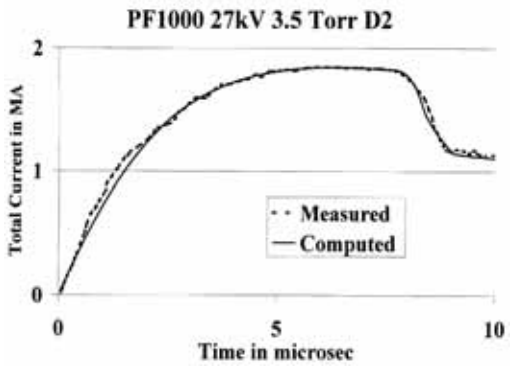

Figure 1. PF1000 at 27kV measured (dashed line) vs computed (smooth line) current traces.

Figure 1 shows a comparison of the computed total current trace (solid smooth line) with the experimental trace (dotted line) of the PF1000 at 27 kV at 3.5 Torr Deuterium, with outer/inner radii b=16 cm, a=11.55 cm, and anode length z_o=60 cm. In the numerical experiments we fitted external or static inductance L_o=33 nH and stray resistance r_o=6 mΩ with model parameters mass factor, current factor, and radial mass factor as f_m=0.14, f_c=0.7, and f_{mr}=0.35. The computed current trace agrees very well with the experiment, a typical performance of this code.

Each numerical experiment is considered satisfactory when the computed current trace matches the experiment in current rise profile and peak current, in time position of the current dip, in slope, and absolute value of the dip (see Figure 1). Once this fitting is done our experience is that the other computed properties including dynamics, energy distributions and radiation are all realistic.

3. Pinch current limitation effect

In a recent paper [18] there was expectation that the large MJ plasma focus PF1000 in Warsaw could increase its discharge current, and its pinch current, and consequently neutron yield by a reduction of its external inductance L_o. To investigate this point experiments were carried out using the Lee Model code [19]. Unexpectedly, the results indicated that whilst I_{peak} indeed progressively increased with reduction in L_o, no improvement may be achieved due to a pinch current limitation effect [20, 21]. Given a fixed C_o powering a plasma focus, there exists an optimum L_o for maximum I_{pinch}. Reducing L_o further will increase neither I_{pinch} nor Y_n.

We carried out numerical experiments for PF1000 using the machine and model parameters determined from Figure 1, modified by information about values of I_{peak} at 35 kV. Operating the PF1000 at 35 kV and 3.5 Torr, we varied the anode radius a with corresponding adjustment to b to maintain a constant c=b/a in order to keep the peak axial speed at 10 cm/μs. The anode length z_o was also adjusted to maximize I_{pinch} as L_o was decreased from 100 nH progressively to 5 nH.

As expected, I_{peak} increased progressively from 1.66 to 4.4 MA. As L_o was reduced from 100 to 35 nH, I_{pinch} also increased, from 0.96 to 1.05 MA. However, then unexpectedly, on further reduction from 35 to 5 nH, I_{pinch} stopped increasing, instead decreasing slightly to 1.03 MA at 20 nH, to 1.0 MA at 10 nH, and to 0.97 MA at 5 nH. Y_n also had a maximum value of $3.2\text{x}10^{11}$ at 35 nH.

To explain this unexpected result, we examine the energy distribution in the system at the end of the axial phase (see Figure 1) just before the current drops from peak value I_{peak} and then again near the bottom of the almost linear drop to the pinch phase. The energy equation describing this current drop is written as follows:

$$0.5I_{\text{peak}}^2(L_o + L_a f_c^2) = 0.5I_{\text{pinch}}^2(L_o/f_c^2 + L_a + L_p) + \delta_{cap} + \delta_{plasma}, \quad (1)$$

where L_a is the inductance of the tube at full axial length z_o, δ_{plasma} is the energy imparted to the plasma as the current sheet moves to the pinch position and is the integral of $0.5(dL/dt)I^2$. We approximate this as $0.5L_pI_{pinch}^2$ which is an underestimate for this case. δ_{cap} is the energy flow into or out of the capacitor during this period of current drop. If the duration of the radial phase is short compared to the capacitor time constant, the capacitor is effectively decoupled and δ_{cap} may be put as zero. From this consideration we obtain

$$I_{pinch}^2 = I_{\text{peak}}^2(L_o + 0.5L_a)/(2L_o + L_a + 2L_p), \quad (2)$$

where we have taken f_c=0.7 and approximated $f_c^{\,2}$ as 0.5.

Generally, as L_o is reduced, I_{peak} increases; a is necessarily increased leading [17] to a longer pinch length z_p, hence a bigger L_p. Lowering L_o also results in a shorter rise time, hence a necessary decrease in z_o, reducing L_a. Thus, from Eq. (2), lowering L_o decreases the fraction I_{pinch}/I_{peak}. Secondly, this situation is compounded by another mechanism. As L_o is reduced, the L-C interaction time of the capacitor bank reduces while the duration of the current drop increases (see Fig 2, discussed in the next section) due to an increasing a. This means that as L_o is reduced, the capacitor bank is more and more coupled to the inductive energy transfer processes with the accompanying induced large voltages that arise from the radial compression. Looking again at the derivation of Eq. (2) from Eq. (1) a nonzero δ_{cap}, in this case, of positive value, will act to decrease I_{pinch} further. The lower the L_o the more pronounced is this effect.

Summarizing this discussion, the pinch current limitation is not a simple effect, but is a combination of the two complex effects described above, namely, the interplay of the various inductances involved in the plasma focus processes abetted by the increasing coupling of C_o to the inductive energetic processes, as L_o is reduced.

4. Optimum L_o for maximum pinch current and neutron yield

From the pinch current limitation effect, it is clear that given a fixed C_o powering a plasma focus, there exists an optimum L_o for maximum I_{pinch}. Reducing L_o further will increase neither I_{pinch} nor Y_n. The results of the numerical experiments carried out are presented in Figure 2 and Table 1.

With large L_o = 100 nH it is seen (Figure 2) that the rising current profile is flattened from what its waveform would be if unloaded; and peaks at around 12μs (before its unloaded rise time, not shown, of 18μs) as the current sheet goes into the radial phase. The current drop, less than 25% of peak value, is sharp compared with the current rise profile. At L_o = 30 nH the rising current profile is less flattened, reaching a flat top at around 5μs, staying practically flat for some 2μs before the radial phase current drop to 50% of its peak value in a time which is still short compared with the rise time. With L_o of 5 nH, the rise time is now very short, there is hardly any flat top; as soon as the peak is reached, the current waveform droops significantly. There is a small kink on the current waveform of both the L_o = 5 nH, z_o = 20 cm and the L_o = 5 nH, z_o = 40 cm. This kink corresponds to the start of the radial phase which, because of the large anode radius, starts with a relatively low radial speed, causing a momentary reduction in dynamic loading. Looking at the three types of traces it is seen that for L_o = 100 nH to 30 nH, there is a wide range of z_o that may be chosen so that the radial phase may start at peak or near peak current, although the longer values of z_o tend to give better energy transfers into the radial phase.

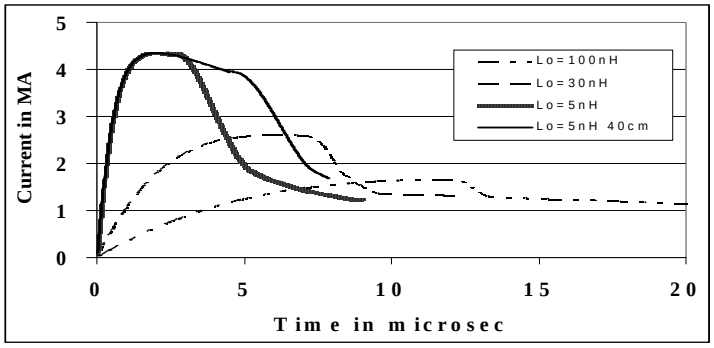

Figure 2. PF1000 current waveforms computed at 35kV, 3.5 Torr D2 for a range of L_o

The optimized situation for each value of L_o is shown in Table 1. The table shows that as L_o is reduced, I_{peak} rises with each reduction in L_o with no sign of any limitation. However, I_{pinch} reaches a broad maximum of 1.05MA around 40–30 nH. Neutron yield Y_{n} also shows a similar broad maximum peaking at 3.2×10^{11} neutrons. Figure 3 shows a graphical representation of this I_{pinch} limitation effect. The curve going up to 4MA at low L_o is the I_{peak} curve. Thus I_{peak} shows no sign of limitation as L_o is progressively reduced. However I_{pinch} reaches a broad maximum. From Figure 3 there is a stark and important message.

One must distinguish clearly between I_{peak} and I_{pinch}. In general one cannot take I_{peak} to be representative of I_{pinch}.

Table 1. Effect on currents and ratio of currents as L_o is reduced-PF1000 at 35kV, 3.5 Torr Deuterium

L_0(nH)	b(cm)	a(cm)	z_0(cm)	I_{peak}(MA)	I_{pinch}(MA)	$Y_n(10^{11})$	I_{pinch}/I_{peak}
100	**15.0**	**10.8**	**80**	**1.66**	**0.96**	**2.44**	**0.58**
80	**16.0**	**11.6**	**80**	**1.81**	**1.00**	**2.71**	**0.55**
60	**18.0**	**13.0**	**70**	**2.02**	**1.03**	**3.01**	**0.51**
40	**21.5**	**15.5**	**55**	**2.36**	**1.05**	**3.20**	**0.44**
35	**22.5**	**16.3**	**53**	**2.47**	**1.05**	**3.20**	**0.43**
30	**23.8**	**17.2**	**50**	**2.61**	**1.05**	**3.10**	**0.40**
20	**28.0**	**21.1**	**32**	**3.13**	**1.03**	**3.00**	**0.33**
10	**33.0**	**23.8**	**28**	**3.65**	**1.00**	**2.45**	**0.27**
5	**40.0**	**28.8**	**20**	**4.37**	**0.97**	**2.00**	**0.22**

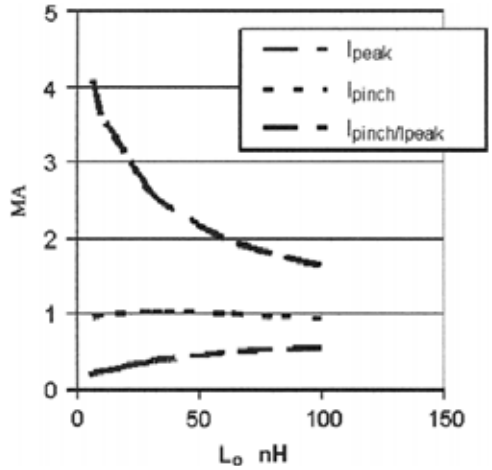

Figure 3. Effect on currents and current ratio (computed) as *L*o is reduced-PF1000, 35 kV, 3.5 torr D_2.

We carried out several sets of experiments on the PF1000 for varying L_o, each set with a different damping factor. In every case, an optimum inductance was found around 30–60 nH with I_{pinch} decreasing as L_o was reduced below the optimum value. The results showed that for PF1000, reducing L_o from its present 20–30 nH will increase neither the observed I_{pinch} nor the neutron yield, because of the pinch limitation effect.

5. Neutron yield scaling with pinch current

The main mechanism producing the neutrons is a beam of fast deuteron ions interacting with the hot dense plasma of the focus pinch column. The fast ion beam is produced by diode action in a thin layer close to the anode with plasma disruptions generating the necessary high voltages. This mechanism, described in some details in a recent paper [18], results in the following expression [22] used for the Lee Model code:

$$Y_{b\text{-}t} = \text{calibration constant} \times n_i I_{pinch}^{\ 2} z_p^{\ 2} (\ln(b/r_p))\sigma/V_{max}^{\ 0.5} \qquad (3)$$

where I_{pinch} is the current at the start of the slow compression phase, r_p and z_p are the pinch radius and pinch length at the end of the slow compression phase, V_{max} is the maximum value attained by the inductively induced voltage and σ is the D-D fusion cross section (n branch) [24] corresponding to the beam ion energy. The D-D cross section σ is obtained by using beam energy equal to 3 times V_{max}, to conform to experimental observations [25].

Experimental data [26,27] of neutron yield Y_n against pinch current I_{pinch} is assembled (see Figure 4) to produce a more global scaling law than available. It must be noted that there is no clear distinction shown in the literature of I_{pinch} , I_{peak} and I_{total}. From the data a mid-range point is obtained to calibrate the neutron production mechanism of the Lee Model code (Figure 4).

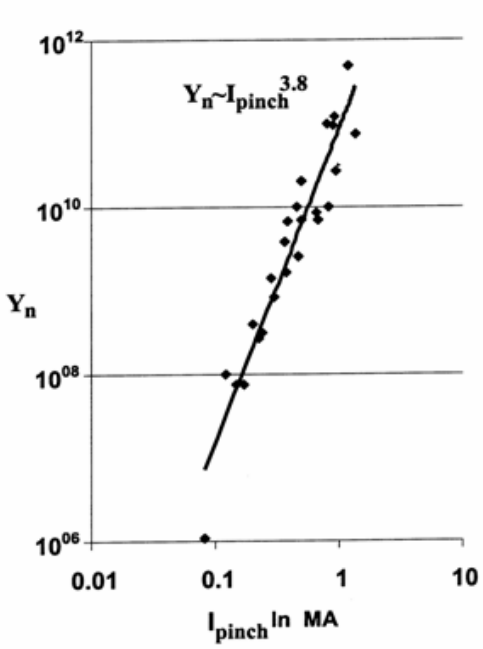

Figure 4. Assembly of experimental data to obtain Y_n scaling with current; loosely termed as the current or pinch current in the literature. This is the experimental curve from which a calibration point is obtained, at 0.5 MA, to calibrate the neutron yield equation (3) for the Lee Model code.

We then apply the calibrated code to several machines including the PF400, UNU/ICTP PFF, the NX2 and Poseidon to derive neutron scaling laws from computation. The PF1000 which has a current curve published at 27kV and Y_n published at 35kV provided an important point. Moreover using parameters for the PF1000 established at 27 kV and 35 kV, additional points were taken at different voltages ranging from 13.5kV upwards to 40kV. These machines were chosen because each has a published current trace and hence the current curve computed by the model code could be fitted to the measured current trace.

Table 2. Computed values of I_{peak}, I_{pinch} & Y_n and selected parameters for a range of Focus Machines

Machine	V_o (kV)	P_o (Torr)	L_o (nH)	C_o (μF)	b (cm)	a (cm)	Z_o (cm)	I_{peak} (MA)	I_{pinch} (MA)	S	Y_n	k_{min}	I_{pinch}/I_{peak}
PF400	**28**	**6.6**	**40**	**0.95**	**1.55**	**0.60**	**1.7**	**0.126**	**0.082**	**82**	**1.1×10^{06}**	**0.14**	**0.65**
UNU	**15**	**4**	**110**	**30**	**3.2**	**0.95**	**16**	**0.182**	**0.123**	**96**	**1.2×10^{07}**	**0.14**	**0.68**
NX2 T	**15**	**5**	**20**	**28**	**5**	**2**	**7**	**0.386**	**0.225**	**86**	**2.5×10^{08}**	**0.16**	**0.58**
Calibration	**16**	**5**	**24**	**308**	**7**	**4**	**30**	**0.889**	**0.496**	**99**	**5.6×10^{09}**	**0.17**	**0.56**
NX2 T-2	**12.5**	**10.6**	**19**	**28**	**3.8**	**1.55**	**4**	**0.357**	**0.211**	**71**	**2.4×10^{08}**	**0.16**	**0.59**
PF1000	**13.5**	**3.5**	**33**	**1332**	**8.00**	**5.78**	**60**	**0.924**	**0.507**	**89**	**9.6×10^{09}**	**0.17**	**0.55**
	18	**3.5**	**33**	**1332**	**10.67**	**7.70**	**60**	**1.231**	**0.636**	**89**	**2.9×10^{10}**	**0.18**	**0.52**
	23	**3.5**	**33**	**1332**	**13.63**	**9.84**	**60**	**1.574**	**0.766**	**89**	**6.8×10^{10}**	**0.19**	**0.49**
	27	**3.5**	**33**	**1332**	**16**	**11.60**	**60**	**1.847**	**0.862**	**89**	**1.2×10^{11}**	**0.19**	**0.47**
	30	**3.5**	**33**	**1332**	**17.77**	**12.80**	**60**	**2.049**	**0.929**	**89**	**1.6×10^{11}**	**0.20**	**0.45**
	35	**3.5**	**33**	**1332**	**20.74**	**15.00**	**60**	**2.399**	**1.037**	**89**	**2.7×10^{11}**	**0.20**	**0.43**
	40	**3.5**	**33**	**1332**	**23.70**	**17.10**	**60**	**2.736**	**1.137**	**89**	**4.1×10^{11}**	**0.21**	**0.42**
Poseidon	**60**	**3.8**	**18**	**156**	**9.50**	**6.55**	**30**	**3.200**	**1.260**	**251**	**3.3×10^{11}**	**0.20**	**0.39**

In Table 2, corresponding to each laboratory device, the operating voltage V_o and pressure P_o are typical of the device, as is the capacitance C_o. It was found that the static inductance L_o usually needed to be adjusted from the value provided by the laboratory. This is because the value provided could be for short-circuit conditions, or an estimate including the input flanges and hence that value may not be sufficiently close to L_o. The dimensions b (outer radius), a (anode radius) and z_o (anode length) are also the typical dimensions for the specific device. The speed factor S [17] is also included. All devices except Poseidon have typical S values. Poseidon is the exceptional high speed device in this respect. The minimum pinch radius is also tabulated as $k_{min}= r_p/a$. It is noted that this parameter increases from 0.14 for the smaller machines towards 0.2 for the biggest machines. The ratio I_{pinch}/I_{peak} is also tabulated showing a trend of decreasing from 0.65 for small machines to 0.4 for the biggest machines.

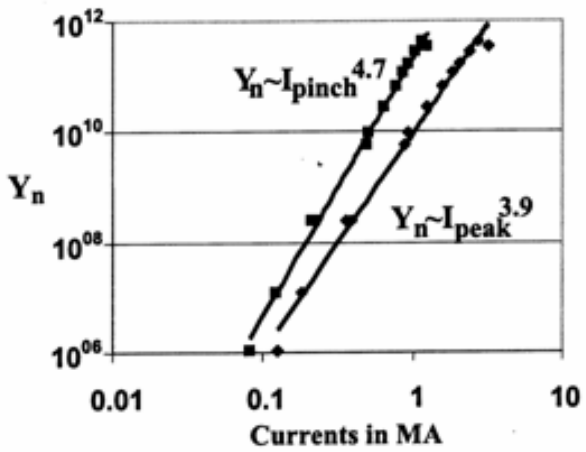

Figure 5. Computed neutron yield compiled to produce Y_n~I_{peak} and Y_n~I_{pinch} scaling laws

The results are the following: $Y_n=2x10^{11}I_{pinch}^{4.7}$ and $Y_n=9x10^{9}I_{peak}^{3.9}$; Y_n in units of neutrons per shot; and I_{peak} and I_{pinch} in MA.

It is felt that the scaling law with respect to I_{pinch} is rigorously obtained by these numerical experiments when compared with that obtained from measured data, which suffers from inadequacies in the measurements or assumptions of I_{pinch}.

6. Measurement of pinch current

The total current trace in a plasma focus discharge is the most commonly measured quantity. However, yield laws for plasma focus should be scaled to focus pinch current I_{pinch} rather than peak total current I_{peak}. Since the direct measurement of I_{pinch} is laborious and difficult, a reliable method for its deduction would be useful. Numerical experiments using the Lee Model code can be used to determine I_{pinch} from the total current trace of a plasma focus by fitting a computed current trace to the measured current trace. The method is applied to an experiment in which both the total current trace and the plasma sheath current trace were measured. The result shows good agreement between the values of computed and measured I_{pinch}.

We now describe how we tested the validity of this method. In an experiment in Stuttgart [28,29] using the DPF78, a Rogowski coil measured the I_{total} trace, and magnetic probes measured the plasma current I_p waveform. The bank parameters were C_0=15.6 μF (nominal) and L_0=45 nH (nominal), tube parameters were b=50 mm, a=25 mm, and z_0=150 mm, and operating parameters were V_0=60 kV, and P_0=7.6 Torr Deuterium. Figure 6 shows these measured I_{total} (labeled as I_{ges}) and I_p waveforms. The third trace is the difference of I_{total} and I_p.

These parameters were put into the code. The best fit for the computed I_{total} with the measured I_{total} waveform was obtained with the following: bank parameters were C_0 =17.2 μF, L_0=55 nH, and r_0=3.5 mΩ; tube parameters were b=50 mm, a=25 mm, and z_0=137 mm; and operating parameters were V_0=60 kV and P_0=7.6 Torr deuterium. Model parameters of f_m=0.06, f_c=0.57, f_{mr}=0.08, and f_{cr} =0.51 were fitted. With these parameters, the computed I_{total} trace compared well with the measured I_{total} trace, as shown in Figure

7. The computed dynamics, currents, and other properties of this plasma focus discharge were deemed to be correctly simulated.

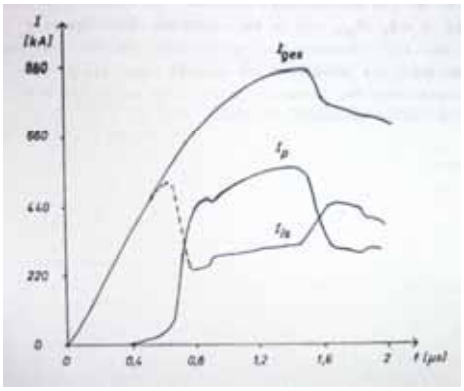

Figure 6. Experimental measurements of I_{total} (top trace) & I_{plasma} on DPF78 in Stuttgart.

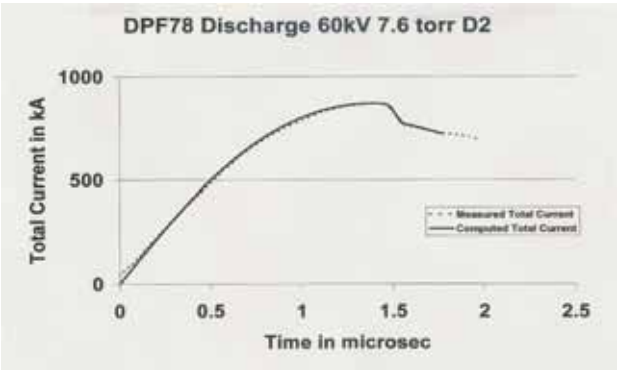

Figure 7. Fitting the computed I_{total} waveform to the measured I_{total} waveform from Fig 6

From the numerical experiments I_{pinch} was computed as 397 kA. I_{pinch} measured in the Stuttgart DPF78 experiment (Figure 6) was=381 kA. The computed I_{pinch} was 4% larger than the measured I_{pinch}. This difference was to be expected considering that the modeled f_{cr} was an average value of 0.51; while the laboratory measurement showed (Figure 8) that in the radial phase I_p/I_{total} varied from 0.63 to 0.4, and at the start of the pinch phase this ratio was 0.49 and rapidly dropping. Thus, one would expect the computed value of I_{pinch} to be somewhat higher than the measured, which turned out to be the case. Nevertheless, the difference of 4% is better than the typical error of 20% estimated for I_{pinch} measurements using magnetic probes. The numerical method proves to be a good alternative, being more accurate and convenient and only needing a commonly measured I_{total} waveform.

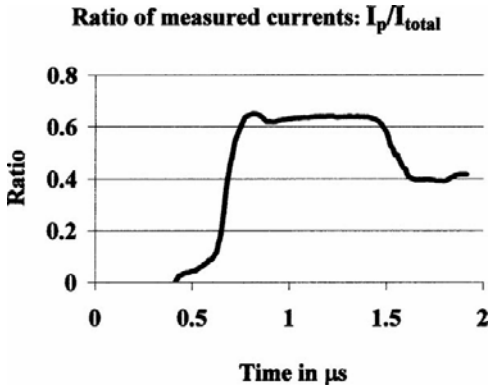

Figure 8. Ratio (measured) I_p/I_{total} derived from Figure 6.

7. Conclusion

The results of these numerical experiments indicate that corresponding to each plasma focus of capacitance C_0, there is an optimum value for L_0 below which performance in terms of I_{pinch} and Y_n does not improve. A scaling law $Y_n \sim I_{pinch}^{4.7}$ is obtained from the numerical experiments. This numerically computed scaling is more rigorous and reliable than previously obtained scaling of Y_n with loosely termed 'pinch current'. This is because we have clearly defined and rigorously computed our pinch currents. It is worth emphasizing that one of the most important ideas arising from this series of published papers is the crucial need to differentiate between the commonly-measured I_{total} and the almost-never-measured pinch current I_{pinch} in attempts to understand plasma focus processes and scaling. The Lee Model code is a reliable tool to determine the pinch current.

References

[1] Lee S 1984 Radiations in Plasmas ed B McNamara (Singapore: World Scientific) pp 978–87
[2] Lee S et al 1988 Am. J. Phys. **56** 62
[3] Tou T Y, Lee S and Kwek K H 1989 IEEE Trans. Plasma Sci. **17** 311
[4] Lee S 1991 IEEE Trans. Plasma Sci. **19** 912
[5] Potter D E 1971 Phys. Fluids **14** 1911
[6] Liu M H, Feng X P, Springham S V and Lee S 1998 IEEE Trans. Plasma Sci. **26** 135–40
[7] Lee S, Lee P, Zhang G, Feng X, Gribkov V A, Liu M, Serban A and Wong T 1998 IEEE Trans. Plasma Sci. **26** 1119
[8] Bing S 2000 Plasma dynamics and x-ray emission of the plasma focus PhD Thesis NIE ICTP Open Access Archive: http://eprints.ictp.it/99/
[9] Lee S 2000/2007 http://ckplee.myplace.nie.edu.sg/plasmaphysics/
[10] Lee S 2005 ICTP Open Access Archive: http://eprints.ictp.it/85/
[11] Siahpoush V, Tafreshi M A, Sobhanian S and Khorram S 2005 Plasma Phys. Control. Fusion **47** 1065
[12] Lee S 1998 Twelve Years of UNU/ICTP PFF—A Review IC, 98 (231) Abdus Salam ICTP, Miramare, Trieste; ICTP OAA: http://eprints.ictp.it/31/
[13] L. Soto, P. Silva, J. Moreno, G. Silvester, M. Zambra, C. Pavez, L. Altamirano, H. Bruzzone, M. Barbaglia, Y. Sidelnikov & W. Kies. Brazilian J Phys 34, 1814 (2004)
[14] H.Acuna, F.Castillo, J.Herrera & A.Postal. International conf on Plasma Sci, 3-5 June 1996, conf record Pg127
[15] C.Moreno, V.Raspa, L.Sigaut & R.Vieytes, Applied Phys Letters 89(2006)
[16] D.Wong, P.Lee, T.Zhang, A.Patran, T.L.Tan, R.S.Rawat & S.Lee. Plasma Sources, Sci & Tech 16, 116 (2007)
[17] S Lee & A Serban, IEEE Trans Plasma Sci **24**, 1101-1105 (1996)
[18] Gribkov V A *et al* 2007 *J. Phys. D: Appl. Phys.* **40** 3592
[19] Lee S Radiative Dense Plasma Focus Computation Package: RADPF http://www.intimal.edu.my/school/fas/UFLF/
[20] Lee S and Saw S H 2008 Appl. Phys. Lett. **92** 021503
[21] S Lee, P Lee, S H Saw and R S Rawat. Plasma Phys. Control. Fusion **50** (2008) 065012
[22] Lee S and Saw S H Neutron scaling laws from numerical experiments J. Fusion Energy at press
[23] Lee S, Saw S H, Lee P C K, Rawat R S and Schmidt H 2008 Appl. Phys. Lett. **92** 111501
[24] J.D.Huba. 2006 Plasma Formulary pg44 http://wwwppd.nrl.navy.mil/nrlformulary/NRL_FORMULARY_07.pdf
[25] S.V.Springham, S.Lee & M.S.Rafique. Plasma Phys Control.Fusion 42, 1023 (2000)
[26]W Kies in *Laser and Plasma Technology*, Procs of Second Tropical College Ed by S Lee, B.C. Tan, C.S. Wong, A.C. Chew, K.S. Low, H. Ahmad & Y.H. Chen , World Scientific, Singapore ISBN 9971-50-767-6 (1988) p86-137
[27] H Herold in *Laser and Plasma Technology*, Procs of Third Tropical College Ed by C S Wong, S. Lee, B.C. Tan, A.C. Chew, K.S. Low & S.P. Moo, World Scientific, Singapore ISBN 981-02-0168-0 (1990) p21-45
[28] T. Oppenländer: Ph.D. Dissertation, University of Stuttgart, Germany, 1981
[29] G Decker, L Flemming, H J Kaeppeler, T Oppenlander, G Pross, P Schilling, H Schmidt, M Shakhatre and M Trunk, Plasma Physics **22**, 245-260 (1980)

Click here to see list of awardees of IPFS-IBC1

Results of the Internet-based Workshop on Plasma Focus Numerical Experiments

S Lee
Institute for Plasma Focus Studies, 32 Oakpark Drive, Chadstone, VIC 3148, Australia
NTI International University College, 71800 Nilai, Malaysia
Nanyang Technology University, National Institute of Education, Singapore 637616

e-mail: leesing@optusnet.com.au

Abstract

The Institute of Plasma Focus Studies was founded with the aim of using the Lee model code to assist training of focus scientists in the same way that the UNU ICTP PFF was used successfully to train a generation of plasma focus researchers. The inaugural activity of the IPFS was an internet-based Workshop on Plasma Focus Numerical Experiments. Over 4 weeks, 30 participants were guided to configure the RADPFV5.13.9b to operate a range of machines from the tiny PF400 to the 1 MJ PF1000. Important exercises included fitting a plasma focus so that the computed current waveform agrees, in axial and radial features, with the measured waveform, thus obtaining the model parameters of that particular machine. Computed properties were tabulated side-by-side for a small and a big machine to show **similar** properties and **scalable** properties. The evolution of current profiles with pressure was traced for a neutron yielding focus as well as for a neon soft x-ray yielding focus. 18 participants from 9 countries successfully submitted all exercises. A surprising development is also reported. This concerns an additional exercise given to participants to be attempted in future. Numerical experiments in connection with this exercise show that contrary to what Nukulin and Polukhin surmised, there is neither current nor neutron saturation attributable to purely electrodynamic effects for plasma focus machines up to 25 MJ. The numerical experiments show that early peaking of the current profile for megajoule banks invalidates the crux of the N & P argument. The numerical experiments also find the conditions at which a 3 MJ plasma focus may yield 10^{13} D-D neutrons, a landmark target for materials testing in connection with first wall materials in fusion reactors.

1. Introduction

The Institute for Plasma Focus Studies was founded to promote the understanding of plasma focus devices. The method used will be communication through the internet. The main instrument will be the plasma focus simulation package based on the Lee model, the latest being the version RADPFV5.13.9b.

From the mid-Eighties to mid-Nineties and on to the new Millennium a group assisted in the starting and strengthening of several laboratories on plasma focus studies [1] , using a 3 kJ plasma focus the UNU/ICTP PFF, specially designed for that purpose. More than 20 Fellows were trained to build, use and maintain this plasma focus through intensive hands-on training programmes sponsored by UNU, ICTP, UNESCO and TWAS and the AAAPT. This plasma focus, though low-cost, has proved very useful in the

education of plasma focus scientists [2]. It is now actively operated in 7 countries and research on it has produced more than 22 PhD theses, 50 Masters theses and 200 peer reviewed research papers.

From the very beginning of that program it was realized that the laboratory work should be complemented by computer simulation. A 2-phase model was developed in 1984 [3,4]. Over the years we have developed the model until its present form [5-7]. It now includes thermodynamics data so the code can be operated in H_2, D_2, He, Ne, Ar, Xe. We have used it to simulate a wide range of plasma focus devices from the sub-kJ PF400 (Chile) through the small 3kJ UNU/ICTP PFF (Network countries), the NX2 3kJ Hi Rep lithographic focus (Singapore), medium size tens of kJ DPF78 & Poseidon (Germany) to the MJ PF1000 [7]. An Iranian Group has modified the model, calling it the Lee model, to simulate Filippov type plasma focus [8].

We are now confident that the Lee model in its latest coded version the RADPFV5.13.9b; can realistically simulate all Mather type plasma focus, from small to large, and produce reliable results for all the electrodynamic processes including axial and radial trajectories, total discharge currents and plasma currents, energy distributions; and also giving a good representation of the temperature waveform, radiation yields and neutron yields [7].

Although we can simulate any given machine, without any experimental input, our standard practice requires a measured total discharge current versus time waveform from the specific machine together of course with the bank parameters (capacitance, static inductance), tube parameters (cathode/anode radii, anode length) and operating parameters (voltage, pressure and which gas). We then configure the code with these parameters; and further use 4 model parameters (a mass swept-up factor and a plasma current factor for each of axial and radial phases) to fit the computed total discharge current trace to the experimental total discharge current trace. The process, carried out separately for axial and radial phases, usually ends with an excellent fit for both shape and absolute magnitudes of the total current waveform [9-12].

The total discharge current, particularly the fraction of it flowing in the plasma, drives all the electrodynamic processes in the axial and radial phases; even the plasma heating and radiation are coupled into the equation of motion during the pinch phase.

Conversely all these processes are reflected back in the profile of the plasma current and hence the total discharge current. **The total discharge current carries in its profile and magnitudes the information about all the processes that go on in the plasma focus**. Thus having fitted the computed I_{total} trace with the measured I_{total} trace, we then have the confidence that all the processes are realistically simulated; and the numerical results are realistic representation of the actual properties of that particular plasma focus.

In the last 3 months of 2007 numerical experiments using the code found a new effect, the plasma focus pinch current limitation effect [11,12]. We also re-formulated neutron yield scaling laws from the numerical experiments [9] and defined a numerical procedure [10] to compute pinch current I_{pinch} from the waveform of the easily measured total discharge current $I_{total.}$. This code is a universal numerical laboratory that will complement any plasma focus laboratory; acting as a powerful research tool that goes beyond the normal experimental reach. The power of this tool is only limited by the researcher's limit in imagination.

As an inaugural exercise of the IPFS the Internet-based Workshop on Plasma Focus Numerical Experiments was held from 14 April to 19 May 2008.

2. The Program

The program was divided into 4 parts.

The **first part** introduced the worksheet, guiding the participant to configure the code as a Numerical Plasma Focus Laboratory (UPFL) to operate as any plasma focus. The input data to configure each focus are: the bank parameters static inductance L_0, capacitance C_0 and circuit resistance r_0; the tube parameters outer radius b, inner radius a and tube length z_0 and operational parameters voltage V_0 and pressure P_0 and the fill gas. The model parameters representing the mass swept-up factor f_m, the plasma current factor f_c for the axial phase and factors f_{mr} and f_{cr} for the radial phases are also required. As an example the participant operated the NX2 [13,14], studied the results {see Fig 1) and completed an exercise with some measurements taken from the results displayed by the worksheet after a shot. Notes were supplied to emphasize the importance of the inductive and resistive effects of plasma focus dynamics on the current time profile; the fact that all energetic processes are reflected in the current waveform.

Fig 1. The worksheet configured for NX2 Neon, showing the results of a shot.

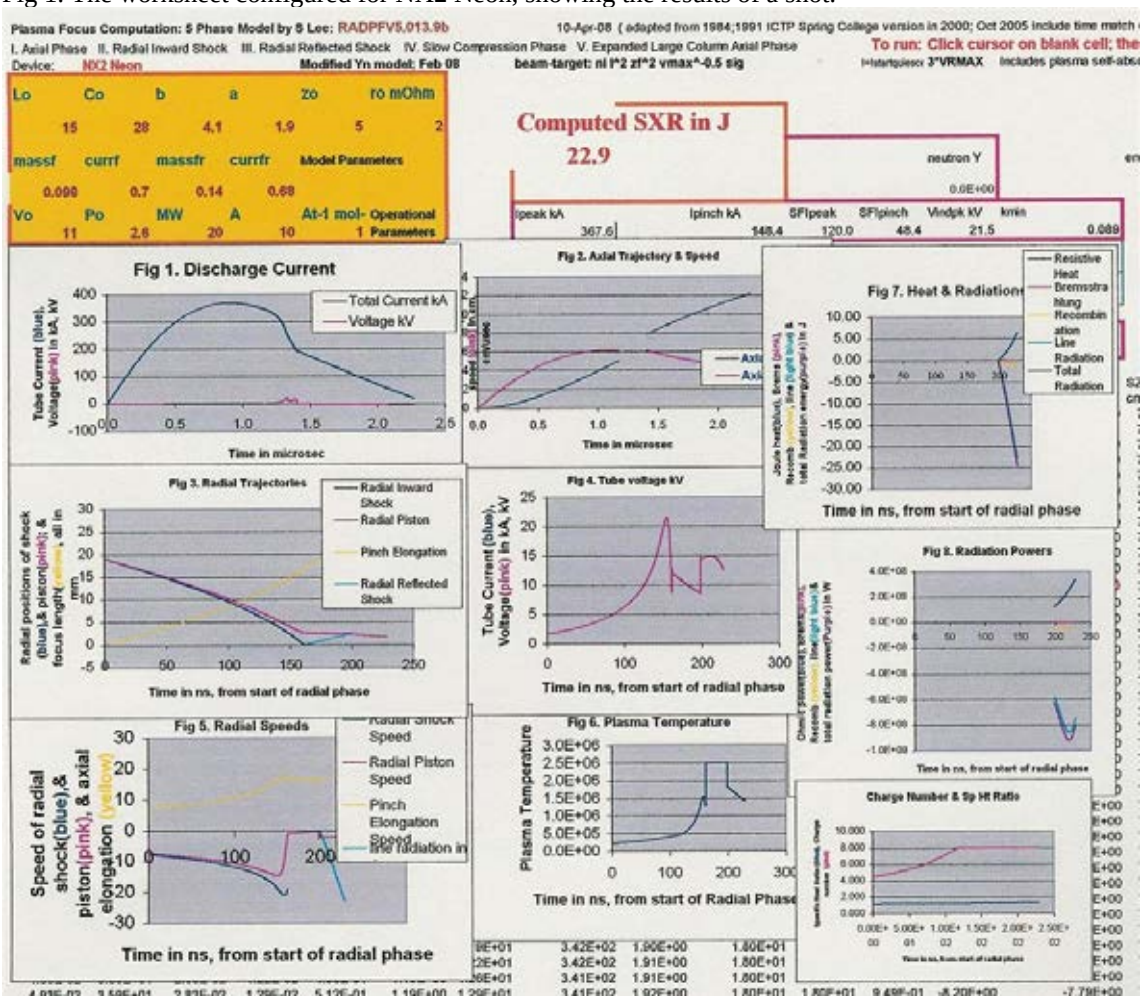

What about the model parameters? In the **second part** of the program, a participant was guided to configure the code as the biggest plasma focus in the world the 1 MJ PF1000 using guessed trial model parameters, fire the focus, and adjust the trial model parameters progressively until the computed current waveform agreed with a published current waveform of the PF1000 [15].

The axial phase is fitted first, followed by the radial phase (see Fig.2a-c). As an exercise, a participant was then required to fit the PF400 [16], with storage energy several thousand times smaller than the PF1000. A side-by-side tabulation of the results for the BIG and small machines show **similar** properties, such as speeds, temperature (energy density), ratios of "peak pinch dimension/inner radius", and **scalable** properties such as pinch dimensions and times and neutron yield (Fig 3). The physics of the similarity and scaling was discussed [5-7,17]. The importance of clearly distinguishing pinch current I_{pinch} from peak total current I_{peak} was emphasized [9-12].

Fig 2a. Computed current trace not agreeing with measured trace; need to adjust f_m, f_c.

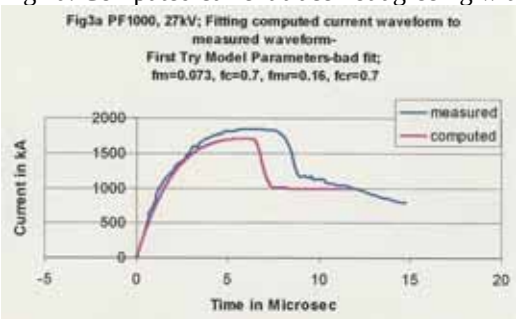

Fig 2b. Computed trace agrees with measured trace, up to end of axial phase.

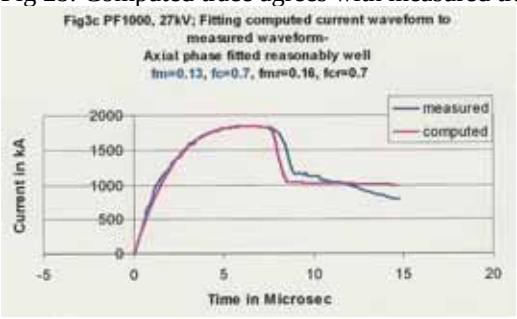

Fig 2c. Computed trace agrees with measured trace; reasonable fit to end of pinch phase.

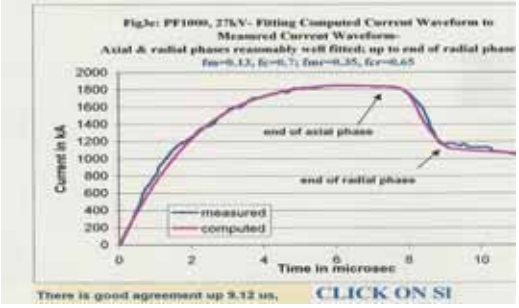

Fig 3. Comparing properties of a BIG & a small focus, showing **Similar** properties & **Scalable** Properties.

Parameter	**PF1000** (**27kV** 3.5 Torr D2)	Ratio **PF1000/PF400**	**PF400** (**28kV** 6.6 Torr D2)	Ratio **PF1000/DPF78**	DPF78 (**60kV** 7.6Torr D2)
Stored Energy Eo in kJ	486	1313	0.37	15.6	31
Pressure in Torr, Po	3.5	0.53	6.6	0.47	7.5
Anode radius a in cm	11.55	19.3	0.6	4.6	2.5
c=b/a	1.39	0.54	2.6	0.7	2
anode length z_o in cm	60	35	1.7	4.4	13.7
final pinch radius r_{min} in cm	2.3	26.7	0.086	6.2	0.37
pinch length z_{max} in cm	18.9	22.2	0.85	5.5	3.43
pinch duration in ns	282	53	5.3	16.7	16.9
r_{min}/a	0.2	1.4	0.143	1.36	0.147
z_{max}/a	1.64	1.16	1.42	1.2	1.37
I_{peak} in kA	1845	14.6	126	2.1	869
I_{peak}/a in kA/cm	160	0.76	210	0.4	348
$S=(I_{peak}/a)/(P_o^{1/2})$(kA/cm)/Torr$^{1/2}$	**85.6**	1.05	**81.7**	0.59	**127**
I_{pinch} in kA	784	9.64	81.3	1.96	401
I_{pinch}/I_{peak}	0.425	0.65	0.65	0.92	0.46
Peak induced voltage in kV	40.1	2.4	16.7	0.43	93
peak axial speed in cm/us	11.2	1.24	9	0.72	15.5
peak radial shock speed cm/us	16.4	0.48	34.3	0.36	45.2
peak radial piston speed cm/us	10.9	0.48	22.9	0.36	30.2
peak temperature in 10^6K	1.14	0.19*	6.1	0.11*	10.4
neutron yield Y_n in 10^6	8.6E+04	82000	1.05	6.6	1.3E+03
Measured Y_n in 10^6: range	(2 - 7)E+04		0.9-1.2		
Measured Y_n in 10^6 :highest	2.0E+05				9.0E+03

Note: ratios in **orange**: values are of the order of 1; ratios in **blue**: values are of the order of (ratio of anode radii) or (ratio of Ipeak); ratio of temperature (**orange***) is a special case, because of the difference in values of c.
[These points are worth thinking about; with reference to the file on the Theory of the Lee model, available from http://www.intimal.edu.my/school/fas/UFLF/
Look especially at the sections on the scaling parameters of the axial and radial phases]

Part 3 went on to guide a participant to more advanced fitting situations; e.g. how to fit the stray circuit resistance r_0 (commonly not given by experimenters), or values of L_0 and C_0 in cases (commonly encountered) where nominal (or inaccurate values) are given. Even given values of z_0 may need to be fitted as 'effective values' as well as a time shift given to the whole measured current trace to account for break-down times and switching processes. An exercise was given to a participant to fit the DPF78 [10], which required some of these more advanced fitting considerations.

Part 4 took the participant back to work on the PF1000; operating the PF1000 from short-circuit-like high pressure, through to optimum pressure for neutron yield, and then down to lower pressures (Fig 4). In the process the neutron yield was plotted as a function of pressure. Various other properties were also plotted for the participant to get a feel of any correlations (see Fig 5). For example as the pressure was increased, I_{peak} was seen to increase continually with pressure whereas I_{pinch} reached a maximum value at a pressure close to the optimum pressure for neutron yield. This emphasized again the importance to distinguish clearly I_{peak} and I_{pinch} in the analysis of plasma focus performance.

Fig 4. Showing evolution of current trace with pressure; the greater and greater distortion of the current traces (from sinusoid) is due to greater dynamic resistance with greater speeds as pressure is reduced.

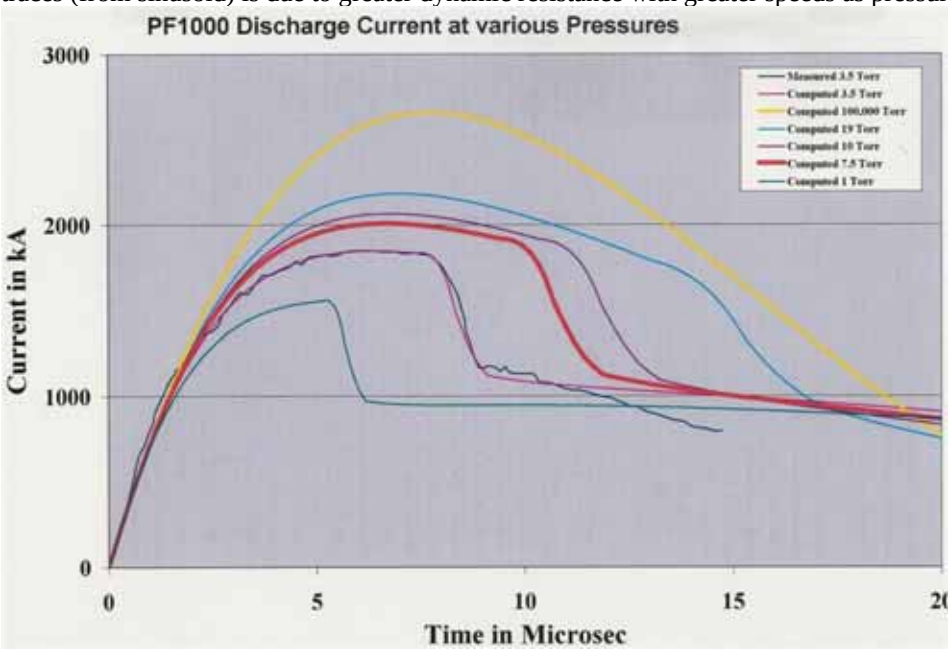

The second section of Part 4 had the participant working on the NX2 neon soft x-ray production as a function of pressure (Fig 6), again plotting the yield and various focus pinch properties against pressure (Fig 7) to enhance the understanding of correlation. Moreover the soft x-ray yield versus pressure curve was found to agree with experimental measurements.

Fig 5. Variation of Yn, speeds, pinch dimensions & other properties with pressure.

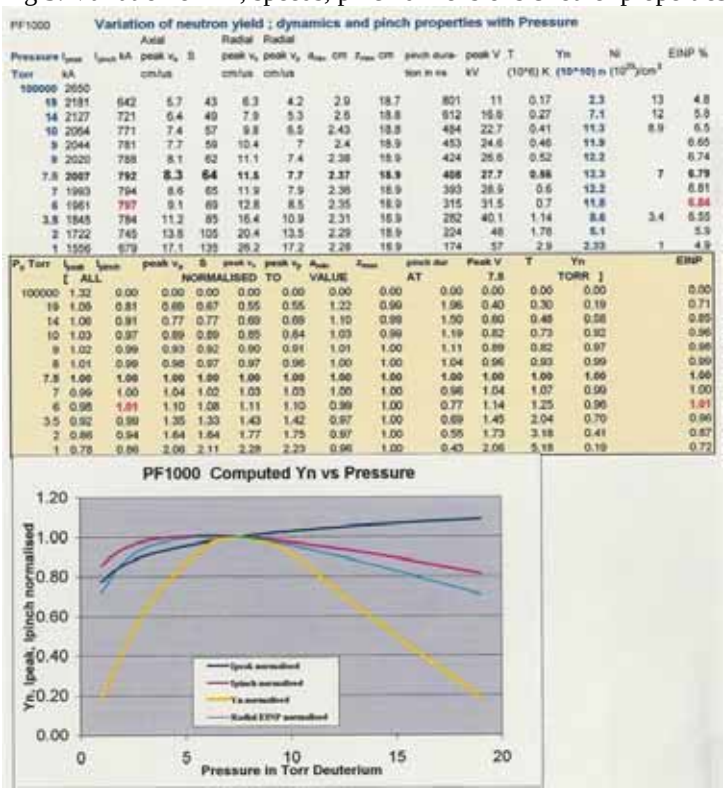

PF1000 Variation of neutron yield ; dynamics and pinch properties with Pressure

Pressure Torr	I_{peak} kA	I_{pinch} kA	Axial peak v_a cm/us	S	Radial peak v_s cm/us	Radial peak v_p cm/us	R_{min} cm	Z_{max} cm	pinch duration in ns	peak V kV	T (10^6) K	Yn (10^9) n	Ni (10^18)/cm^2	EINP %
100000	2650													
19	2181	642	5.7	43	6.3	4.2	2.9	18.7	801	11	0.17	2.3	13	4.8
14	2127	721	6.4	49	7.9	5.3	2.6	18.8	612	16.9	0.27	7.1	12	5.9
10	2064	771	7.4	57	9.8	6.5	2.43	18.8	484	22.7	0.41	11.3	8.9	6.5
9	2044	781	7.7	59	10.4	7	2.4	18.9	453	24.6	0.46	11.9		6.65
8	2020	788	8.1	62	11.1	7.4	2.38	18.9	424	26.6	0.52	12.2		6.74
7.8	2007	792	8.3	64	11.5	7.7	2.37	18.9	408	27.7	0.55	12.3	7	6.79
7	1993	794	8.6	65	11.9	7.9	2.36	18.9	393	28.9	0.6	12.2		6.81
6	1961	797	9.1	69	12.8	8.5	2.35	18.9	315	31.5	0.7	11.8		6.84
3.5	1845	784	11.2	85	16.4	10.9	2.31	18.9	282	40.1	1.14	8.6	3.4	6.55
2	1722	745	13.8	105	20.4	13.5	2.29	18.9	224	48	1.76	6.1		5.9
1	1556	679	17.1	135	26.2	17.2	2.28	18.9	174	57	2.9	3.33	1	4.9

P_0 Torr	I_{peak} [ALL	I_{pinch} NORMALISED	peak v_a TO	S VALUE	peak v_s	peak v_p	R_{min}	Z_{max}	pinch dur AT	Peak V 7.8	T	Yn TORR]	EINP
100000	1.32	0.00	0.00	0.00	0.00	0.00	0.00	0.00	0.00	0.00	0.00	0.00	0.00
19	1.05	0.81	0.69	0.67	0.55	0.55	1.22	0.99	1.96	0.40	0.30	0.19	0.71
14	1.06	0.91	0.77	0.77	0.69	0.69	1.10	0.99	1.50	0.60	0.48	0.58	0.85
10	1.03	0.97	0.89	0.89	0.85	0.84	1.03	0.99	1.19	0.82	0.73	0.92	0.96
9	1.02	0.99	0.93	0.92	0.90	0.91	1.01	1.00	1.11	0.89	0.82	0.97	0.98
8	1.01	0.99	0.98	0.97	0.97	0.96	1.00	1.00	1.04	0.96	0.93	0.99	0.99
7.8	1.00	1.00	1.00	1.00	1.00	1.00	1.00	1.00	1.00	1.00	1.00	1.00	1.00
7	0.99	1.00	1.04	1.02	1.03	1.03	1.00	1.00	0.96	1.04	1.07	0.99	1.00
6	0.98	1.01	1.10	1.08	1.11	1.10	0.99	1.00	0.77	1.14	1.25	0.96	1.01
3.5	0.92	0.99	1.35	1.33	1.43	1.42	0.97	1.00	0.69	1.45	2.04	0.70	0.96
2	0.86	0.94	1.64	1.64	1.77	1.75	0.97	1.00	0.55	1.73	3.18	0.41	0.87
1	0.78	0.86	2.06	2.11	2.28	2.23	0.96	1.00	0.43	2.06	5.18	0.19	0.72

Fig 6. Evolution of discharge current in NX2 as a function of pressure.

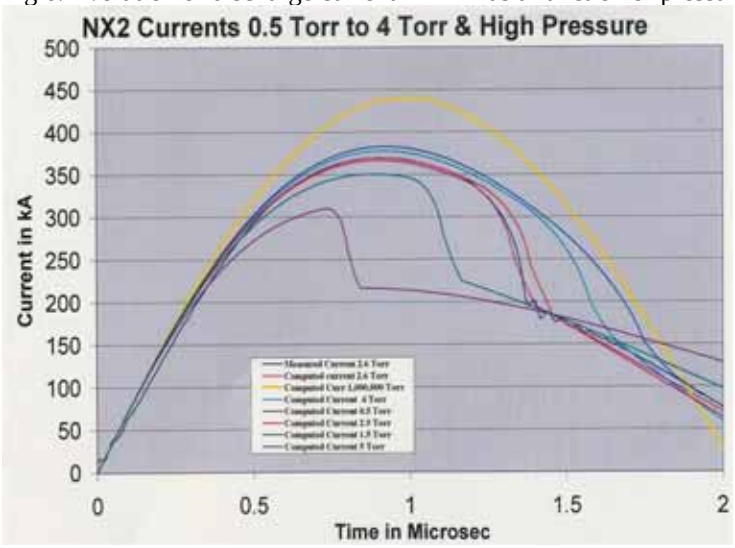

Fig 7. Variation of Y_{sxr}, speeds and pinch properties with pressure of NX2, Hi Rep Focus developed for microelectronics lithographic & micromachining purposes. The attached graph also shows comparison of computed yield curve vs measured yield points.

NX2: 11kV, Neon. Variation of Soft X-Ray Yield and Dynamics and Pinch Properties with Operating Pressure

Comparison of computed yield vs measured yield

Po Torr	I_{peak} kA	I_{pinch} kA	peak v_a cm/us	S	peak v_s cm/us	peak v_p cm/us	a_{min} cm	z_{max} cm	pnch dur ns	V_{max} kV	T_{pinch} (10^6)K	N_i pinch $(10^{25})/m^3$	z		EINP %	Ysxr J	ALT	
1E+06	440																	
10	unable to force										middle	of	pinch					
5	383	76	4.6	90	11.1	8.6	0.86	2.84	100	7	0.3	1.1	5.5	6.3	0	0.61	pinch expanding	
4.5	381	99	4.8	94	12.2	9.5	0.42	2.7	60	10	0.47	2.4	7.7	8.6	0	0.64	pinch expanding	
4	378	114	5	99	14.9	11.6	0.29	2.7	46	13.7	0.7	3.2	8	10.7	0.0003	0.68	pinch not compressive	
3.5	374	128	5.3	105	17	12.8	0.22	2.75	37	16.4	1.03	3.9	8	12.9	4.5	0.73		
3.2	372	135	5.6	109	18.8	13.7	0.19	2.79	34	18.4	1.23	4.1	8	14.4	14.6	0.76		
3	370	140	5.7	113	20	14.1	0.18	2.8	32	19.8	1.4	4.1	8	15.2	19.9	0.79		
2.9	**369**	**142**	**5.8**	**114**	**20.6**	**14.5**	**0.17**	**2.79**	**30.6**	**20**	**1.51**	**4**	**8**	**15.5**	**20.8**	**0.8**		
2.8	369	144	5.9	116	21.1	14.8	0.17	2.79	29.6	20.1	1.61	3.8	8	15.7	20	0.82		
2.7	368	146	6	118	21.8	15	0.18	2.78	28.8	21.2	1.72	3.5	8	15.8	17.9	0.83		
2.6	367	148	6.1	120	22.5	15.3	0.19	2.75	27.3	21.5	1.86	3	8	15.8	14.4	0.85		
2.4	364	152	6.3	124	24.4	15.4	0.22	2.7	23.5	22.3	2.18	2.3	8	15.6	8	0.88		
2	359	159	6.8	134	25.2	16.7	0.25	2.73	23.6	23.7	2.8	1.6	8.2	16.2	3.9	0.97		
1.5	350	164	7.6	151	27.6	18.8	0.26	2.77	22.4	26.7	3.9	1.1	8.7	16.7	1.5	1.12		
1	338	165	8.8	178	32	22.7	0.26	2.77	19.3	31.2	5.5	0.7	9.3	16.5	0.4	1.4		
0.5	310	157	11.1	230	41	28.6	0.26	2.78	15.5	37	9.4	0.35	10	14.4	0.05	1.93		

Po Torr	Ipeak [	Ipinch Normalised	Peak va	S	Peak vs to	Peak vp the	amin	zmax value	pnch dur	Vmax at	T pinch optimum	ni pinch	z	2.9	EINP Torr	Ysxr]	J	ALT
1E+06	1.19																	
10																		
5	1.04	0.54	0.7931	0.79	0.5388	0.5931	5	1.02	3.268	0.34	0.1987	0.275	0.7		0.41	0.00000	0.76	
4.5	1.03	0.7	0.8276	0.82	0.5922	0.6552	2.44	0.97	1.961	0.49	0.3113	0.6	1		0.55	0.00000	0.8	
4	1.02	0.8	0.8621	0.87	0.7233	0.8	1.69	0.97	1.503	0.67	0.4636	0.8	1		0.69	0.00001	0.85	
3.5	1.01	0.9	0.9138	0.92	0.8252	0.8828	1.28	0.99	1.209	0.81	0.6821	0.975	1		0.83	0.21635	0.91	
3.2	1.01	0.95	0.9655	0.96	0.9126	0.9448	1.1	1	1.111	0.91	0.8146	1.025	1		0.93	0.70192	0.95	
3	1	0.99	0.9828	0.99	0.9709	0.9724	1.02	1	1.046	0.98	0.9272	1.025	1		0.98	0.95673	0.99	
2.9	1	1	1	1	1	1	1	1	1.000	1	1	1	1		1	1.00000	1	
2.8	1	1.01	1.0172	1.02	1.0243	1.0207	1.01	1	0.967	0.99	1.0662	0.95	1		1.01	0.96154	1.03	
2.7	0.99	1.03	1.0345	1.04	1.0583	1.0345	1.05	1	0.941	1.04	1.1391	0.875	1		1.02	0.86058	1.04	
2.6	0.99	1.04	1.0517	1.05	1.0922	1.0552	1.1	0.99	0.893	1.06	1.2318	0.75	1		1.03	0.69231	1.06	
2.4	0.99	1.07	1.0862	1.09	1.													
2	0.97	1.12	1.1724	1.18	1.													
1.5	0.95	1.15	1.3103	1.32	1.													
1	0.91	1.16	1.5172	1.56	1.													
0.5	0.84	1.11	1.9138	2.02	1.													

Experimental data: Zhang Guixin
Plasma Soft X-ray Source for Microelectronics Lithography
PhD NTU/NIE 1999 pg 206 Fig6.77b
NX2-same configuration 11.5 kV
Published in IEEE Trans Plasma Sci **26 (1998) 1119**

Po Neon Torr	Ysxr J	Ysxr normalised to Optimum
1	2	0.11
1.5	9	0.47
2	8	0.42
2.5	13	0.68
2.8	15.9	0.84
3	16.1	0.85
3.5	19	1
4	11.5	0.61
4.6	9	0.47
5	2	0.11

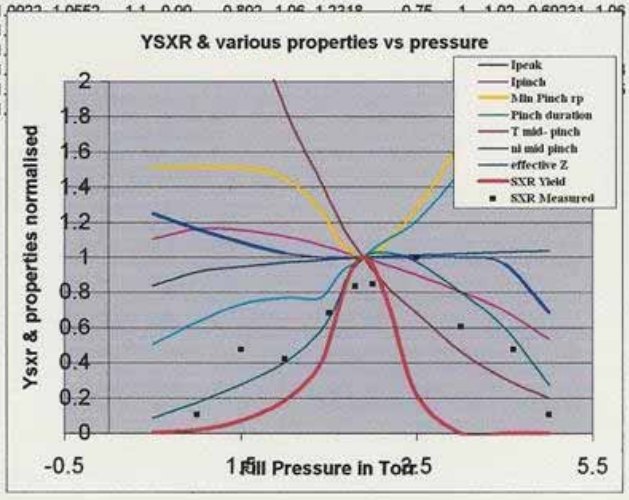

3. Participation

Eighteen participants submitted all exercises. There was a lively exchange of views, in the discussion of the physics of the plasma focus. Regarding the fitting of the model parameters in some cases, particularly for the PF1000, there appeared to be some difference of opinion as to what constituted the best fit. There emerged the consensus that one is not able to get a perfect fit; in the sense that you can defend it as absolutely the perfect fit. The way to treat it is that one has got a working fit; something to work with; which gives comparable results with experiments; rather than perfect agreement. There is no such thing anyway; experiments on any one plasma focus under consistent conditions give a range of results; especially in yields (factor of 2-5 range is common). Thus several slightly differing working fits should still all give results that fall within the range of the hardware experiment.

Even though a fit may only be a 'working' fit (as opposed to the hypothetical perfect fit) when one runs a series of well planned numerical experiments one can then see a trend e.g. how properties, including yields, change with pressure or how yields scale with I_{pinch}, or with L_0 etc. And if carefully carried out, the numerical experiments can provide, much more easily, results just like hardware experiments; with the advantage that after proper reference to existing experiments, then very quickly one can extend to future experiments and predict probable results.

4. Additional exercises

In order to engage the participant beyond the workshop to emphasize that the UPLF is to be used as a tool in later work two additional experiments were proposed. The first involved a simple exercise to run the code for PF400 neutron yield [16] as a function of pressure and to compare the computed results with published results of the PF400. The second outlined the broad idea of using the code to verify (or not) the Nukulin and Polukhin (N & P) idea that for megajoule plasma focus machines current and neutron yield saturate from a consideration of purely electrodynamic effects [18].

5. Results arising out of the additional exercises

In order to be able to answer prospective queries from participants in future, numerical experiments were then carried out. For the PF400, the numerical experiments resulted in a paper to be presented in this Workshop. Although a simple exercise, the results establish the state of the art, since before this effort, all plasma focus neutron computation only compared with the measured values in order of magnitude.

Numerical experiments carried out to verify the N & P idea for the second additional exercise very quickly showed that the crux of their argument is wrong; in fact based on purely electrodynamic consideration, there is no saturation for I_{peak}, I_{pinch} or Y_n. A detailed study followed, which revealed that their error was related to assumptions of current profile. Numerical experiments show that there is a very early peaking (Fig 8) of the current profile for megajoule devices, whereas the N & P scenario envisaged a much longer current risetime of the order of $(L_aC_0)^{0.5}$ where the inductance of the coaxial tube L_a is further assumed in the N & P scenario to be proportional to C_0.

Fig. 8. Comparing the N & P scenario waveform and the computed waveform.

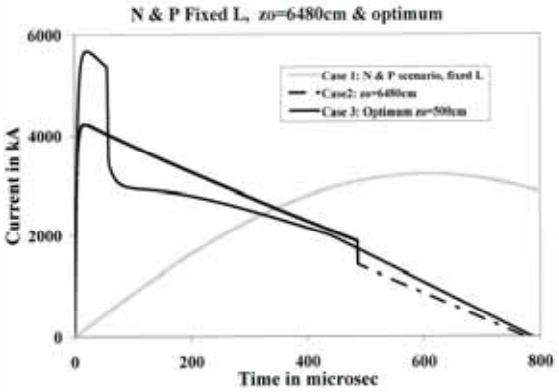

Fig 9. Computed currents showing no saturation, as opposed to the N & P scenario.

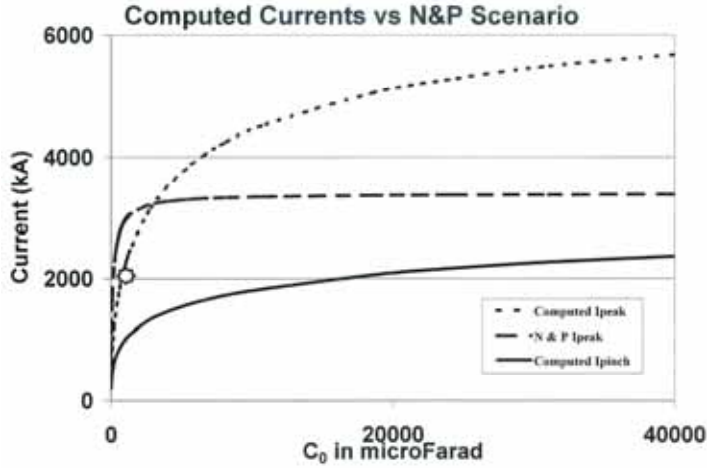

The numerical studies gave the following important results [19]:

$Y_n \sim E_0^{2}$ for low (kJ) energies; this scaling slows down to $Y_n \sim E_0^{0.84}$ for megajoule energies up to the 25 MJ levels investigated.

The scaling of Y_n with I_{peak} and I_{pinch} shows similar slowing down at high megajoules.

As a result, over the whole range of energies from kJ up to the 25 MJ level investigated, it was found that the scaling of Y_n with currents are as follows:

$Y_n \sim I_{peak}^{3.8}$ and
$Y_n \sim I_{pinch}^{4.5}$

This is the first time that neutron scaling with I_{peak} or I_{pinch} up to such high energies has been formulated. The currents involved go up to 6.7 MA for I_{peak} and 2.7 MA for I_{pinch}.

Furthermore, numerical experiments found the conditions to reach the landmark target of 10^{13} D-D neutrons per shot (convertible to 10^{15} D-T neutron), for cost-effective testing of materials for first wall

components in magnetic & inertial confinement fusion reactors [20] as follows:

PF1000-like banks at 35 kV:	18 MJ
Modern, low-damped banks:	8 MJ
High voltage (90 kV) banks:	3 MJ at I_{pinch} of 2.5 MA

6. Conclusion

A report of the Internet-based Workshop on Plasma Focus Numerical Experiments is given. The Lee model code is used as a Universal Plasma Focus Laboratory Facility, configured to operate as a range of plasma focus from very small to very big for neutron yield and soft x-ray yield. Major points emphasized in the activity include model fitting, similar and scalable properties of the plasma focus, evolution of current waveforms, neutron and soft x-ray yields, and focus properties with pressure, and the importance of distinguishing between I_{pinch} and I_{peak} for scaling purposes. Arising from additional exercises, important results pertaining to current and neutron scaling of megajoule plasma focus machines were obtained, and prepared for publication [19].

References

[1] Sing Lee & Chiow San Wong. Physics Today. **May 2005** 31-36
[2] Lee S 1998 Twelve Years of UNU/ICTP PFF—A Review IC, 98 (231) Abdus Salam ICTP, Miramare, Trieste; ICTP OAA: http://eprints.ictp.it/31/
[3] Lee S 1984 Radiations in Plasmas ed B McNamara (Singapore: World Scientific) pp 978–87 1S.
[4] Lee S in *Laser and Plasma Technology*, edited by S. Lee, B. C. Tan, C. S. Wong, and A. C. Chew. World Scientific, Singapore, 1985_, pp. 387–420.
[5] Lee S 2000/2007 http://ckplee.myplace.nie.edu.sg/plasmaphysics/
[6] Lee S 2005 ICTP Open Access Archive: http://eprints.ictp.it/85/
[7] Lee S Radiative Dense Plasma Focus Computation Package: RADPF http://www.intimal.edu.my/school/fas/UFLF/
[8] Siahpoush V, Tafreshi M A, Sobhanian S and Khorram S 2005 Plasma Phys. Control. Fusion **47** 1065
[9] Lee S and Saw S H Neutron scaling laws from numerical experiments J. Fusion Energy at press
[10] Lee S, Saw S H, Lee P C K, Rawat R S and Schmidt H 2008 Appl. Phys. Lett. **92** 111501
[11] S Lee, P Lee, S H Saw and R S Rawat. Plasma Phys. Control. Fusion **50** (2008) 065012
[12] Lee S and Saw S H 2008 Appl. Phys. Lett. **92** 021503
[13] Lee S, Lee P, Zhang G, Feng X, Gribkov V A, Liu M, Serban A and Wong T 1998 IEEE Trans. Plasma Sci. **26** 1119
[14] Bing S 2000 Plasma dynamics and x-ray emission of the plasma focus PhD Thesis NIE ICTP Open Access Archive: http://eprints.ictp.it/99/
[15] Gribkov V A *et al* 2007 *J. Phys. D: Appl. Phys.* **40** 3592
[16] Patricio Silva, Jose Moreno, Leopoldo Soto, Lipo Birstein, Roberto E. Mayer and Walter Kies 2003. Appl. Phys. Lett. **83**, 3269
[17] Lee S and Serban A 1996 IEEE Trans. Plasma Sci. **24** 1101–5
[18] Nukulin V Ya and Polukhin S N 2007 *Plasma Phys. Rep.* **33** 271–7
[19] S Lee. Current and Neutron Scaling for Megajoule Plasma Focus Machines, submitted to Plasma Phys & Controlled Fusion, June 2008
[20] Gribkov V A *et al* 2007 *J. Phys. D: Appl. Phys.* **40** 1977

Numerical Experiments on PF400 Neutron Yield

S Lee[1,2,3], S H Saw[2,4]
[1]Institute for Plasma Focus Studies, 32 Oakpark Drive, Chadstone, VIC 3148, Australia
[2]INTI International University College, 71800 Nilai, Malaysia
[3]Nanyang Technology University, National Institute of Education, Singapore 637616
[4]Universty of Malaya, Kuala Lumpur, Malaysia

e-mail: leesing@optusnet.com.au

Abstract

Numerical experiments are carried out, using the Lee model code to compute the neutron yield of PF400 as a function of pressure. Results are compared with published laboratory measurements, showing agreement between the numerical and the laboratory experiments.

1. Introduction

The Lee Model couples the electrical circuit with plasma focus dynamics, thermodynamics and radiation, enabling realistic simulation of all gross focus properties. The basic model, described in 1984 [1], was successfully used to assist several experiments [2-5]. An improved 5-phase model and code incorporating small disturbance speed [6], and radiation coupling with dynamics assisted other research projects [7-9], and was web-published in 2000 [10] and 2005 [11]. Plasma self-absorption was included in 2007 [10] improving soft x-ray yield simulation. The code has been used extensively in several machines including UNU/ICTP PFF [2,5,7,8,12], NX2 [8,9], NX1 [8], and adapted for the Filippov-type plasma focus DENA [13]. A recent development is the inclusion of neutron yield, Y_n, using a beam–target mechanism [2], incorporated in the present version [14] of the code RADPFV5.13.b, resulting in realistic Y_n scaling with I_{pinch} [15]. The versatility and utility of the Lee Model is demonstrated in its clear distinction of I_{pinch} from I_{peak} [16] and the recent uncovering of a plasma focus pinch current limitation effect [17,18]. The description, theory, code and a broad range of results of this 'Universal Plasma Focus Laboratory Facility' is available for download from [19].

2. Procedures for the numerical experiments

The Lee Model code is configured to work as any plasma focus by inputting the bank parameters, L_0, C_0 and stray circuit resistance r_0; the tube parameters b, a and z_0 and operational parameters V_0 and P_0 and the fill gas. The standard practice is to fit the computed total current waveform to an experimentally measured total current waveform [11,15-19] using four model parameters representing the mass swept-up factor f_m, the plasma current factor f_c for the axial phase and factors f_{mr} and f_{cr} for the radial phases.
From experience it is known that the current trace of the focus is one of the best indicators of gross performance. The axial and radial phase dynamics and the crucial energy transfer into the focus pinch are among the important information that is quickly apparent from the current trace.

The exact time profile of the total current trace is governed by the bank parameters, by the focus tube geometry and the operational parameters. It also depends on the fraction of mass swept-up and the fraction of sheath current and the variation of these fractions through the axial and radial phases. These parameters determine the axial and radial dynamics, specifically the axial and radial speeds which in turn affect the profile and magnitudes of the discharge current. The detailed profile of the discharge current during the pinch phase also reflects the Joule heating and radiative yields. At the end of the pinch phase the total current profile also reflects the sudden transition of the current flow from a constricted pinch to a large column flow. Thus the discharge current powers all dynamic, electrodynamic, thermodynamic and radiation processes in the various phases of the plasma focus. Conversely all the dynamic, electrodynamic, thermodynamic and radiation processes in the various phases of the plasma focus affect the discharge current. It is then no exaggeration to say that the discharge current waveform contains information on all

the dynamic, electrodynamic, thermodynamic and radiation processes that occurs in the various phases of the plasma focus. This explains the importance attached to matching the computed current trace to the measured current trace in the procedure adopted by the Lee Model code.

3. The numerical experiments- fitting the computed current trace to obtain the model parameters

Silva, Moreno and Soto et al had published a paper [20] with laboratory measurements from the PF400, including a typical current waveform and a graph on neutron yield vs pressure. We first fit the computed current waveform to the published measured waveform in the following manner.

We then configure the Lee model code (version RADPF05.13.9b) to operate as the PF400 starting with the following published [20] bank and tube parameters:

Bank parameters:	L_0=38nH, C_0=0.88μF, r_0=not given
Tube parameters:	b=1.55 cm, a=0.6 cm, z_0=2.8 cm
Operating parameters:	V_0=28 kV, P_0= 6.6 Torr Deuterium

where L_0=static inductance (nominal) , C_0= storage capacitance (nominal), b=tube outer radius, a=inner radius, z_0=tube axial length, V_0=operating voltage, P_0= operating initial pressure.

To obtain a reasonably good fit the following bank and tube parameters (L_0, C_0 and z_0 refitted and r_0 fitted) are used:

Bank parameters:	L_0=40 nH, C_0=0.95 μF, r_0=10 mΩ
Tube parameters:	b=1.55 cm, a=0.6 cm, z_0=1.7 cm
Operating parameters:	V_0=28 kV, P_0= 6.6 Torr Deuterium

together with the following fitted model parameters:

f_m=0.08, f_c=0.7, f_{mr}=0.11 and f_{cr}=0.7.

The fitted computed current waveform is compared with published waveform in Fig.1.

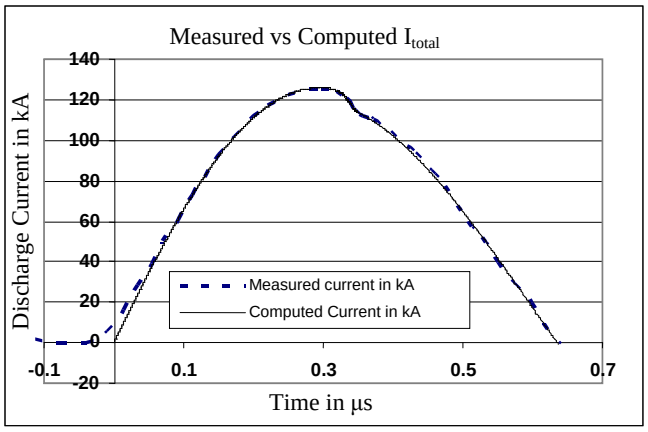

Fig 1. Computed discharge current compared to published current for PF400.

4. The numerical Experiments- computing the neutron yield as a function of operating pressure

Using the fitted model parameters, numerical experiments are then carried out at various initial pressures in Deuterium. The neutron yields Y_n are then tabulated in Table 1 and compared with the published values [20] in Fig. 2.

Table 1: Computed Y_n compared with published Y_n for PF400 as a function of pressure

	Measured	Computed
P_0 (mbar)	Y_n (10^6)	Y_n (10^6)
1		0.25
2		0.55
3		0.81
4		0.99
5		1.11
6	0.2	1.16
7	0.53	1.15
8	0.7	1.10
9	1.06	1.01
10	0.78	0.90
11	0.74	0.77
12	0.2	0.63
13		0.50
14		0.38
15		0.27

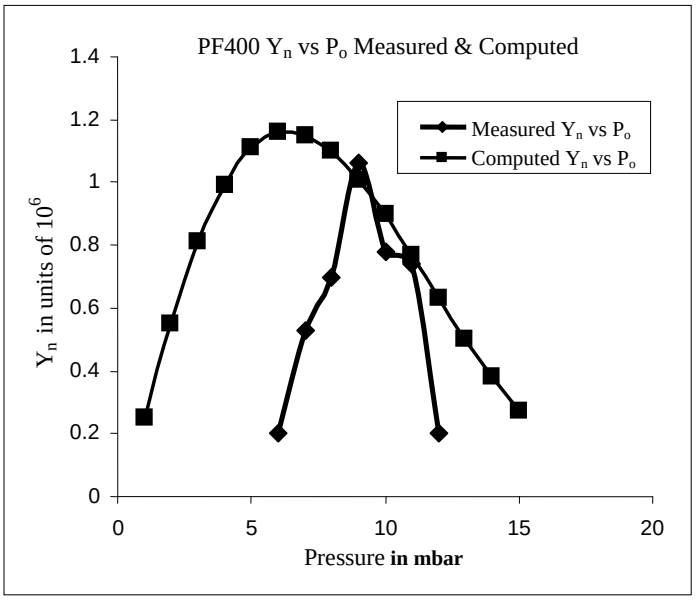

Fig. 2. Computed and Measured Neutron Yield as functions of pressure.

Figure 2 shows that the computed neutron yield versus pressure curve agrees reasonably with the published curve. The agreement is even more remarkable when we note that the same model code (version RADPF05.13.9b) also shows reasonable agreement in neutron yield when compared with the published results of the PF1000 [15]; noting that the PF400 is a small plasma focus of 400 J whilst the PF1000 is one of the biggest plasma focus in the world at 1 MJ. Despite all the discussions in the literature about neutron production mechanisms such as beam-target [14], gyrating ions, moving boiler and others, the state of the art is not able to do better than make order of magnitude estimates [21]. Figure 2 is the first time, to our knowledge, that computed neutron yield versus pressure data has been quantitatively compared with measured data; moreover with several important features of agreement.

5. Conclusion

The Lee Model code is used to compute the neutron yield versus pressure curve of the Chilean PF400. The computed results agree reasonably well with the published curve.

References

[1] Lee S 1984 Radiations in Plasmas ed B McNamara (Singapore: World Scientific) pp 978–87
[2] Lee S et al 1988 Am. J. Phys. **56** 62
[3] Tou T Y, Lee S and Kwek K H 1989 IEEE Trans. Plasma Sci. **17** 311
[4] Lee S 1991 IEEE Trans. Plasma Sci. **19** 912
[5] Lee S and Serban A 1996 IEEE Trans. Plasma Sci. **24** 1101–5
[6] Potter D E 1971 Phys. Fluids **14** 1911
[7] Liu M H, Feng X P, Springham S V and Lee S 1998 IEEE Trans. Plasma Sci. **26** 135–40
[8] Lee S, Lee P, Zhang G, Feng X, Gribkov V A, Liu M, Serban A and Wong T 1998 IEEE Trans. Plasma Sci. **26** 1119
[9] Bing S 2000 Plasma dynamics and x-ray emission of the plasma focus PhD Thesis NIE ICTP Open Access Archive: http://eprints.ictp.it/99/
[10] Lee S 2000/2007 http://ckplee.myplace.nie.edu.sg/plasmaphysics/
[11] Lee S 2005 ICTP Open Access Archive: http://eprints.ictp.it/85/
[12] Lee S 1998 Twelve Years of UNU/ICTP PFF—A Review IC, 98 (231) Abdus Salam ICTP, Miramare, Trieste; ICTP OAA: http://eprints.ictp.it/31/
[13] Siahpoush V, Tafreshi M A, Sobhanian S and Khorram S 2005 Plasma Phys. Control. Fusion **47** 1065
[14] Gribkov V A *et al* 2007 *J. Phys. D: Appl. Phys.* **40** 3592
[15] Lee S and Saw S H Neutron scaling laws from numerical experiments J. Fusion Energy at press
[16] Lee S, Saw S H, Lee P C K, Rawat R S and Schmidt H 2008 Appl. Phys. Lett. **92** 111501
[17] S Lee, P Lee, S H Saw and R S Rawat. Plasma Phys. Control. Fusion **50** (2008) 065012
[18] Lee S and Saw S H 2008 Appl. Phys. Lett. **92** 021503
[19] Lee S Radiative Dense Plasma Focus Computation Package: RADPF
http://www.intimal.edu.my/school/fas/UFLF/
[20] Patricio Silva, Jose Moreno, Leopoldo Soto, Lipo Birstein, Roberto E. Mayer
and Walter Kies 2003. Appl. Phys. Lett. **83**, 3269
[21] S P Moo, private communication, July 2008.

Compact sub-kilojoule range fast miniature plasma focus as portable neutron source

2008 Plasma Sources Sci. Technol. 17 045020

(http://iopscience.iop.org/0963-0252/17/4/045020)

Plasma Sources Sci. Technol. **17** (2008) 045020 (11pp) doi:10.1088/0963-0252/17/4/045020

Compact sub-kilojoule range fast miniature plasma focus as portable neutron source

Rishi Verma[1,2], M V Roshan[1], F Malik[1], P Lee[1], S Lee[1], S V Springham[1], T L Tan[1], M Krishnan[3] and R S Rawat[1,4]

[1] Natural Sciences and Science Education, National Institute of Education, Nanyang Technological University, Singapore 637616, Singapore
[2] Pulsed Power Group, Institute for Plasma Research, Bhat, Gandhinagar, Gujarat 382428, India
[3] Alameda Applied Sciences Corporation, CA 94577, USA

E-mail: rajdeep.rawat@nie.edu.sg

Received 26 March 2008, in final form 12 July 2008
Published 1 September 2008
Online at stacks.iop.org/PSST/17/045020

Abstract
As a first step toward the development of a compact and portable, quasi-continuous pulsed neutron source, we have demonstrated a 'fast miniature plasma focus (PF) device' as a compact nuclear fusion apparatus. The system operates with deuterium gas and produces an average neutron yield (Y_{90°) of $(1 \pm 0.27) \times 10^4$ neutrons/shot at ~70 kA peak discharge current. In the range of 1.5–4 mbar, a distinct and sharp dip in the current derivative signal indicates a strong pinching action with subsequent emission of hard x-rays followed by a neutron pulse. The yield and the time history of the neutrons were measured by both active and passive detection techniques (such as a ^{3}He proportional counter, NE102A plastic scintillator and CR-39 SSNTDs). The overall dimensions of the apparatus, which includes a capacitor bank, sparkgap switch and the focus chamber, are 0.2 m × 0.2 m × 0.5 m and the total mass of the system is ~25 kg. The scope of this paper is to evaluate/demonstrate the potential of such a fast miniature PF device as a compact and portable fusion apparatus producing neutrons while operating at relatively low energy.

(Some figures in this article are in colour only in the electronic version)

1. Introduction

The plasma focus (PF) is a kind of pinch discharge in which a pulsed high voltage is applied to a low pressure gas between coaxial cylindrical electrodes generating short duration (~10–50 ns) high density plasma (~10^{19} cm^{-3}). The PF device was independently discovered by Mather [1] and Filippov [2] in the late 1950s. Since then many advances have been made by various laboratories across the world to harness the potential of PF as a source of fusion neutrons when operated with deuterium.

The coaxial discharge arrangement in a PF device uses a fast-rising current pulse with the inner electrode as anode and the outer electrode as cathode. The plasma discharge is initiated along a dielectric insulator at the closed, upstream end of the electrode assembly and generates a $\vec{J} \times \vec{B}$ Lorentz force that drives the plasma sheath toward the open end of the coaxial electrode assembly. Once the plasma sheath has traversed the length of the anode, magnetic forces rapidly further accelerate the plasma radially inward across the face of the anode, resulting in the formation of a pinched plasma column with very high temperatures and densities [3]. In the pinch, temperature is of the order of ~200 eV–1 keV. The pinch phase is designed to coincide with the natural rise time of the capacitor bank, in order to achieve the best pinching efficiency. The typical velocity of the current sheath is of the order of 5–10 cm μs^{-1} and 15–25 cm μs^{-1} in the axial rundown and radial compression phases, respectively. The PF device generates beams of ions and electrons, ultra-short bursts of soft and hard x-rays (HXRs) and neutrons (if operated with deuterium) during and after the radial compression phase.

Using deuterium as the filling gas, as a consequence of D–D fusion reactions, fast neutrons of energy ~2.5 MeV and

[4] Author to whom any correspondence should be addressed.

energetic protons of energy ∼3 MeV (leaving behind ^{3}He and ^{3}H) are produced. The neutron burst typically lasts about tens to hundreds of nanoseconds [4]. The major advantage of the PF as a pulsed neutron source over a passive radioactive source of fast neutrons of similar energy is that passive sources such as ^{252}Cf with similar mean energy or Am–Be with a harder spectrum emit continuously, causing inconvenience in handling and storing [5], whereas the PF, being a pulsed plasma device, does not have any activation problem for storage and handling.

Over the past few decades, most of the experimental studies on PF devices were in medium (2–10 kJ) [6–9], large 10–500 kJ [10–13] and mega-joule [14, 15] PF facilities and not many results have been reported on the sub-kilojoule range, low energy PF devices. In fact, the PF community was somewhat skeptical about reproducibility and efficient pinching in the sub-kilojoule range of PF devices. The inherent advantage with the sub-kilojoule range 'miniature PF' devices is that they are much smaller in size and cost effective in comparison with medium and high energy plasma foci and also easier to operate in a repetitive regime from a few Hz to kHz range since the driving power requirement is low. For these reasons the development of sub-kilojoule range miniature PF devices is now gaining momentum [16–21], but it is still in the stage of infancy and more research is required to develop an efficient and reproducible miniature PF device which would find commercial applications.

In this paper, we present the results of optimization of a miniature PF utilizing different electrode designs and dimensions to generate strong pinches and neutron yield.

2. Experimental arrangement

As a first step toward the development of a repetitive pulsed neutrons source, a low energy PF device named 'Fast Miniature PF (FMPF-1)' (200 J, 2.4 μF, 27 nH, $T/4 \sim 400$ ns) was designed and constructed. A computational code developed by Lee [22] was used to optimize the FMPF-1's parameters to maximize the 2.45 MeV D–D neutron yield. One of the major considerations in the design was to obtain a PF device of minimum possible dimensions and mass for enhanced portability. Specifications of the capacitor bank were chosen such that for field applications FMPF-1 could be charged using battery powered high voltage supplies [23]. In order to make the system efficient, significant efforts were made to reduce the driver inductance. The capacitor bank consisted of four 0.6 μF, 30 kV low inductance capacitors (total mass ∼20 kg), connected in parallel, in a compact layout through a common transmission plate assembly of size 0.2 m × 0.2 m as shown in figure 1.

Four layers of 125 μm thick Mylar were used as insulation between the transmission plates. The connections between capacitor bank, spark gap and PF head were integrated without use of cables to minimize the total system inductance. This was done by embedding the indigenously designed spark gap within the transmission line assembly of the capacitor bank and by directly interfacing the PF head to the discharge end of the spark gap (figure 2).

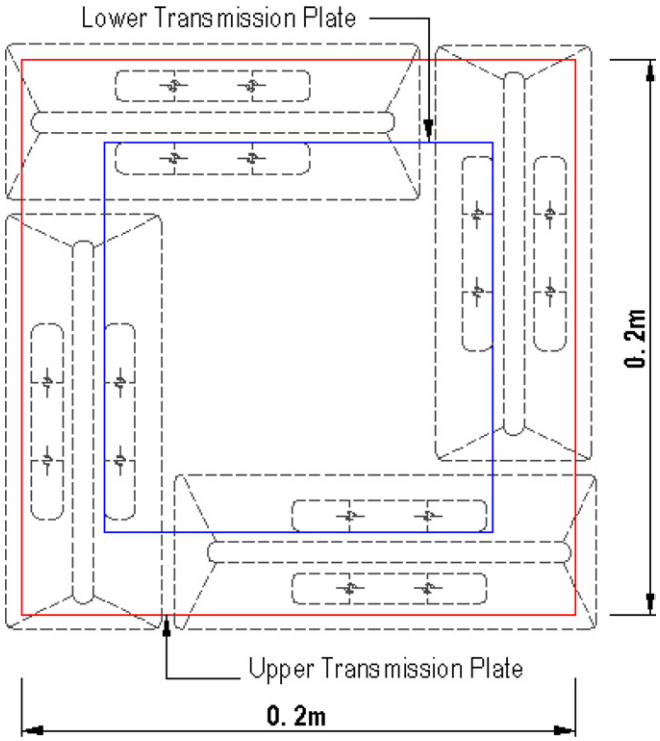

Figure 1. Layout of the compact geometry of 200 J capacitor bank.

The measured total driver bank inductance (≈capacitor bank inductance + transmission line inductance + spark gap inductance) was about 27 ± 2 nH. The control system and radiation diagnostics of the PF were contained in a Faraday cage in order to minimize pick-up due to the associated intense electromagnetic noise generated during PF operation.

The finalized coaxial electrode assembly of the PF head consisted of a 17 mm long stainless steel (SS) anode of composite geometry [24] and a chamber wall of 30 mm inner diameter acting as cathode. The chamber was fabricated from stainless steel material and had a wall thickness of 5 mm. Traditionally, PF devices have been characterized as Mather and Filippov types according to their anode aspect ratios, i.e. $A = l/2a$ in which l is the effective anode length and a the radius of the anode. The Mather configuration is defined with an aspect ratio >1 (typically 5–10) whereas the Filippov configuration has an aspect ratio <1 (typically 0.2–0.5). The miniature PF device reported here is closer to the Mather type, but its aspect ratio is only 2.8.

An insulator sleeve of Pyrex glass with a breakdown length of 5 mm was placed between the SS anode and cathode. Selection of the anode and insulator sleeve material was done in accordance with comparative studies reported earlier for the enhanced neutron yield. Significant improvement in the neutron yield was reported by Shyam *et al* [25] using an anode with low discharge driven erosion. A comparative study performed by Zakaullah *et al* [26] regarding anode material indicated two-fold enhancements in the neutron yield when an SS anode was used in comparison with a copper anode. Pyrex was chosen as the insulator sleeve material because Beg *et al* [27] indicated a higher neutron yield with a higher

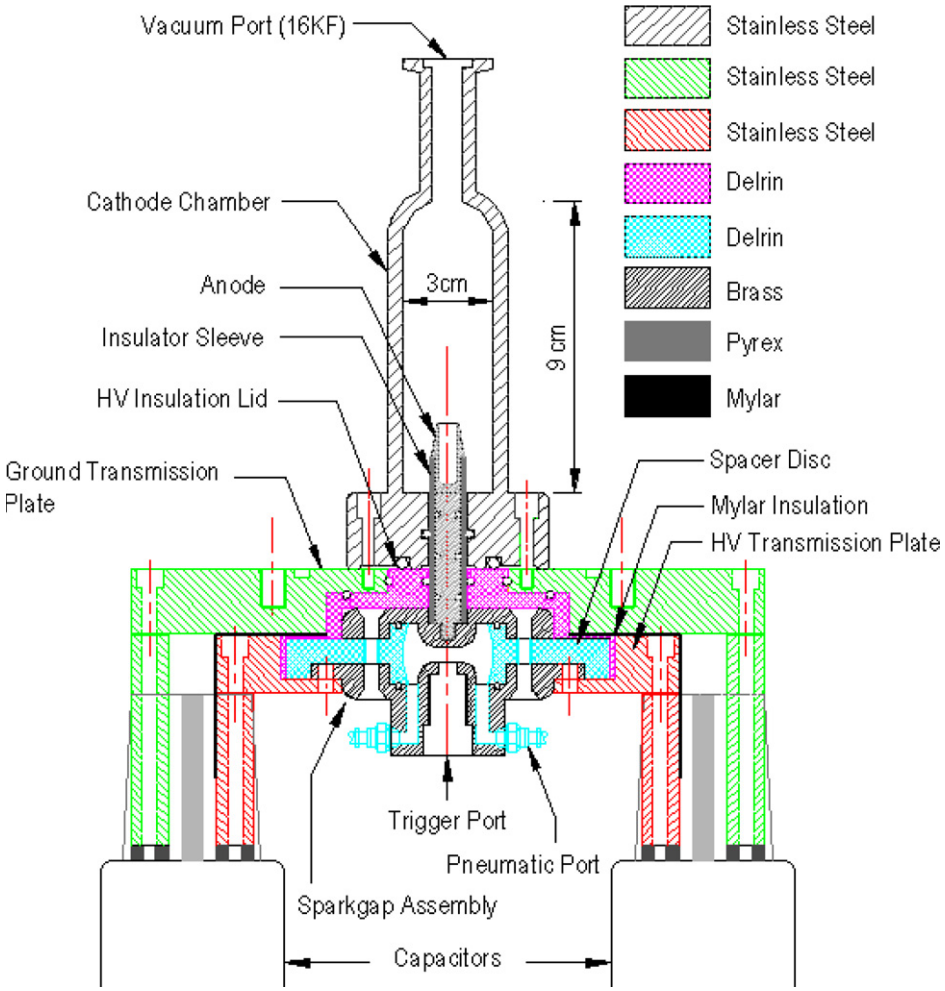

Figure 2. Construction details of the FMPF-1 device.

dielectric constant insulator sleeve and Pyrex has a fairly high dielectric constant of 4.5–6 and is relatively inexpensive.

3. Diagnostics arrangement

Diagnostics of FMPF-1 have been found to be more complicated in comparison with conventional kilojoule range PF devices for the following reasons: (i) in medium and high energy range PF devices, the quarter rise time ($T/4$) of electrical discharges is typically in the range of a few microseconds (1–5 μs), but in the sub-kilojoule range of miniature PF devices it is faster, typically ranging from 150 to 500 ns. Therefore the associated plasma dynamics is much faster in comparison with conventional kilojoule devices. In such fast discharges, the bandwidth of the electrical diagnostics must be wider to observe fast dynamic events such as the pinch phase which may have a typical lifetime of only a few nanoseconds. (ii) Another complication that is associated with the operation of 'fast miniature PF device' is the generation of large electromagnetic noise, from the Mylar separated low inductance parallel plate assembly due to transmission line effects and secondarily from the sparkgaps [28]. In the present device, the electromagnetic noise was found to be so strong that it resulted in either the complete malfunctioning of the employed diagnostics or a significant decrease in the signal-to-noise ratio. To eliminate noise interference, all of the implemented diagnostics along with the cables had to be thoroughly shielded and radiation diagnostics were installed inside the shielded enclosure. (iii) For measuring yields below the order of 10^5 neutrons/shot, which is the expected yield for the miniature PF device, neutron detectors such as activation counters (indium/beryllium based) and bubble detectors (which have been commonly used by us in the past [7, 29] for kJ range PF devices) are not effective. Hence, for measuring neutron yields $<10^5$ neutrons/shot, a high sensitivity ^{3}He proportional counter was tailored for this source.

The time resolved information of neutron emission was obtained by a photomultiplier based scintillation detector, where the PMT was coupled to an NE102A plastic scintillator. We also confirmed the neutron emission indirectly by observing >1 MeV proton tracks using a CR-39 solid state nuclear track detector (SSNTD).

The data acquisition system consists of two Yokogawa DL9140, 5GS/s, 1 GHz oscilloscopes and one Tektronix TDS 340 real-time digital oscilloscope and a computer. The synchronization of signals is very important because data analysis requires comparison on the basis of the same time base.

Table 1. Typical values of neutron detection efficiency and gamma ray sensitivity for some common detectors [34].

Detector type	Neutron active material	Incident neutron energy	Neutron detection efficiency (%)	Gamma ray sensitivity ($R\,h^{-1}$)
Plastic scintillator	^{1}H	1 MeV	78	0.01
Loaded scintillator	^{6}Li	Thermal	50	1
Methane (7 atm)	^{1}H	1 MeV	1	1
^{3}He (4 atm), Ar (2 atm)	^{3}He	Thermal	77	1
^{3}He (4 atm), CO_2 (5%)	^{3}He	Thermal	77	10
BF_3 (0.66 atm)	^{10}B	Thermal	29	10

3.1. Electrical diagnostics

It is well known that the current derivative signal, obtained by a Rogowski coil, is a key parameter that provides relevant information regarding the plasma dynamics in the axial acceleration phase and radial collapse (pinch) phase of the PF device. The successful pinch compression is verified by the strong dip in the current derivative signal which is due to the rapid change in plasma impedance [30, 31]. According to Bernard *et al* [31, 32] the increase in plasma impedance is a necessary condition for the good operation of the PF machine for generation of efficient neutrons and x-ray yields. They attributed the large increase in the plasma impedance to (i) fast changing plasma inductance $L_p(t)$ and (ii) growth in anomalous resistance $R_p(t)$ caused by the collisions of electrons with the waves, when they reach a high intensity level. In the present arrangement, an indigenously designed, high bandwidth Rogowski coil of 350 MHz (having a response time of <3 ns) was used. It is to be noted that the rise time of the Rogowski is limited by the length of its winding; therefore it was made from a 15 cm long, 5 mm wide copper strip. The strip winding technique limits the stray inductances and enhances flux coupling [33] that helps to attain high bandwidth response.

3.2. Neutron diagnostics using a ^{3}He proportional counter

The typical neutron yield expected in a miniature PF device as per the existing scaling laws is of the order of $<10^5$ neutrons/shot. This compelled us to tailor a high sensitivity, gas-filled thermal neutron detector, i.e. a ^{3}He proportional counter configured to measure low yields.

To achieve a high neutron-to-gamma discrimination ratio it is necessary that the detector used have minimal gamma ray sensitivity. Table 1 lists the neutron detection efficiency (i.e. interaction probability for neutrons of the specified energy striking the detector face normally) and approximate gamma ray sensitivity for various neutron detectors [34]. The detection efficiency mentioned here is for a single pass through the detector at the specified energy.

It can be concluded from table 1 that amongst all, the ^{3}He gas filled detector is most suitable because of its high neutron (thermal) detection efficiency (typically $\sim$77%) and low gamma ray sensitivity. The cross section for the ^{3}He reaction is 5330*b* for thermal neutrons. It is important to note that the cross section depends strongly on the incident neutron energy E and exhibits a roughly $1/\sqrt{E}$ dependence. Typically ^{3}He has 77% efficiency for thermal neutrons, i.e. $\sim$0.025 eV, 2% at 100 eV, 0.2% at 10 keV and roughly 0.002% at 1 MeV [34]. Because of this strong energy dependence ^{3}He gas filled neutron detector tubes are customarily surrounded by a local moderating medium such as paraffin wax. In our arrangement, a moderator having a thickness of $\sim$10 cm was used to maximize the counting efficiency of the high sensitivity ^{3}He neutron detector tube RP-P4-1636-203 from GE Reuter–Stokes (having a nominal sensitivity length of 36 in. with 2 in. diameter). The thickness of the moderator was estimated using MCNPX simulation for D–D neutrons. This tube was used in the proportional counter mode along with an amplifier, ORTEC 485, and low-noise, fast rise time, charge-sensitive preamplifier, CAEN A424A. TENNELEC TC 948 (0 to +1500 V) was used as an NIM high voltage module. For providing power to various transistorized modules, namely, amplifiers, high voltage supplies, etc the standard NIM bin module 4001 A from ORTEC was used. The layout of the overall neutron detection and instrumentation arrangement is shown in figure 3.

When the neutrons are detected, an analog signal corresponding to the current generated in the ^{3}He detector tube is registered through a preamplifier (CAEN A424A) whose output is directly connected to a digital oscilloscope. The time integrated signal is the charge generated in the ^{3}He tube and it is proportional to the neutron yield. The signal registered on the oscilloscope is integrated using Yokogawa software, XViewer®, and the area under the curve is calculated in microvolt seconds.

To calibrate the ^{3}He detection system (with the moderator included) a beryllium activation counter (previously cross calibrated with an indium detector [29] on the much higher neutron output NX2 PF device) was used. Both of the detectors, the newly adapted high sensitivity ^{3}He and the beryllium activation counter, were used simultaneously in the NX2 PF device detecting neutron yields on the order of 10^6–10^7 neutrons per shot. We estimated the calibration factor for the ^{3}He proportional counter placed at distances of 1–3 m (at 0.5 m intervals) from the NX2 pinch. The variation in the calibration factor with distance is shown in figure 4. For each of the distances shown in figure 4, the calibration factor was estimated using an average of 20 NX2 shots. The calibration factor for the 0.5 m distance of the ^{3}He proportional counter from the neutron source point (because the NX2 has access limitation of >1 m for the big ^{3}He detector tube) was extrapolated, since for the miniature PF we used this distance to estimate the neutron yield. It may however be cautioned that there may be additional uncertainty at this extrapolated point, as that distance is comparable to the size of the detector used.

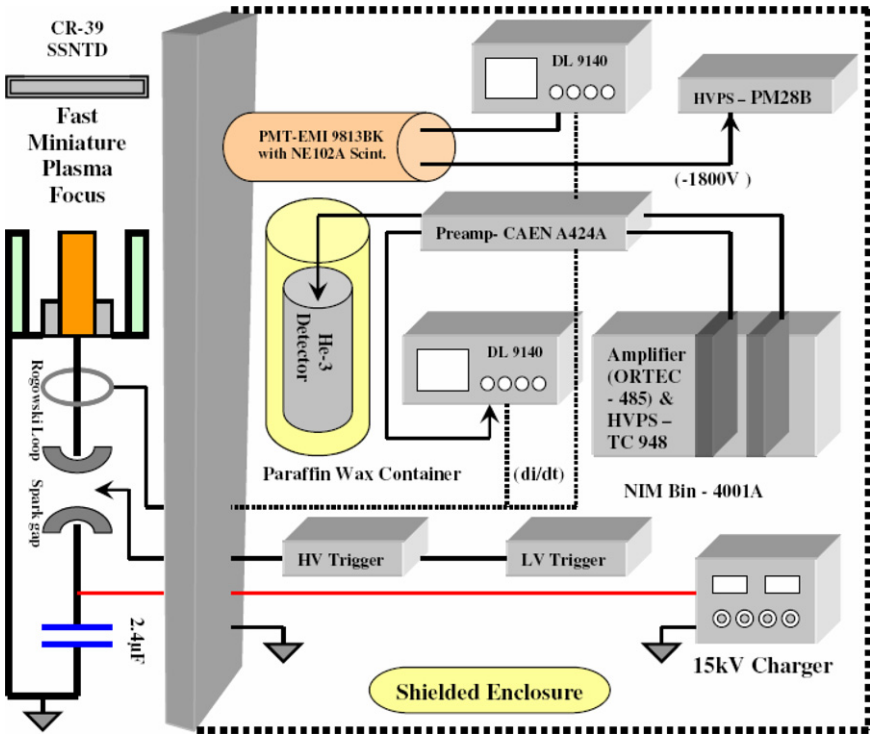

Figure 3. Overall layout of neutron detection and instrumentation set-up.

The bias voltage was kept fixed at +650 V during the entire calibration process.

3.3. Neutron diagnostics using SSNTD (CR-39)

A passive detector such as an SSNTD was also used to confirm neutron production. Imaging of fusion protons using CR-39/PM355 from a 3 kJ deuterium PF was reported by Springham *et al* [35]. Time integrated measurements of the angular distributions of fusion products using CR-39 Lantrack® passive detectors were done by Castillo *et al* [36]. In our arrangement, a CR-39/PM355 plastic track detector from Page Mouldings, UK, of size 2.5 cm × 3.5 cm having a thickness of 1000 μm, was placed on a circular KF40 vacuum flange in the end-on position (see figure 3) at a distance of 15 cm from the anode top and covered with a 50 μm thick Kapton tape. Calculations done using the TRIM code [35, 37] showed that a 50 μm thick Kapton window would pass 2.45 MeV neutrons and the 3.03 MeV protons from the fusion reactions but stop the other charged products of D–D fusion reactions such as 1.01 MeV tritium and the 0.82 MeV ^{3}He nuclei. It is also able to stop the lower energy deuterons as well as impurity ions resulting from electrode erosion. The detection efficiency of the CR-39/PM355 for protons is expected to be 100%.

3.4. Time resolved neutron diagnostics

To acquire time resolved neutron and HXR signals, a 14-stage, high gain photomultiplier tube (EMI 9813BK) coupled with an NE102A plastic scintillator (of thickness 10 mm and diameter 50 mm) having a decay time constant of 2.4 ns was used in the side-on position. A high voltage power supply, model PM28B from Thorn EMI electron tubes, was used to provide −1800 V bias to the photomultiplier tube. The scintillator–photomultiplier tube assembly was jacketed inside a 400 mm long aluminum casing of 10 mm wall thickness to effectively shield it from electromagnetic noise and also visible light.

4. Results and discussion

The results discussed in the following subsections are the average of 20 shots for each of the filling gas pressures and the gas is refreshed after every five shots as a nominal pressure rise of 0.05 mbar was observed after each set of five shots. For the absolute measurement of pressure, a Barocel capacitance manometer (Model 600) from BOC Edwards was used. It has an accuracy of 0.15% in the range of 0–10 mbar. The negative peak of the current derivative signal obtained from the Rogowski coil is taken as the time fiducial reference for all time resolved measurements. The charging voltage was kept fixed at 12 kV throughout the investigation.

4.1. Anode optimization

The current derivative signal of discharge current was used to investigate the effect of anode design/gas parameters on the pinching characteristics of the miniature PF device. The magnitude of the distinct, sharp dip in the current derivative signal is considered as a measure of the pinching efficiency. Higher magnitude of the current derivative dip implies stronger pinching [38, 39] resulting in efficient radiation emission from the pinched plasma column. The four different anode designs that have been studied are shown in figures 5(*a*)–(*d*). Pinching efficiency (measured in terms of peak amplitude of dip in

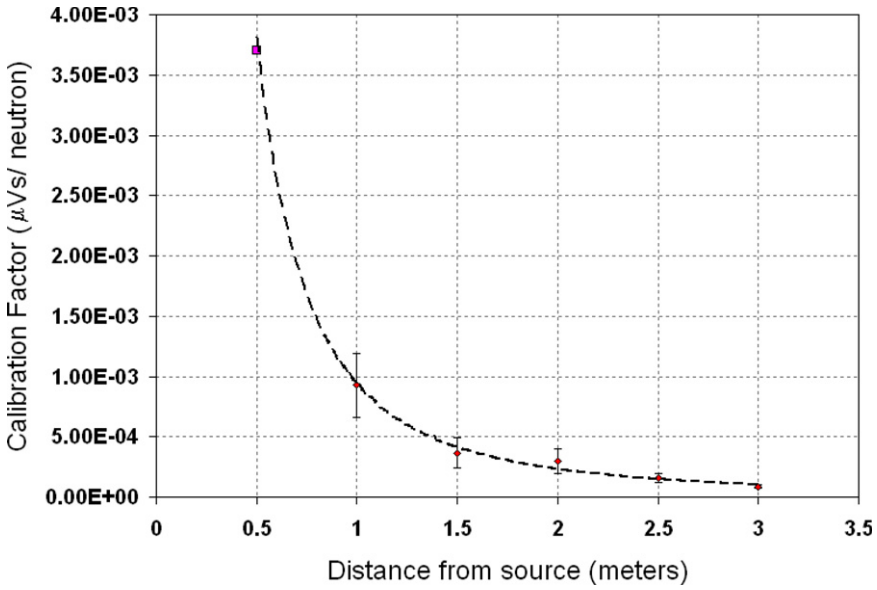

Figure 4. Variation of calibration factor with changing distance of the ^{3}He proportional counter detector from the neutron source point (at a bias voltage of +650 V).

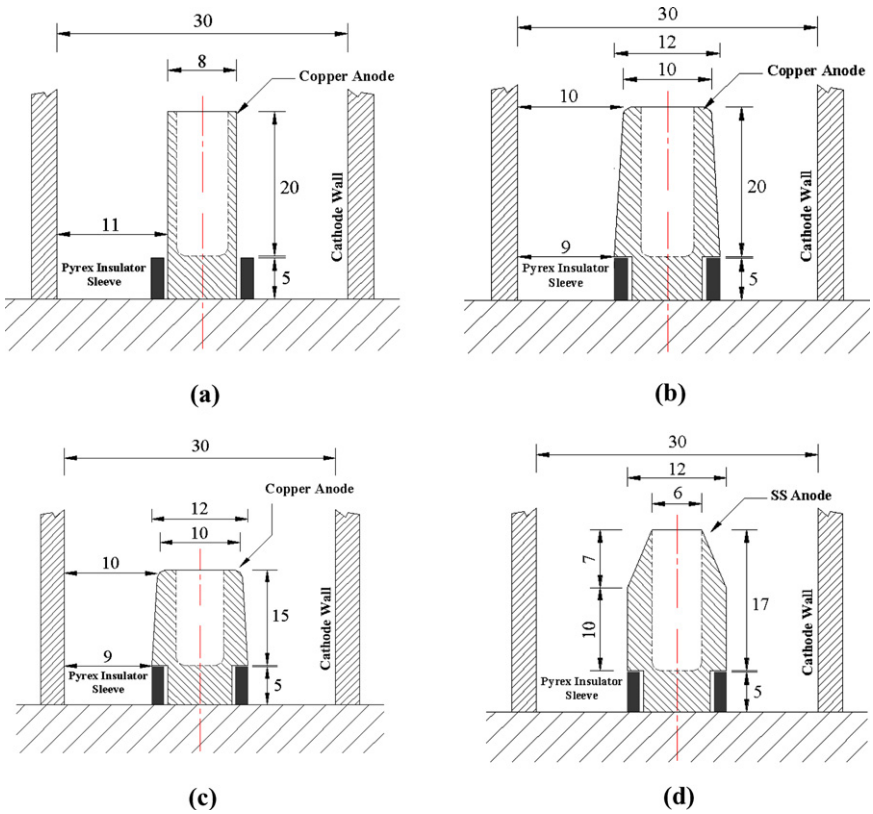

Figure 5. Schematic of various anode geometries used for optimization of FMPF-1. (*a*) Cylindrical flat-end anode(V1/CFA/20-5/Cu). (*b*) Tapered anode (V2/TA/20-5/Cu). (*c*) Tapered anode (V3/TA/15-5/Cu). (*d*) Composite anode (V4/CA/17-3/SS).

the current derivative signal) for different anode geometries is shown collectively in figure 6 for comparative analysis. The figure also includes 'speed factor' curves for the investigated anode designs. The 'speed factor' (also referred to as the drive parameter), i.e. $(I_o/a)/\sqrt{p}$ (here, I_o is the peak discharge current in kA, a is the anode radius in cm and p is the filling gas pressure in Torr), is a measure of driving magnetic energy per unit mass associated with peak discharge current [40] and was considered for analyzing the performance of different anode designs. Across the wide energy range of deuterium optimized, Mather type PF devices, it has a typical value of 89 ± 8 kA cm^{-1} Torr$^{-1/2}$ [41].

The characteristic curves shown in figure 6 illustrate that operating regimes and pinching characteristics of the PF

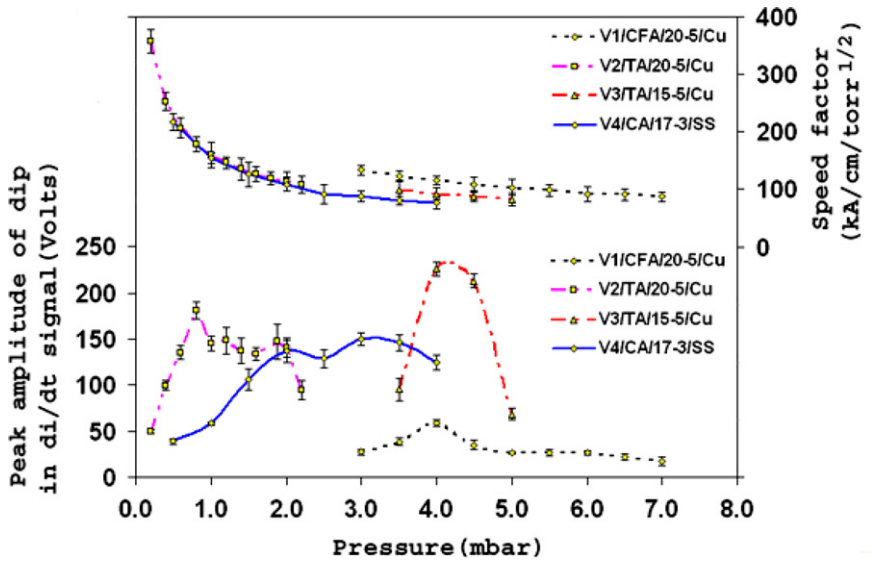

Figure 6. Peak amplitude of dip in the di/dt signal and speed factor for various anode geometries.

device are significantly influenced by anode design/geometry. For the cylindrical flat anode geometry (V1/CFA/20-5/Cu), pinching efficiency was found to be considerably low along with poor reproducibility. This was probably due to delay in the ignition of the breakdown phase across the insulator which in turn will further delay the current sheath buildup time [42, 43], and as the miniature PF has a relatively short quarter time period, its pinching efficiency is significantly affected by the delay in the breakdown phase. As the uniform initiation of the plasma sheath depends crucially on the electric field appearing between the anode and cathode [44], to enhance the electric field and support rapid formation of surface discharge streamers over insulator, in the rest of the anode designs/geometries, the lower end of the anode diameter was extended up to the insulator outer surface with sharp edge periphery, seen in figures 5(*b*)–(*d*), to improve the ignition of the breakdown phase. This resulted in a significant improvement in pinching efficiency and higher reproducibility.

For the second anode design V2/TA/20-5/Cu (see figure 5(*b*)), even though good pinching efficiency was achieved at lower operating pressures, we failed to detect neutrons as well as HXRs. It can be seen from the graph shown in figure 6 that the speed factors at various pressures for this anode are on the relatively higher side ranging from 250 to 113 kA cm^{-1} Torr$^{-1/2}$ in the pressure range of 0.4–2 mbar. Such high speed factors may cause effective separation of the magnetic piston from the plasma layer thereby resulting in inefficient collapse of the plasma layer in the radial phase as the piston continues to drive axially [45]. However, performance of this anode design was found to be favorable for producing high soft x-ray yields [46].

In order to reduce the speed factor (to bring it closer to the typical range of 89 $\pm$ 7 kA cm^{-1} Torr$^{-1/2}$) the third anode geometry V3/TA/15-5/Cu (see figure 5(*c*)) was used with the anode length reduced to 15 mm from 20 mm (for the second anode design). Reduction in the anode length increases the operating pressure to match the arrival time of the current sheath at the anode top with the quarter time period of the capacitor bank. As expected, this anode design performed in the relatively higher pressure regime with the optimum pinching pressure shifted to 4 mbar as compared with 0.8 mbar for the second configuration. However, due to the significantly reduced length it focused efficiently in the very narrow regime of 4 to 4.5 mbar.

To broaden the operating pressure range of optimum pinching, a fourth composite configuration V4/CA/17-3/SS (see figure 5(*d*)) was tested. This anode is made of SS as it has low spark erosion characteristics as compared with copper [26]. In this design, the length of the anode was increased from 15 to 17 mm and a taper was incorporated over the last 7 mm of the anode with the radius gradually tapering from 6 to 3 mm. The decrease in the anode radius from 5 mm (for the third design) to 3 mm (for the fourth design) enhanced the linear current density (i.e. I_0/a) and hence increased the compression efficiency, since dimensions and lifetime of pinches are scaled according to the anode radius [41].

As indicated from characteristic curves shown in figure 6, in experiments with the fourth composite anode geometry, efficient and consistent pinching was observed, over a wide range of operating pressures from 1.5 to 4 mbar. The oscilloscope trace of the typical di/dt pattern for this anode geometry is shown in figure 7. In the rest of this paper, all results and discussions are only for this fourth composite anode design.

The variation in time to pinch from the breakdown phase (which includes axial acceleration phase and compression phase), defined as t_p in figure 7, and the radial phase duration (measured using FWHM of the dip in current derivative signal), defined as t_r in figure 7, at different filling gas pressures is shown in figure 8. The characteristic time t_p increases with the increase in operating pressure due to the slowing down of the current sheath in the axial phase. However, the radial phase duration is almost constant over a wide range of deuterium pressures from 0.5 to 4.0 mbar indicating the consistent focusing in FMPF-1.

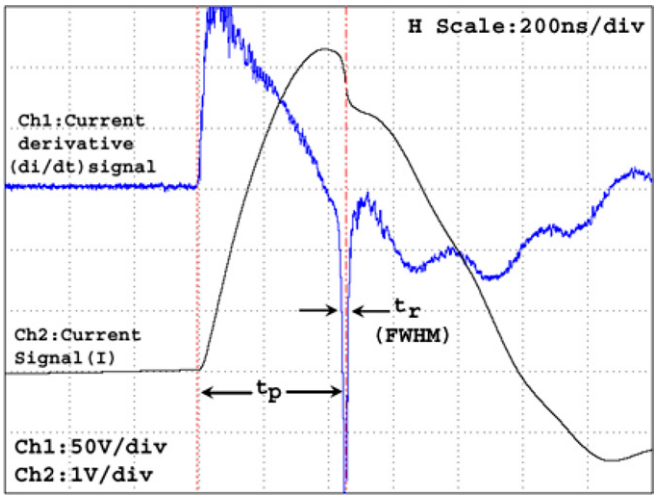

Figure 7. Typical current derivative trace observed in FMPF-1 for shots in deuterium.

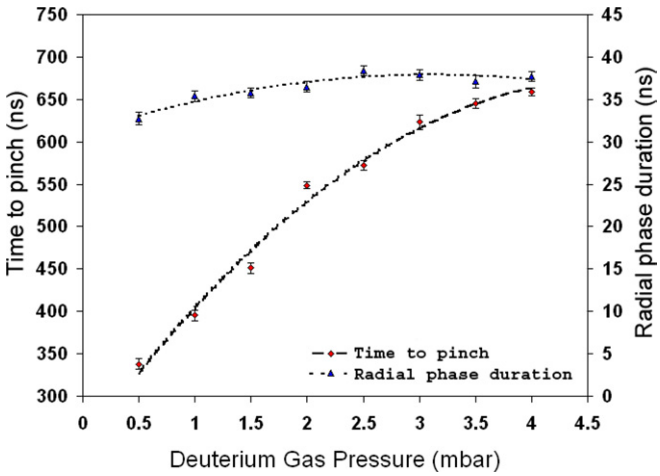

Figure 8. Time to pinch and radial phase duration (FWHM) versus deuterium gas pressure.

4.2. Neutron yield measurement using a ^{3}He detector

The variation of the neutron yield with deuterium gas pressure for the fourth anode design is shown in figure 9. Comparing the graph shown in figure 9 with the pinching efficiency graph shown in figure 6 confirms that the neutron yield maximizes at the highest amplitude of dip in the current derivative signal. The measured average neutron yield (Y_{90°) was $1 \pm 0.27 \times 10^4$ neutrons/shot at 3 mbar gas pressure.

It is observed from figure 9 that there is an optimum pressure which produces a maximum neutron yield. This can be explained using the effect of ambient gas pressure on thermonuclear and beam–target mechanisms. From a thermonuclear point of view, we can use the explanation provided by Moreno *et al* [47] according to which the optimum neutron yield can be achieved provided the peak current occurs simultaneously with pinch (with the neutron yield proportional to I^4). This condition, when expressed mathematically (equation (17) in [47]), was shown to have an interdependence among the anode length, charging voltage and filling gas pressure. If two of the parameters are kept fixed, then the third

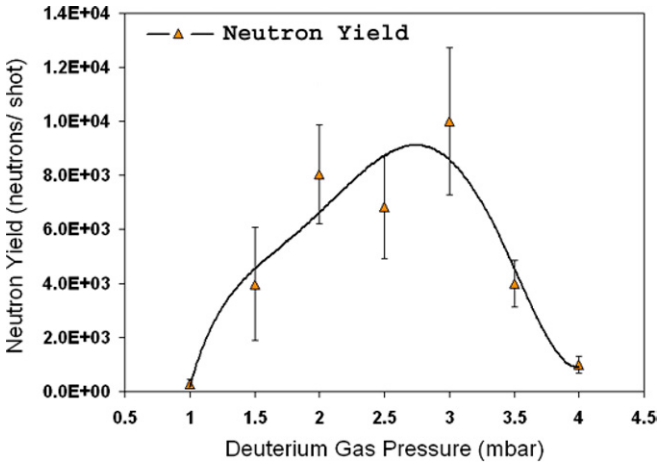

Figure 9. Total neutron yield versus deuterium filling pressure.

can be fine tuned to satisfy the condition for obtaining the optimum yield. Moreover, logically, the initial increase in the filling gas pressure increases the plasma density in the pinch, increasing thereby the reaction rate probability and the neutron yield. But after a certain critical pressure, which depends on the other operating parameters of the focus machine, increasing the pressure does not increase the neutron yield as the time to pinch increases further and the pinch does not occur simultaneously with peak current resulting in lower heating of the pinch plasma and thus lowering of the neutron yield. From the beam–target point of view, one needs strong Rayleigh–Taylor (RT) instability formation for efficient production of accelerated deuterons to produce a higher neutron yield [48]. It may be noted that the growth time for RT instability is give as $\sqrt{2\pi\lambda/g}$ where g is acceleration of the current sheath and λ is the wavelength of perturbation [49]. At lower pressures, the growth rate of RT instabilities will be too high (because of higher acceleration of the current sheath) to allow the formation of a well-defined pinch plasma column resulting in a poor neutron yield. Near the optimum operating pressure, the current sheath acceleration is adequate for efficient instability formation. This results in a strong instability generated deuteron beam resulting in a higher neutron yield by an efficient beam–target mechanism. At pressures significantly above the optimum pressure, the acceleration of the current sheath may be too slow to allow for efficient RT instability formation resulting in a less efficient beam–target interaction leading to a low neutron yield. It may however be noted that since the neutron anisotropy measurements have not been done by us so far it is not appropriate for us to comment on which one is a more dominant mechanism of neutron production in our miniature PF device.

Soto observed the empirical scaling law of $Y \approx 7.73 \times 10^{-5} I_0^{4.82}$ [4], for sub-kilojoule range CCHEN PF-400J and PF-50J PF devices. The peak discharge current in our FMPF-1 is ~70 kA; therefore, following the observed scaling law for sub-kilojoule PF, the expected yield is about $6 \times 10^4\,\mathrm{n\,s^{-1}}$ which is in the same order as measured by us. Even though the neutron yield is on the lower side as compared with the one expected from the observed scaling law, it should be

emphasized that the FMPF-1 produced neutrons with high reproducibility over a wider range of operating gas pressures.

4.3. Simulation 'fitting' results with FMPF-1

The plasma dynamics involved with PF discharges is complicated, as it is inherently 2D in nature and involves radiation hydrodynamics as well. The 'Lee code' [22] provides a useful tool to conduct scoping studies, as it is not purely a theoretical code, but offers a means for the user to conduct phenomenological scaling studies for a given machine, once certain key 'fitting' parameters (such as current and mass fractions) and electrical circuit parameters have been adjusted.

Knowing the short circuit discharge current parameters, the approximate anode length, anode radius and inter-electrode separation were chosen for deuterium operation based on a certain universally known range of typical values of axial acceleration and radial compression speeds. Then the Lee code is used to fine tune the electrode shape, electrode dimensions and operating pressure. The electrode assembly is then constructed and tested. The experimental discharge current traces are then used to fine tune the 'fitting' parameter of the Lee code for that particular electrode design. The possible pressure and voltage regime are explored computationally to optimize the pinching efficiency and the radiation yield. The experiments are then carried out to verify the simulation results and possible modification in the electrode assembly is explored for further enhancement of the radiation yield. Hence, the system works on the mutual feedback mechanism, from simulation to experiment to simulation and then to experiment again, to continuously evolve the electrode shapes and dimension until we get the best results. As an example, in the following paragraph we mention the results for our final version of composite anode geometry (V4).

The following values of 'fitting' parameters were found to have a good fit of the current traces operated for a range of charging voltages and pressures: axial mass factor (f_m) = 0.155; axial current factor (f_c) = 0.6; radial mass factor (f_{mr}) = 0.2 and radial current factor (f_{cr}) = 0.7. The electrical circuit parameters: capacitance (C_0), inductance (L_0) and resistance (R_0), were fixed at 2.4 μF, 32.9 nH and 60 mΩ. The sample current-trace 'fitting' result for the FMPF-1 device operated at 12 kV for deuterium filling at a gas pressure of 3 mbar for composite anode geometry is presented in figure 10. As can be seen, there is a good match with the experimentally measured trace, particularly with respect to the rising and roll-off portions (the portion of the computed current trace near the end of dip requires further investigation). The maximum current 70 kA obtained from simulation matches well with the experimentally obtained current trace. The Lee code [22] simulation predicted a maximum neutron yield of 4.91×10^4 neutrons per shot at 70 kA peak discharge current and 3 mbar D_2 filling gas pressure which is of the same order of magnitude as obtained experimentally.

4.4. Measurements with SSNTD

The CR-39 SSNTD, mounted along the end-on direction at a distance of 15 cm from the anode face, was exposed to five

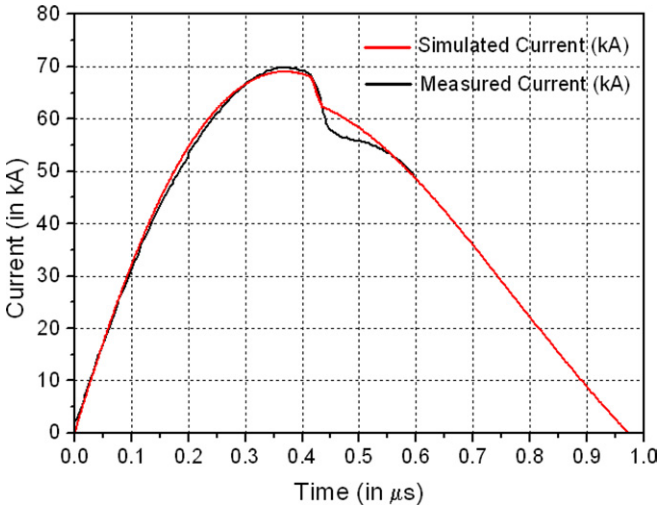

Figure 10. Current-trace 'fitting' result for composite anode.

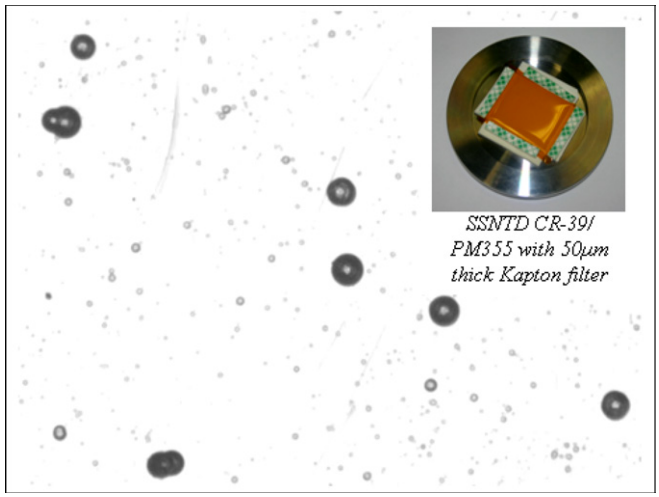

Figure 11. Energetic proton recoil tracks registered on CR-39/PM355 detector at 5× resolution. (A snap of SSNTD along with the filter holding arrangement is shown in the inset.)

PF shots at 3 mbar gas pressure. After irradiation, the detector sample was etched in 6.25 M NaOH solution at a controlled temperature of 70 ± 1 °C for 24 h. Since the 50 μm Kapton filter is thick enough to block the 1.01 MeV T and the 0.82 MeV ^{3}He fusion products, energetic proton recoil tracks of average diameter 38 ± 6 μm were registered on the CR-39 detector. A microphotograph of the etched pits formed on the plastic detector with 5× magnification is shown in figure 11.

Upon scanning the plate area of 25 mm × 30 mm under a high resolution microscope, four recoil tracks were observed in the field of view of size ~208 μm × 160 μm. Our calculations indicate that the yield is typically in the order of $\sim 2 \times 10^5$ neutrons/shot (we have considered neutrons/protons to be essentially forward directed within the angular cone of about 10°). The estimated neutron yield was found to be on the higher side (in comparison with time integrated measurements performed using ^{3}He proportional measurements mentioned earlier), possibly due to background etch pits, representing undistinguishable pseudo tracks. Also, a larger sample size of tracks would improve the statistics.

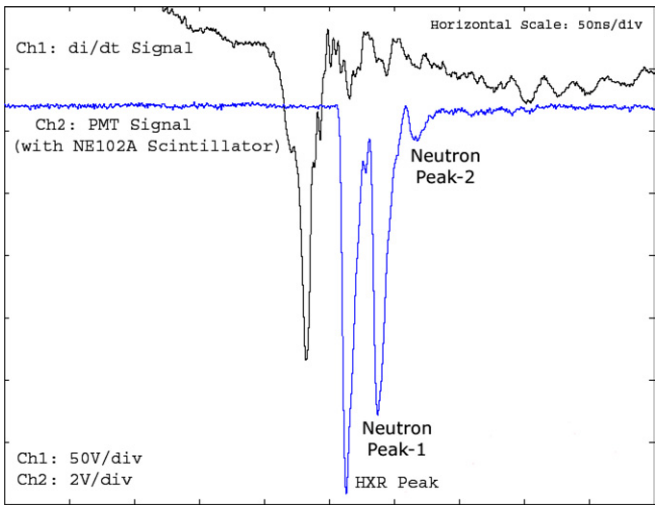

Figure 12. Current derivative ($\mathrm{d}i/\mathrm{d}t$) signal trace with the HXR/neutron signal recorded with a side-on scintillator–photomultiplier detector.

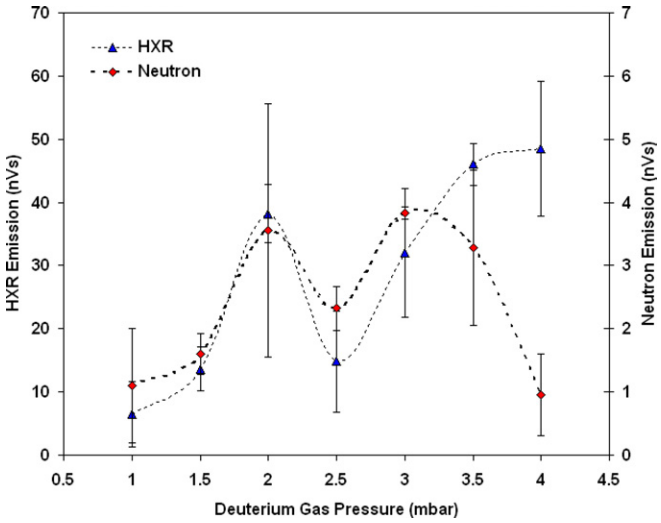

Figure 13. Relative measurements of HXR and neutron emission (area under the curve) estimated from scintillator–PMT detector signals.

4.5. Time resolved measurement of neutron and HXR pulses

The scintillator–photomultiplier detector is located in the side-on position 0.5 m from the focus in order to separate in time the HXR pulse from the neutron pulse. The current derivative and scintillator–photomultiplier signals were recorded simultaneously in a fast digital oscilloscope DL9140; both channels were triggered at the same time and similar lengths of cables were used for both diagnostics. The oscilloscope traces of typical current derivative and scintillator–photomultiplier signals for a PF shot at 3 mbar deuterium gas pressure are shown in figure 12.

The first peak is of non-thermal HXRs produced by the interaction of energetic electrons with the copper anode. It may be important to mention here that there is an inherent delay of ∼30 ns in the photomultiplier tube signal, causing the HXR peak to shift significantly from the peak of the current derivative signal as seen from the graphs shown in figure 12. The second peak is confirmed to be the neutron peak as 2.45 MeV D–D neutrons are expected to arrive about 24 ns after the first HXR peak which matches well with the observed time difference of 23.8 ns between the two peaks. The durations of HXR and neutron pulses, estimated from FWHM of the corresponding peaks, are about 8.9 ± 0.8 ns and 6.9 ± 0.8 ns, respectively, averaged over 20 shots at 3 mbar gas pressure.

Relative measurements (area under the curve) of HXR and neutron emission as recorded by scintillator–photomultiplier detector signals at various pressures are shown in figure 13. As inferred from the graph, initially with the increase in pressure from 1 to 3 mbar the trends in neutron emission follow HXR emission trends with the yield for both maximizing at 2 mbar. It may be noted that for all of the shots, (i) the neutron pulse was registered only after the non-thermal HXR pulse (which is mainly generated due to an accelerated electron beam hitting the anode target) and (ii) the neutron yield predominantly peaked at a peak HXR yield in the operation range of 1–3 mbar filling gas pressure. These observations point to the dominance of the beam–target mechanism in FMPF-1. We plan to perform neutron anisotropy measurements in the near future to confirm the neutron production mechanism in miniature PF. At operating pressures >3 mbar, the neutron yield decreased but the HXR emission was still significant. This can be due to the difference in acceleration mechanisms of ions (specifically deuterons which produce neutrons) and electrons (which produce HXRs).

5. Conclusion

The results presented here demonstrate a proof of concept of a low energy pulsed plasma neutron source based on a cost effective, fast miniature PF device (FMPF-1) producing yield in the order of $\sim 10^4$ neutrons/shot. After performing an experimental study on various anode geometries, it was realized that there are three major issues—good focusing efficiency, speed factor and ignition process (in the breakdown phase), which are critical for efficient performance of miniature PF devices. It is remarkable to note that the speed factor (which describes the axial sheath speed) seems also to strongly influence the radial sheath speed and thus the neutron optimized regime. In other words, the final radial speed is coupled to the axial speed in the coaxial region. Serban and Lee [24, 41] demonstrated this when they first optimized the tapered anodes. Performance of the present device with composite anode geometry confirms that even for the sub-kilojoule range of miniature devices, the speed factor/drive parameter lies in the typical range of 89 ± 7 kA cm^{-1} Torr$^{-1/2}$ for the optimum neutron yield. The yield obtained with FMPF-1 also conforms to the established neutron yield scaling law $Y \approx 7.73 \times 10^{-5} I_{\mathrm{O}}^{4.82}$ for the sub-kilojoule range of PF devices. Further optimization measures such as electrode parameters, operation with admixtures and increase in the discharge current to increase the neutron yield are presently under investigation. To make this compact (0.2 m × 0.2 m × 0.5 m) and low mass device (∼25 kg) useful for potential

applications such as non-invasive interrogation of contraband materials, hidden nuclear materials, medical neutron therapies and soil humidity measurements, the targeted D–D neutron yield generation is about 10^6 neutrons/shot and hence efforts are underway to increase the time averaged fluence by conceptualizing and designing the next generation of high repetition rate miniature PF devices with an upgraded pulsed power system of similar energy.

Acknowledgment

The authors are grateful to the National Institute of Education/Nanyang Technological University, Singapore, for providing the AcRF grant RP 3/06/RSR. The authors also wish to express their gratitude to Cecelia M N Selvam for her assistance in this work. One of the authors, RV, would like to thank NIE/NTU for providing the research scholarship and the parent organization Institute for Plasma Research, Gandhinagar, Gujarat, India, for providing study leave to pursue the PhD Programme at NTU.

References

[1] Mather J W 1964 *Phys. Fluids* **8** 366
[2] Filipov N V, Filipova T I and Vinogradov V P 1962 *Nucl. Fusion (Suppl.)* **2** 577
[3] Rodney P, Bykanov A, Freshman J, Reilly D, Mangano J, Roche M, Dickenson J, Burte M and Heaton J 2004 *Rev. Sci. Instrum.* **75** 2551
[4] Soto L 2005 *Plasma Phys. Control. Fusion* **47** A361
[5] Soto L *et al* 2004 *Brazilian J. Phys.* **34** 1814
[6] Zakaullah M, Akhtar I, Waheed A, Alamgir K, Shah A and Murtaza G 1998 *Plasma Sources Sci. Technol.* **7** 206
[7] Koh J M, Rawat R S, Patran A, Zhang T, Wong D, Springham S V, Tan T L, Lee S and Lee P 2005 *Plasma Sources Sci. Technol.* **14** 12
[8] Mohammadi M A, Verma R, Sobhanian S, Wong C S, Lee S, Springham S V, Tan T L, Lee P and Rawat R S 2007 *Plasma Sources Sci. Technol.* **16** 785
[9] Castillo F, Herrera J J E, Rangel J, Milanese M, Moroso R, Pouzo J, Golzarri J I and Espinosa G 2003 *Plasma Phys. Control. Fusion* **45** 289
[10] Kies W, Decker G, Berntien U, Sidelnikov Y V, Glushkov D A, Koshelev K N, Simanovskii D M and Bobashev S V 2000 *Plasma Sources Sci. Technol.* **9** 279
[11] Czekaj S, Kasperczuk A, Miklaszewski R, Paduch M, Pisarczyk T and Wereszczynski Z 1989 *Plasma Phys. Control. Fusion* **31** 587
[12] Mahabadi T D and Tafreshi M A 2007 *Plasma Phys. Control. Fusion* **49** 1447
[13] Freeman B L, Boydston J L, Guy T L, Rock J C and Luginbill A 2001 *Proc. 27th IEEE Int. Conf. Pulsed Power Plasma Sci. (New Orleans, LA)* p 594
[14] Schmidt H, Kasperczuk A, Paduch M, Pisarczyk T, Scholz M, Tomaszewski K and Szydłowski A 2002 *Phys. Scr.* **66** 168
[15] Brzosko J S, Robouch B V and Klobukowska J 1987 *Fusion Technol.* **12** 71
[16] Silva P, Moreno J, Soto L, Birstein L, Mayer R E and Kies W 2003 *Appl. Phys. Lett.* **83** 3269
[17] Milanese M, Moroso R and Pouzo J 2003 *Eur. Phys. J.* D **27** 77
[18] Silva P, Soto L, Moreno J, Sylvester G, Zambra M, Altamirano L, Bruzzone H, Clausse A and Morenoe C 2002 *Rev. Sci. Instrum.* **73** 7
[19] Mohanty S R, Sakamoto T, Kobayashi Y, Song I, Watanabe M, Kawamura T, Okino A, Horioka K and Hotta E 2006 *Rev. Sci. Instrum.* **77** 043506
[20] Dubrovsky A V and Gribkov V A 2000 *Nukleonika* **45** 159
[21] Bowering N, Martins M, Partlo W N and Fomenkov I V 2004 *J. Appl. Phys.* **95** 16
[22] http://www.intimal.edu.my/school/fas/UFLF/File7RADPF05.13.9b.xls
[23] Verma R, Shyam A and Nair L 2006 *Rev. Sci. Instrum.* **77** 106104
[24] Serban A and Lee S 1998 *J. Plasma Phys.* **60** 3
[25] Shyam A and Rout R K 1998 *Phys. Scr.* **57** 290
[26] Zakaullah M, Ahmad I, Shafique M, Khanam S, Omar A R, Mathuthu M, Murtaza G and Beg M M 1997 *Phys. Scr.* **56** 649
[27] Beg F N, Zakaullah M and Murtaza G 1992 *Phys. Scr.* **46** 152
[28] Rapezzi L, Angelone M, Pillon M, Rapisarda M, Rossi E, Samuelli M and Mezzetti F 2004 *Plasma Sources Sci. Technol.* **13** 272
[29] Mahmood S, Springham S V, Zhang T, Rawat R S, Tan T L, Krishnan M, Beg F N, Lee S, Schmidt H and Lee P 2006 *Rev. Sci. Instrum.* **77** 10E713
[30] Castillo F, Milanese M, Moroso R and Pouzo J 1997 *J. Phys. D: Appl. Phys.* **30** 1499
[31] Bernard A *et al* 1998 *J. Moscow Phys. Soc.* **8** 93
[32] Bernard A, Cloth P, Conrads H, Coudeville A, Gourlan C, Jolas A, Maisonnier C and Rager J P 1977 *Nucl. Instrum. Methods* **145** 191
[33] Verma R, Lee P, Springham S V, Tan T L and Rawat R S 2007 *Rev. Sci. Instrum.* **78** 086107
[34] http://fas.org/sgp/othergov/doe/lanl/lib-www/la-pubs/00326408.pdf
[35] Springham S V, Moo S P, Lee P, Rawat R S, Patran A and Lee S 2005 *Japan. J. Appl. Phys.* **44** 4117
[36] Castillo F, Herrera J J E, Gamboa I, Rangel J, Golzarri J I and Espinosa G 2007 *J. Appl. Phys.* **101** 013303
[37] Springham S V, Lee S and Rafique M S 2000 *Plasma Phys. Control. Fusion* **42** 1023
[38] Castillo F, Milanese M, Moroso R and Pouzo J 2000 *J. Phys. D: Appl. Phys.* **33** 141
[39] Serban A 1995 *PhD Thesis* Nanyang Technological University, Singapore
[40] Zhang T, Rawat R S, Hassan S M, Lin J J, Mahmood S, Tan T L, Springham S V, Gribkov V A, Lee P and Lee S 2006 *IEEE Trans. Plasma Sci.* **34** 2356
[41] Lee S and Serban A 1996 *IEEE Trans. Plasma Sci.* **24** 1101
[42] Zhang T, Lin X, Chandra K A, Tan T L, Springham S V, Patran A, Lee P, Lee S and Rawat R S 2005 *Plasma Sources Sci. Technol.* **14** 368
[43] Hassan S M *et al* 2006 *Plasma Sources Sci. Technol.* **15** 614
[44] Yordanov V, Genov D, Ivanova I and Blagoev A 2004 *Vacuum* **76** 365
[45] Serban A and Lee S 1997 *Plasma Sources Sci. Technol.* **6** 78
[46] Verma R, Lee P, Springham S V, Tan T L, Krishnan M and Rawat R S 2008 *Appl. Phys. Lett.* **92** 011506
[47] Moreno C, Bruzzone H, Martinez J and Clausse A 2000 *IEEE Trans. Plasma Sci.* **28** 1735
[48] Yamamoto T,Shimoda K, Kobayashi K and Hirano K 1984 *Japan. J. Appl. Phys.* **23** 242
[49] Zakaullah M, Akhtar I, Murtaza G and Waheed A 1999 *Phys. Plasmas* **6** 3188

Order of magnitude enhancement in neutron emission with deuterium-krypton admixture operation in miniature plasma focus device

Rishi Verma,[1,a)] P. Lee,[1] S. Lee,[1] S. V. Springham,[1] T. L. Tan,[1] R. S. Rawat,[1,b)] and M. Krishnan[2]
[1]*NSSE, National Institute of Education, Nanyang Technological University, 1 Nanyang Walk, Singapore 637616, Singapore*
[2]*Alameda Applied Sciences Corporation, San Leandro, California 94577, USA*

(Received 5 June 2008; accepted 18 August 2008; published online 8 September 2008)

The effect of varied concentrations of deuterium-krypton (D_2–Kr) admixture on the neutron emission of a fast miniature plasma focus device was investigated. It was found that a judicious concentration of Kr in D_2 can significantly enhance the neutron yield. The maximum average neutron yield of $(1\pm0.27)\times10^4$ n/shot for pure D_2 filling at 3 mbars was enhanced to $(3.14\pm0.4)\times10^5$ n/shot with $D_2+2\%$ Kr admixture operation, which represents a >30-fold increase. More than an order of magnitude enhancement in the average neutron yield was observed over the broader operating range of 1–4 mbars for $D_2+2\%$ Kr and $D_2+5\%$ Kr admixtures. © *2008 American Institute of Physics*. [DOI: 10.1063/1.2979683]

Plasma focus devices are among the least expensive and simplest available pulsed neutron generators that suit a number of potential applications.[1–5] Several attempts have been made to enhance the neutron yield from plasma focus by optimizing various parameters.[6–10] Recently, research and development of fast repetitive miniature plasma focus devices[11,12] with a few hundred joules of stored energy is gaining momentum because of their suitability for various field applications. In this letter we report the results of the effect of varied concentrations of D_2–Kr admixtures on the neutron yield of a fast miniature plasma focus device.

In recent years substantial efforts have been made in investigating the role of high-Z impurity ions on radiation yields. Koshelev *et al.*[13] reported formation of micropinch structures by the addition of heavy gas impurity to the pure deuterium fill. Kies *et al.*[14,15] reported that in admixture operations, two distinct pinch modes are produced: the micropinch mode or the stable column mode, depending on the atomic number of the doping gas. Micropinches are zones of local radiative collapse. According to Lebert *et al.*,[16] such radiative collapse seems to appear only if the atomic number $Z\geq18$ whereas with $Z\leq18$ macroscopically stable pinch columns are formed. It is well known that the Pease–Braginskii current for radiative collapse in a pure hydrogen plasma is ~1.4 MA.[17] As the atomic number of the plasma increases, the bremsstrahlung radiation loss channel is augmented by line radiation channels, which effectively reduce the Pease–Braginskii current to lower values. Koshelev and Pereira[18] gave a formula to estimate this "modified" Pease–Braginskii current. Decker *et al.*[19] reported that in argon-doped deuterium discharges the micropinches preferentially undergo radiative collapse via bremsstrahlung and line radiation from argon. Bayley *et al.*[20] and Antsiferov *et al.*[21] illustrated that admixture of D_2–Ar results in the formation of multiple high density micropinches having structures of high aspect ratio (10:1) with lifetime in subnanosecond regime. Brzosko and Nardi[22] reported formation of superdense domains ($>10^{21}$ cm^{-3}) with admixture operation which resulted in higher neutron yield. Vikherev and Braginski[23] discussed that an admixture of a heavier gas promotes the slipping of the current sheath due to "Hall effect" near the anode.

All the investigations, discussed in the preceding paragraph, have been done for medium (approximately a few kilojoules) to high energy (>10 kJ) plasma focus devices whereas this letter reports the work done on miniature plasma focus device named "FMPF-1" (200 J, 2.4 μF, 27 nH, T/4 ~400 ns). In "FMPF-1,"[24] the electrode assembly consists of a 17 mm long stainless steel anode of composite geometry (tapered over the last 7 mm with diameter decreasing from 12 to 6 mm) and the chamber wall of 30 mm inner diameter acting as cathode. An insulator sleeve of Pyrex glass with a breakdown length of 5 mm is used. To measure time integrated neutron yields, a high sensitivity ^{3}He proportional counter was used. To acquire the time resolved history of emitted radiation, a "dual time of flight" setup was implemented. Three identical scintillator photomultiplier detectors—PMT1, PMT2, and PMT3—each comprising of NE102A plastic scintillator and photomultiplier tube (PMT) EMI 9813B (biased at −1800 V and enclosed inside 1cm thick aluminum casing) were arranged in the radial direction. Two of the detectors, PMT1 and PMT2, were placed at the same distance of 0.5 m from the anode axis. PMT1 was used unscreened where as PMT2 was screened with 1 cm thick lead sheet. PMT3 (screened with 1 cm of lead sheet) was placed at the distance of 1 m from the anode axis. Throughout the experiment, the stored energy of the system was kept constant (12 kV, 70 kA) and the effect of varied concentrations of D_2–Kr admixture (with Kr volumetric ratios of 10%, 5%, and 2%) on neutron and hard x-ray (HXR) emissions was investigated. The results were obtained for averages of 20 shots for every choice of admixture gas pressure.

The measured average neutron yields for various volumetric ratios of D_2–Kr admixture are shown in Fig. 1. Significant enhancement of neutron yield was observed specifi-

[a)]Also at Pulsed Power Group, Institute for Plasma Research, Bhat, Gandhinagar, Gujarat 382428, India.
[b)]Author to whom correspondence should be addressed. Electronic mail: rajdeep.rawat@nie.edu.sg.

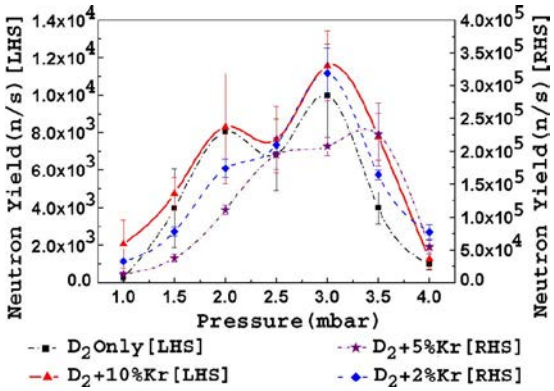

FIG. 1. (Color online) Neutron yields obtained with various impurity concentrations.

cally with $D_2+2\%$ Kr and $D_2+5\%$ Kr admixture ratios. The maximum neutron yield with admixture operation increased by 30, 20, and 1.2 times for $D_2+2\%$ Kr, $D_2+5\%$ Kr, and $D_2+10\%$ Kr, respectively, as compared to pure deuterium operation at 3 mbars.

Time resolved information obtained using PMT1 (Ch2 trace) for pure D_2 filling is shown in Fig. 2. The first peak (PMT1 trace) is of nonthermal HXR whereas the second peak was confirmed to be of neutron on the basis of time of flight consideration. The Ch3 and Ch4 traces, from lead screened PMT2 and PMT3, filter out the HXR pulse and record only the neutron signal. The ~24 ns time difference between the neutron pulses recorded by these two channels confirmed the production of 2.45 MeV D–D neutrons. The duration of HXR and neutron pulses, estimated from full width at half maximum (FWHM) of the corresponding peaks, are about 9 ± 1 and 7 ± 1 ns, respectively. It is important to note here that the appearance of HXR peak (in Ch2 trace) after ~30 ns from the peak of the current derivative signal is because of the latency in PMT.

The PMT1 signal with D_2-Kr admixture operation, as shown in Fig. 3, depicts HXR and multiple neutron pulses. The multiple neutron pulses can also be noticed on traces of Ch3 and Ch4. The relative time difference of ~24 ns between the neutron pulses of Ch3 and Ch4 confirms the presence of 2.45MeV D–D neutrons. The cumulative pulse widths of HXR and neutron pulses are ~20–25 and ~25–35 ns, respectively, for various admixture concentrations.

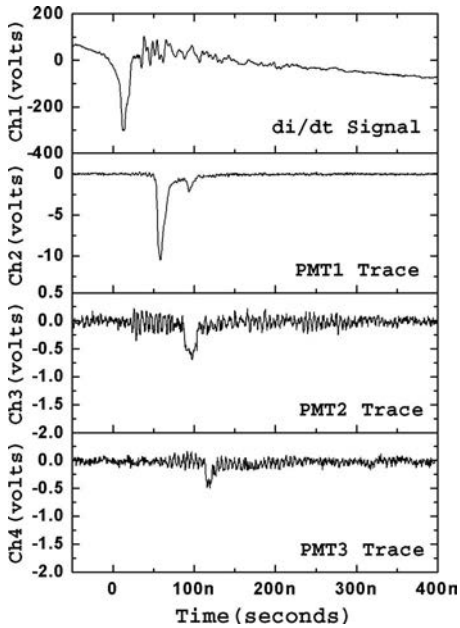

FIG. 2. *di/dt* trace with HXR/neutron signals (D_2 discharge at 3 mbars).

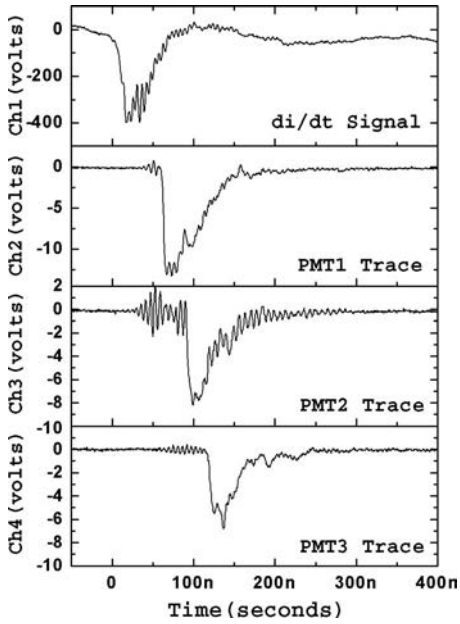

FIG. 3. *di/dt* trace with HXR/neutron signals ($D_2+5\%$ Kr admixture discharge at 3 mbars).

The relative HXR yields, area under the identified HXR peaks, at various pressures for different admixture combinations are shown collectively in Fig. 4. The trends of increase in HXR yield predominantly follow the trends for neutron yields, indicating that the Kr admixture enhances the contribution of the nonthermal mechanism in neutron production.

The observation of multiple HXR and neutron pulses in Kr seeded operation with enhanced yields can be explained by hypothesizing the formation of several successive micropinches initiated by radiative collapse in high-Z admixture operation. It is well known that the use of high-Z impurity increases the effective ion charge (Z_{eff}) of deuterium plasma. For the fully ionized pure deuterium plasmas, there are three mechanisms that control the kinetic pressure of the plasma: Ohmic heating rate, radiative cooling rate, and rate of change in current. In general, the Ohmic heating rate is larger than the radiative cooling rate until the time at which the pinch current (I_{pinch}) exceeds the Pease–Braginski critical

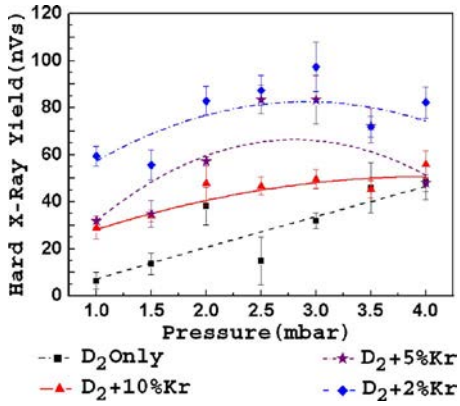

FIG. 4. (Color online) HXR yield for D_2 and D_2-Kr admixtures at different pressures.

value (I_{PB}).[25] Beyond the Pease–Braginski current limit, radiative losses exceed the Ohmic heating rate. As the high-Z ions in a <1 keV plasma are not fully stripped, line radiation dominates over bremsstrahlung. Thus, for high-Z admixture plasma, I_{PB} no longer provides the correct power balance relationship. Instead, power balance occurs at a critical current (I_{cr}) which is much less than Pease–Braginski current limit (I_{PB}). Shearer[26] theoretically showed the Pease–Braginski current limit (I_{PB}) of 650 and 110 kA for 1% carbon and 1% argon impurity pinches, respectively.

According to Koshelev and Pereira,[18] the critical current limit for radiative collapse to occur largely depends on effective ion charge (Z_{eff}) and nuclear charge (Z_n) for the plasma of heavy ions; therefore even a small amount of heavy ion impurity drastically modifies the energy balance in the plasma due to intense radiative losses. Heavier atoms, such as Kr, are not fully stripped. For example, 1 keV plasma would ionize the Kr down to the Ne-like stages (Kr^{26+}); therefore many different bound-bound transitions are possible and this makes the high-Z ions radiate copiously. Thus, radiation cooling enables the magnetic field to compress the plasma to a higher density and smaller final radius[26,27] (micropinch), while maintaining the plasma in a Bennett-like state where the average kinetic pressure inside the column is in equilibrium with magnetic pressure at the edge of the plasma.[25] Hence, micropinch formations due to addition of high-Z impurity in pure D_2 in the correct proportion lead to neutron yield enhancement.

Time resolved investigation of current derivative (di/dt) signals of D_2 and D_2-Kr admixtures (referred to as Ch1 in Figs. 2 and 3, respectively) indicates that radial phase duration, FWHM of the dip, averages to 30 ± 5, 35 ± 3, 39 ± 4, and 50 ± 4 ns for pure D_2, $D_2+10\%$ Kr, $D_2+5\%$ Kr, and $D_2+2\%$ Kr, respectively. This infers that the high-Z Kr impurity also plays an effective role in pinch stabilization, depending on the impurity concentration ratio. The magnitude of the dip of the negative spike in the current derivative signal, a measure of focusing efficiency, for D_2-Kr admixture is on an average of ~1.5 times higher than pure deuterium gas discharges. Thus, D_2-Kr admixture, with appropriate volumetric ratio, not only plays an important role in enhancing neutron and HXR yield but it also broadens the optimum pressure regime and stabilizes the pinch for longer duration. Enhancement in pinch stabilization is also supported by the fact that Rayleigh–Taylor instability growth time (which is known to be $t_i=\sqrt{2\pi\lambda/a}$, where a is the sheath acceleration and λ is the wavelength of perturbation) increases as a consequence of slowing down of current sheath with high-Z admixture operation,[28] also observed in Poseidon plasma focus.[29]

In conclusion, our study illustrates that if judicious concentration of Kr in D_2 is used (by adding just enough Kr to optimally enhance the radiation by radiative collapse, but not enough to affect the implosion through the higher atomic mass of the Kr atoms) along with adjustment of the base pressure such that the swept mass allows the time for first radial collapse to coincide with the peak current, then D_2-Kr admixtures can significantly enhance the radiation yields. The improved pinch stabilization and higher plasma density through improved compression, actuated by radiative collapse, explains vigorous enhancement in neutron and HXR yields for D_2-Kr admixture operation.

The authors are grateful to the National Institute of Education/Nanyang Technological University, Singapore for Scholarship grant and AcRF Grant No. RP 3/06/RSR.

[1] V. Gribkov, A. Dubrovsky, L. Karpinski, R. Miklaszewski, M. Paduch, M. Scholz, P. Strzyzewski, and K. Tomaszewski, AIP Conf. Proc. **875**, 415 (2006).
[2] A. V. Kuznetsov, A. V. Evsenin, I. Yu. Gorshkov, O. I. Osetrov, and D. N. Vakhtin, Appl. Radiat. Isot. **61**, 51 (2004).
[3] E. Ergisto, A. Tartari, M. Frignani, V. Molinari, D. Mostacci, F. Rocchi, and M. Summi, Nucl. Technol. Radiat. Prot. **20**, 33 (2005).
[4] V. Benzi, F. Mezzetti, F. Rocchi, and M. Sumini, Nucl. Instrum. Methods Phys. Res. B **213**, 611 (2004).
[5] J. Pouzo, M. Milanese, and R. Moroso, AIP Conf. Proc. **669**, 277 (2003).
[6] A. Shyam and R. K. Rout, Phys. Scr. **57**, 290 (1998).
[7] F. N. Beg, M. Zakaullah, G. Murtaza, and M. M. Beg, Phys. Scr. **46**, 152 (1992).
[8] M. Zakaullah, T. J. Baig, S. Beg, and G. Murtaza, Phys. Lett. A **137**, 39 (1989).
[9] J. M. Koh, R. S. Rawat, A. Patran, T. Zhang, D. Wong, S. V. Springham, T. L. Tan, S. Lee, and P. Lee, Plasma Sources Sci. Technol. **14**, 12 (2005).
[10] M. Zakaullah, A. Waheed, S. Ahmad, S. Zeb, and S. Hussain, Plasma Sources Sci. Technol. **12**, 443 (2003).
[11] I. V. Fomenkov, N. Böwering, C. L. Rettig, S. T. Melnychuk, I. R. Oliver, J. R. Hoffman, O. V. Khodykin, R. M. Ness, and W. N. Partlo, J. Phys. D **37**, 3266 (2004).
[12] P. Silva, J. Moreno, L. Soto, L. Birstein, R. E. Mayer, and W. Kies, Appl. Phys. Lett. **83**, 3269 (2003).
[13] K. N. Koshelev, V. I. Krauz, N. G. Reshetniak, R. G. Salukvadze, Y. V. Sidelnikov, and E. Y. Khautiev, J. Phys. D **21**, 1827 (1988).
[14] W. Kies, G. Decker, U. Berntien, Y. V. Sidelnikov, D. A. Glushkov, K. N. Koshelev, D. M. Simanovskii, and S. V. Bobashev, Plasma Sources Sci. Technol. **9**, 279 (2000).
[15] W. Kies, B. Lucas, P. Röwekamp, F. Schmitz, G. Ziethen, and G. Decker, Plasma Sources Sci. Technol. **7**, 21 (1998).
[16] R. Lebert, A. Engel, and W. Neff, J. Appl. Phys. **78**, 6414 (1995).
[17] A. E. Robson, Phys. Rev. Lett. **63**, 2816 (1989).
[18] K. N. Koshelev and N. R. Pereira, J. Appl. Phys. **69**, R21 (1991).
[19] G. Decker, W. Kies, R. Nadolny, P. Röwekamp, F. Schmitz, G. Ziethen, K. N. Koshelev, Y. V. Sidelnikov, and Y. V. Sopkin, Plasma Sources Sci. Technol. **5**, 112 (1996).
[20] J. M. Bayley, G. Decker, W. Kies, M. Maizig, F. Muller, P. Rowekamp, J. Westheide, and Y. V. Sidelnikov, J. Appl. Phys. **69**, 613 (1991).
[21] P. S. Antsiferov, F. B. Rosmej, O. N. Rosmej, H. Schmidt, D. Schulz, and A. Schulz, J. Appl. Phys. **77**, 4973 (1995).
[22] J. S. Brzosko and V. Nardi, Phys. Lett. **155A**, 162 (1991).
[23] V. V. Vikherev and S. I. Braginski, Rev. Plasma Phys. **10**, 425 (1986).
[24] R. Verma, P. Lee, S. V. Springham, T. L. Tan, M. Krishnan, and R. S. Rawat, Appl. Phys. Lett. **92**, 011506 (2008).
[25] W. Thornhill, J. L. Giuliani, Jr., and J. Davis, J. Appl. Phys. **66**, 4154 (1989).
[26] J. W. Shearer, Phys. Fluids **19**, 1426 (1976).
[27] J. Bailey, A. Fisher, and N. Rostoker, J. Appl. Phys. **60**, 1939 (1986).
[28] L. Bilbao and H. Bruzzone, Phys. Lett. **101A**, 261 (1984).
[29] H. Schmidt, M. Sadowski, L. Jakubowski, E. S. Sadowska, and J. Stanislawski, Plasma Phys. Controlled Fusion **36**, 13 (1994).

Applied Surface Science 255 (2008) 2932–2941

Contents lists available at ScienceDirect

Applied Surface Science

journal homepage: www.elsevier.com/locate/apsusc

Nano-phase titanium dioxide thin film deposited by repetitive plasma focus: Ion irradiation and annealing based phase transformation and agglomeration

R.S. Rawat [a,*], V. Aggarwal [a], M. Hassan [b], P. Lee [a], S.V. Springham [a], T.L. Tan [a], S. Lee [a]

[a] Natural Sciences and Science Education, National Institute of Education, Nanyang Technological University, NIE BLK7, 1 Nanyang Walk, Singapore 637616, Singapore
[b] Department of Physics, GC University, 54000 Lahore, Pakistan

ARTICLE INFO

Article history:
Received 30 May 2008
Received in revised form 10 August 2008
Accepted 19 August 2008
Available online 28 August 2008

PACS:
52.58.Lq
52.77.Dq
68.55.−a
68.47.Jn

Keywords:
Crystalline titanium dioxide
Nano-phase
Repetitive plasma focus device

ABSTRACT

We report the successful deposition of nano-phase crystalline titanium dioxide (TiO_2) thin films using a repetitive plasma focus device on silicon (Si) substrates at room temperature. The plasma focus device, fitted with solid titanium anode was operated with argon–oxygen admixture as the filling gas. X-ray diffraction (XRD) patterns of as-deposited films confirm the deposition of crystalline TiO_2 thin films having polymorphism nature; anatase and rutile, and their relative phase transition and crystallinity improvement by increasing the number of ion irradiation shots and/or annealing temperature. The crystallite sizes of the TiO_2 particulates estimated from the typical diffraction peaks are found to be approximately 8 nm and 13 nm. The weight ratios of anatase and rutile in the TiO_2 were estimated and it was revealed that anatase weight fraction was reduced by increasing the total ion irradiation and/or annealing temperature, owing to phase the transformation from anatase to rutile. Raman studies have also established the dominant presence of E_g and A_{1g} Raman active modes of the rultile phase. Scanning electron micrographs (SEM) of the as-deposited films reveal uniformly distributed nano-phase morphology over the film surface. Agglomeration of smaller TiO_2 nano-sized grains, to form bigger sized particulates, is seen to occur owing to the clustering of charged nucleates in the gas phase. The agglomeration is enhanced by increasing the number of ion irradiation shots and/or annealing temperature.

1. Introduction

Thin films of titanium dioxide (TiO_2), being versatile material, have been the subject of sustained research interests due to their diverse electronic and photonic applications. Titania (TiO_2) is known to exist in amorphous form and crystallizes in three distinct crystallographic structures: two tetragonal phases, anatase (a = 3.785 Å, c = 9.514 Å) and rutile (a = 4.593 Å, c = 2.959 Å) and a third orthorhombic phase, brookite (a = 5.456 Å, b = 9.182 Å, c = 5.143 Å). Rutile, known to be the most stable phase, is applied in white pigments (e.g. in cosmetic products and paints) and various optical devices due to its high chemical stability, UV absorbance and refractive index. Owing to its good blood compatibility, rutile can be used as artificial heart valves [1] and plays a key role in the biocompatibility of bone implants. Anatase, a metastable phase which can readily oxidize, is widely used as a photocatalyst [2,3] in various fields such as environmental purification, sterilization and deodorization. In general, TiO_2 is also utilized in electrodes of electrochemical and dye-sensitized solar cells [4]. Particularly due to its high permittivity, high physical and chemical stability and the acceptance for most modern CMOS fabrication facilities, TiO_2 has extensively been investigated as a possible SiO_2 replacement for the fabrication of new generation of dynamic random access memories (DRAMS) and micro-electromechanical systems [5]. TiO_2 has been investigated for use in heterogeneous catalysis, in solar cells for the production of hydrogen and electrical energy, as a corrosion protective coating, as an optical coating, as a gas sensor, in electronic devices (such as varistors) and in ceramics. Generally, high crystallinity of TiO_2 is desired in its applications as a photocatalyst and as an electrode of a photovoltaic device. TiO_2 is a possible candidate among the gate insulators because its rutile type has a high dielectric constant of approximately 80 and good thermal stability on Si.

Various techniques including sputtering [5,6], chemical vapor deposition (CVD) [7], ion beam-assisted deposition, reactive evaporation [6], laser-assisted evaporation, sol–gel process [8] and spray pyrolysis [9] have been employed for the preparation of titanium oxide films. Mardare et al. [5,10] deposited amorphous TiO_2 thin films on the substrates at room temperature using RF sputtering. Many authors have reported crystalline TiO_2 thin film

* Corresponding author. Tel.: +65 67903930.
E-mail address: rajdeep.rawat@nie.edu.sg (R.S. Rawat).

0169-4332/$ – see front matter © 2008 Elsevier B.V. All rights reserved.
doi:10.1016/j.apsusc.2008.08.055

deposition at low substrate temperatures [11–15]. Low temperature deposition of crystalline films is of particular interest in the thin film industry as it eliminates the requirement for substrates that can tolerate high temperatures, and thus reduces the production cost. In this connection, a technique that can easily control the polymorph of TiO_2 on the substrate surface at room temperature during synthetic process is industrially of immense interest. The present investigations report, for the first time, the use of high performance, high repetition rate plasma focus device for the successful deposition of crystalline TiO_2 thin films on Si substrate at room temperature.

The dense plasma focus (DPF) device [16] is a simple pulsed plasma device in which electrical energy of a capacitor bank, upon discharge, is converted into plasma energy resulting in the formation of a short lived, but hot (≈1–2 keV) and dense ($\approx 10^{25-26}\,m^{-3}$) plasma. The plasma focus device is a source of neutrons, highly energetic ions, relativistic electrons and X-rays [17–19]. Being a source of such a wide range of phenomena, the device has found applications in other areas too [20]. Highly energetic ions from the plasma focus have been used for processing of various thin films [21–26] irradiated at different distances from the top of the anode. The plasma focus device has also been used for implantation of nitrogen [27] and carbon [28] ions into different metallic substrates, and for deposition of thin films of carbon [29,30], fullerene [31], titanium carbide [32] and titanium nitride [33,34]. The plasma focus-assisted thin film deposition has shown that this pulsed plasma device possesses interesting features of high deposition rates, energetic deposition and possible film formation under a reactive background gas pressure.

The present work reports the deposition of nano-phase crystalline TiO_2 thin films having polymorphism nature (anatase and rutile) on Si substrates at room temperature using DPF device in repetitive mode. The TiO_2 films are deposited for multiple number (25, 50, 75, 100, 150 and 200) of focus shots and are then annealed at different temperatures of 573 K, 773 K and 973 K for 1 h in air ambient in order to systematically investigate their structural and morphological properties, and to reveal their phase dependence based on total ion irradiation and annealing parameters.

2. Experimental setup

2.1. The deposition system

The deposition of TiO_2 thin films was accomplished by using a repetitive DPF device designated as Nanyang X-ray source-2 (NX2). The NX2 is a high performance (12 kV, 400 kA), high repetition rate (up to 16 Hz) DPF device, which was specially designed for applications like soft X-ray microlithography. Conventionally, the electrode assembly of the NX2 possesses a hollow copper anode surrounded by 12 cylindrical copper cathode rods in a squirrel cage fashion. For the deposition of TiO_2 films, the central hollow copper anode was replaced with a copper anode fitted with a solid titanium top of 99.95% purity. The schematic of experimental setup showing various subsystems of the NX2 device is sketched in Fig. 1.

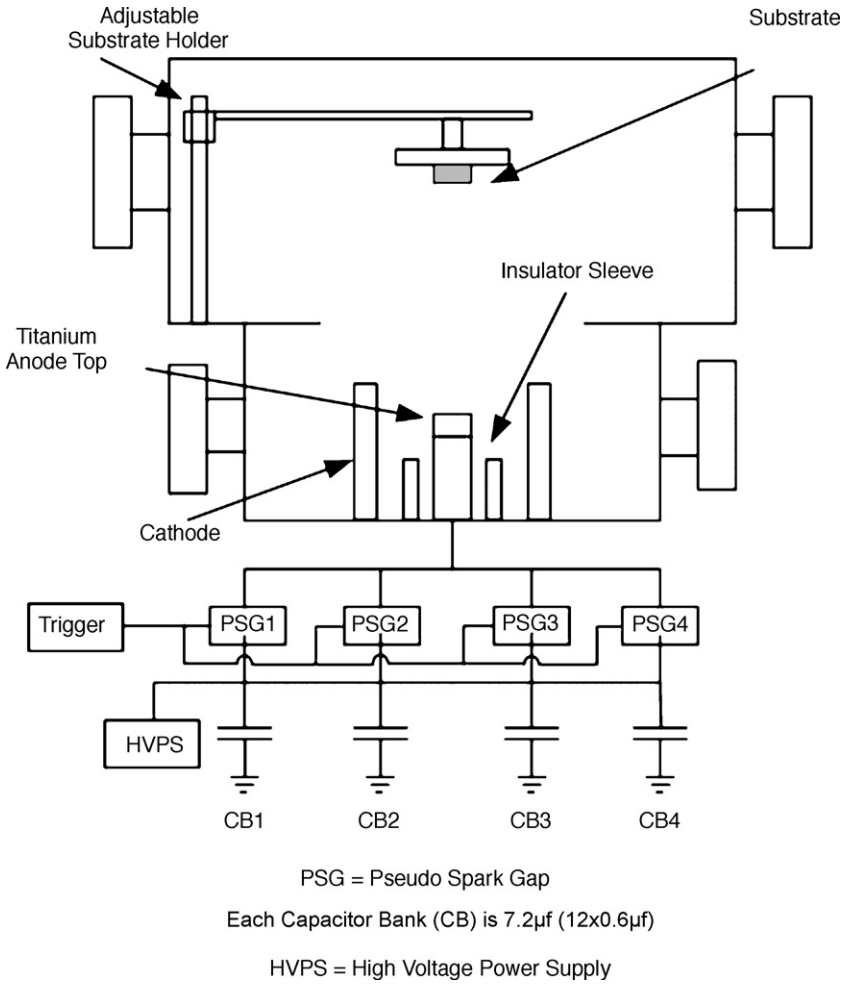

Fig. 1. The schematic of the dense plasma focus device employed for TiO_2 thin film deposition.

Table 1
The operating parameters of plasma focus device for preparation of TiO_2 film

Operating parameters	Description
Base pressure	5×10^{-5} mbar
Filling gas pressure	2 mbar
Oxygen partial pressure	0.2 mbar
Charging voltage	10.5 kV
Capacitor bank	28.8 μF (48 μF × 0.6 μF)
Peak discharge current	350 kA
Repetition rate used	0.2 Hz
Substrate temperature	Room temperature (295 K)

The experimental parameters for the deposition of TiO_2 are provided in Table 1. The base pressure of the order of 5×10^{-5} mbar was achieved in the deposition chamber using a turbo molecular pump. The argon–oxygen admixture in the pressure ratio 9:1 was used as the working gas at the optimum pressure of 2 mbar to ensure strong focusing. When the electrical energy stored in the capacitor bank (four modules of 12 μF × 0.6 μF, 30 kV capacitors) is transferred to the focus chamber by low inductance pseudo-spark gap switches, the gas breakdown occurs initially across the surface of the insulator separating the anode and the cathode. This breakdown, under the influence of Lorentz forces, proceeds on to form uniform, axis symmetrical current sheath in inverse pinch phase before being accelerated down the anode axis in axial rundown phase. Upon reaching the top of the anode, the current sheath collapses radially inward during the final focus phase resulting in the formation of hot dense plasma at the top of the anode. The plasma temperature is sufficiently high to cause complete ionization of the filling gas species. Oxygen, being one of the filling gas species, supplies ions in almost all ionization states [35]. The formation of hot dense plasma is followed by the onset of sausage instabilities. A sausage ($m = 0$) instability is a magneto-hydrodynamic instability which is developed in the cylindrical plasma column, such as pinched plasma column of focus device, carrying a strong axial current due to imbalance between the inward magnetic pressure and outward kinetic pressure. This instability enhances the induced electric field locally, and hence breaks the focus plasma column [36]. This leads to the acceleration of gaseous ions with very high energies (50 keV to few MeV) towards the top of the chamber and relativistic electrons towards the anode, which ablate the anode material. The ablated plasma consisting of titanium ions and neutrals reacts with the oxygen ions of the filling gas to form TiO_2, which is deposited on the Si substrate.

2.2. Film deposition

TiO_2 films were deposited on 10 mm × 10 mm × 0.625 mm fine polished P-doped Si (100) substrates. The substrates were ultrasonically cleaned in acetone, alcohol and de-ionized water sequentially for 10 min each. Films were deposited at ambient substrate temperature using multiple focus shot exposures. The very advantage of the repetitive NX2 device over a single shot device is its high repetitive rate performance unlike a conventional single shot DPF device usually operated in manual trigger mode at a rate of one shot in 30 s to 1 min. Substantial thickness of films can be achieved in a short duration of time using a repetitive DPF device. However, in the repetitive mode, the substrate temperature may increase as a result of energetic ions bombardment if no cooling arrangement is provided. In this regard, the temperature rise of the substrate exposed at 12 cm or above the anode axis for 100 shots of DPF operated at different repetition rates, was explored by using a *k*-type thermocouple interfaced to a computer. For 2.0 Hz repetition rate, the substrate temperature rose from room temperature of 295 K to about 310 K. The reduction in the repetition rate was observed to cause a small substrate temperature rise, typically 1–2 K for 0.2 Hz repetition rate, which was fixed for the present investigations.

Noticeably, the deposition of films such as TiC [32] and TiN [33,34] along the anode axis at lower axial distance have been reported with significant surface damage by the last treatment shot because of the maximum energy and flux of ions along the axis. Eventually, the deposition of those films was conducted at different angular positions (referred as off-center and outermost position) with respect to the anode axis. In the present investigations, the deposition however has been done along anode axis by keeping the substrate at much higher distance of 33 cm. This is to ensure that the energetic ions while traversing through the longer filling gas path should loose enough energy and cause less damage to the film surface. Moreover, this arrangement will also ensure uniform film deposition over a larger area due to fountain like geometry of the ion beam in DPF device. This was accomplished by placing another vacuum chamber above the main chamber of the NX2 device as shown in Fig. 1.

The deposition of thin films on Si substrate in room temperature environment was carried out using multiple number (25, 50, 75, 100, 150 and 200) of focus shots. The as-deposited films were annealed at temperatures of 573 K, 773 K and 973 K for 1 h in air ambient. The main motivation of annealing the films, at above-mentioned temperatures, is to investigate the effectiveness of energetic ion-assisted deposition in plasma focus device in reducing the phase transition temperature, from anatase to rutile phase, from typically observed temperature of about 673 K to lower values.

2.3. Film characterization

The crystallography of the as-deposited and annealed TiO_2 thin films was studied by employing a SIEMENS D5005 X-ray diffractometer having a Cu Kα source. The detector scan mode at grazing incidence of 3° was used to perform 2θ scans over the 20–60° range. The chemical state of the TiO_2 films was analyzed using a Renishaw MicroRaman spectrometer, with a spectral resolution of 1 cm^{-1}. The surface morphology of the films was studied using a JEOL JSM-6700F field emission scanning electron microscope. In order to prevent charge build up, a thin gold film was coated on the substrates during analysis.

3. Results and discussions

3.1. Structural studies

Fig. 2 shows XRD spectra of the as-deposited titania thin films on Si substrate at room temperature for different number of deposition shots viz. 25, 50, 75 and 200. In the notation of Miller indices, "A" indicates anatase-type crystal and "R" indicates rutile-type crystal. The XRD spectra reveal that the film deposited for 25 shots is predominantly composed of anatase phase having a broad diffraction peak (0 0 4) at $2\theta = 37.21°$ (Powder Diffraction pattern 00-021-1272) along with a weak diffraction peak (1 0 1) at $2\theta = 35.51°$ of rutile phase (Powder Diffraction pattern 00-002-0494). The film deposited for 50 shots shows the presence of a weak peak at $2\theta = 40.13°$ (1 1 1) attributable to the rutile phase and a strong rutile peak at $2\theta = 35.51°$ (1 0 1) along with the anatase (0 0 4) peak shoulder. For the film deposited for 75 shots, (1 1 1) rutile peak appears at $2\theta = 40.06°$ and the strong rutile peak (1 0 1) appears at $2\theta = 35.26°$ with an increasing peak shift with the increasing ion irradiation. For the increasing ion irradiation of 50,

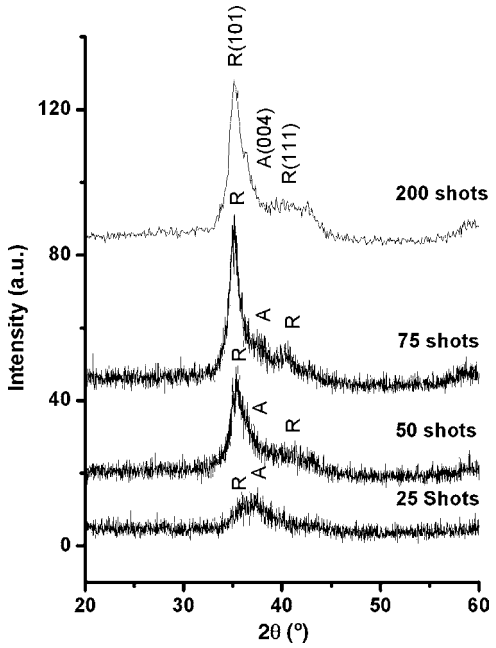

Fig. 2. XRD spectra of as-deposited TiO_2 thin films for different number of shots, at room temperature.

75 and 200 shots, the rutile phase is predominantly evolved with (1 0 1) plane orientation instead of (1 1 0) preferred plane orientation. The crystalline nature of the titania thin films as-deposited at room temperature substrate using multiple focus shots and transformation of anatase to rutile phase during post-annealing (discussed later) at temperature much below than the transition temperature reported in the Powder Diffraction pattern makes the present investigation different from most of the studies reporting amorphous titania thin films grown on substrates at room temperature [5,13]. The observed crystallinity of the films can be explained on the basis of characteristic features of plasma focus-based deposition technique and deposition parameters.

During the DPF discharge, ions of argon and oxygen contributed by filling gas species are much more energetic than titanium ions contributed by ablation of anode material. Moreover, the filling gas species ions are formed and accelerated earlier than the ablated titanium ions. These energetic filling gas species ions reach the substrate first causing etching and hence cleaning of the substrate surface prior to deposition and are then followed by the deposition of the TiO_2 compound on the substrate. It has been suggested that the TiO_2 thin film growth occurs via a chemical reaction between substrate surface and atoms, ions and/or molecules in the gas phase, which impinge on the substrate. The decomposition of predecessor molecules (e.g. O_2) in the gas phase or on the substrate, results in atoms or reactive species (ions and radicals, e.g. O^+, O^{2+}, etc.), which migrate to and diffuse along the substrate surface. Such ions and radicals having multiple charged states have been reported to be emitted from the plasma focus. Rhee [37] has investigated the charged state information of a variety of ion species, emitted either from a solid metallic anode of the plasma focus or the injected gases. For a simple case of He, it was revealed that only singly charged ions were of relatively low energy, whereas all of the higher energy ions were doubly charged states. It has been well established that the ions having singly and doubly charged states (O^+ and O^{2+}) are the most probable ion species in the entire ion spectrum because the energy spectrum contains maximum of comparatively low energy ions as compared to the higher energy ions acquiring higher charged states. Thus, the chemically active background gas oxygen ions react with the subsequent Ti ions (Ti^+, T^{++}, etc.) to form charged nucleates of titania (usually TiO^+ and $TiO_2{}^+$), which are then deposited on Si substrate. The thin film is a self-assembly of such reactive species, which grows via a gas phase nucleation during their flight. Thus, in the case of dense plasma focus with reactive background gas, the deposition mode is usually a CVD, where the gas phase nucleation is the primary step towards the film growth process. Also, every time a shot is fired, energetic filling gas species ions go firstly to the thin film deposited for previous shots. This provides the additional energy required for surface diffusion and migration, and thus improves the crystallinity of the thin film. During the successive ions bombardment, free energy (contributed mainly by the internal energy and the vibrational entropy of the atoms) of the topmost zone of the film deposited for the previous shot/shots may increase leading to the redistribution/phase transition of the film and an eventual stress evolution in it. Nevertheless, the DPF energetic ion-assisted deposition helps restoring the equilibrium state of the film deposited for the previous shot because of the significant transient temperature rise during the short pulse (about 100 ns for low energy DPF) gaseous ions bombardment, in addition to the film growth by the deposition of charged nucleates usually TiO^+ and $TiO_2{}^+$. The equilibrium restoration of the film is also reflected by the transformation of metastable anatase phase to more stable rultile phase by increasing number of ion irradiation shots. Thus, the film growth proceeds along with the phase transformation by increasing the number of shots. The rapid temperature rise during ions bombardment by each successive shot may assist the migration of defects within the film and thus improves its crystallinity as well.

Fig. 2 also demonstrates the number of ion exposure shots dependent phase transition from anatase to rutile phase in the as-deposited films. Such DPF ion-assisted redistribution/phase transitions in thin films have already been reported [38,39]. During DPF ions irradiation, the substrate surface recrystallizes due to the adsorption of the energetic species onto the surface forming new phases. The DPF ions adsorbate-induced reconstruction yields multiphase structures with the minimization of the surface-free energy of substrate [39]. The random impurity dispersion by thermodynamic means may require a quenching procedure from a high transient temperature phase. The impurities (pre-deposited nucleates) may cluster, move to dislocations or form new phases with various stoichiometries [38]. The bombardment of energetic ion species influences the grain growth in the vicinity, i.e. the impingement of ions on the growing surfaces can create new nucleation sites. The phase transition may be considered to be the growth of new crystalline titania phase (rutile) owing to the momentum transfer from the impinging particles to the growing surface. In order to redistribute the film microstructure, the impinging ion species need to possess sufficient kinetic energy to surpass the potential barriers associated with the phase transformation. This corresponds to the crystalline nucleation energy of rutile TiO_2. Hassan et al. [34] have investigated that not only the energy but also the ion flux is the key parameter for DPF ion-assisted phase transformation. The anatase to rutile phase transformation by the DPF ions is considered to require such intrinsic threshold ions flux, hence the total ion exposure, which determines the phase transformation. In argon–oxygen plasmas, the density and energy of the gaseous particles (e.g. TiO^+ and $TiO_2{}^+$) play an important role in the growth of a particular titania phase. Thus, certain minimum total ion irradiation (more than 100 shots for the present case) is required for rutile phase growth. The continuous impingement of ions possessing sufficient kinetic energy transfers momentum to the growing surface by surpassing the potential barriers associated

with the phase transformation and thus increases the surface energy of the film, which helps in its redistribution by minimizing its surface energy as explained earlier. For the present Ar + O_2 discharge, this is actually accompanied by the creation of oxygen vacancies in the film during successive impingement, and is therefore reflected by the poor crystallinity of the films as-deposited for lower number of ion irradiation shots. However, an increase of the number of ion irradiation shots increases the surface energy that is minimized by redistribution of the film microstructure forming new nucleation sites (rutile phase). This redistribution/phase change mechanism is accelerated for higher number of ion irradiation shots due to the defects migration already produced in the film with preceding lower ion irradiations. Eventually, the crystallinity is improved dominantly for rutile for higher number of ion irradiation shots.

Fig. 3 shows XRD spectra of the titania thin films deposited for 20, 50 and 75 shots and annealed at 773 K to reveal the annealing effect on the growth and crystallinity of the films. Annealing of films improves the rutile phase growth, thus showing more than two diffraction peaks. In addition to the significant phase growth in new plane orientations A(1 0 1), R(1 1 0), A(2 0 0) and R(2 1 1), the (1 1 1) rutile peak is also comparatively intense than that in the respective as-deposited film. Similar patterns, with higher peak intensities, were observed for films deposited for 100, 150 and 200 shots. The deviation of positions of a few peaks from their corresponding Powder Diffraction data by less than 0.1° demonstrates the presence of stresses in the films, induced by energetic ions bombardment. Note that for lower number of ion irradiation shots (25, 50 and 75 shots) there is still phase competition in the films annealed at comparatively lower temperature of 773 K. Nevertheless, the annealing based phase transformation can be accomplished for films as-deposited for comparatively lower number of ion irradiation shots, the effect of number of ion irradiation shots on phase transformation for as-grown films is significant for higher number of ion irradiation shots (100 shots and above).

The phase transformation from anatase to rutile mainly depends on substrate temperature, oxygen partial pressure and deposition rate. Tang et al. [40] revealed an anatase to rutile phase transformation temperature of about 673 K in Ar + O_2 atmosphere (20–30% oxygen, 1.5 kV × 0.4 A power and 0.5 Å/s deposition rate). It has also been well investigated that phase transformation temperature depends on background gas pressure, stress, contaminants, oxygen deficiency etc. in the substrate. The rutile phase is usually quenched in the thin film form even when the film is grown at temperature below the transition temperature [41]. The phase transformation from anatase to rutile for the film deposited at room temperature and annealed at 773 K in air ambient is a similar kind of quenching in the as-grown TiO_2 films. Since the oxygen vacancies are introduced not only during the film deposition in the present Ar + O_2 atmosphere but also by annealing stoichiometric TiO_2 films in the reducing atmosphere of air ambient. This facilitates the defects migration, and eventually the phase transformation from anatase to rutile may be accelerated [42] even at 773 K instead of saturating anatase phase as-deposited favorably for lower number of ion irradiation shots.

The annealing of TiO_2 at still higher temperatures results in the transformation of metastable anatase to stable rutile phase, owing to the surface-free energy minimization as revealed by many researchers. Fig. 4 shows XRD spectra of the films deposited for 200 shots (as-deposited and annealed at different temperatures of 573 K, 773 K and 973 K). It may be noted that as the annealing temperature increases, the shift in diffraction peaks also reduces which can be attributed to relaxation of stresses in the film (discussed at the end of this section). The as-deposited films for 200 shots due to their substantial thickness are expected to have high stress as compared to annealed films, which were deposited for 200 deposition shots. In Fig. 4, the (1 0 1) rutile peak for as-deposited film is located at $2\theta = 35.10°$ and gradually shifts to $2\theta = 36.10°$ which is almost same position as being reported in corresponding Powder Diffraction data. Annealing at higher temperature provides more energy for surface diffusion and increases the mobility of deposited species, which leads to high crystallinity. The rearrangement of atoms and evolution of (1 1 0), (1 0 1), (1 1 1), (2 1 0), (2 1 1) and (2 2 0) rutile peaks is well reflected by XRD spectra of the films deposited for 200 shots and annealed at successive higher temperatures as shown in Fig. 4.

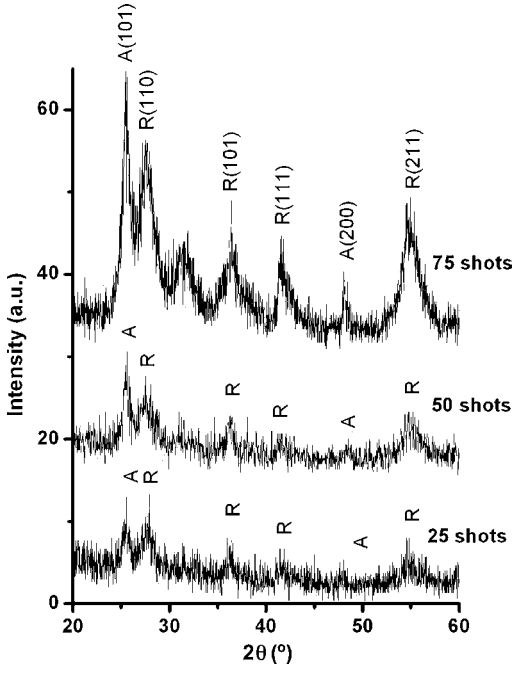

Fig. 3. XRD spectra of TiO_2 thin films deposited for different number of shots and annealed at 773 K.

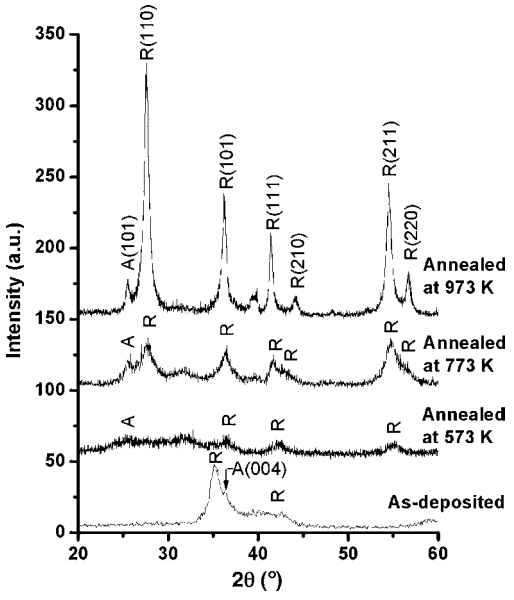

Fig. 4. XRD spectra of TiO_2 thin films deposited for 200 shots for as-deposited and annealed samples at different temperatures.

Scherrer's formula was used for the calculation of crystallite sizes, which is as follows:

$$D = \frac{0.9\lambda}{\beta \cos\theta}$$

where D is the crystallite size, λ the X-ray wavelength used (1.5418 Å), β the broadening of diffraction line measured as full width at half-maxima (FWHM) and θ the corresponding angle. The broadening of the peak is obtained by fitting to Lorentzian distribution. The crystallite sizes of the TiO_2 were found to be approximately 8 nm and 13 nm corresponding to as-deposited film for 50 and 75 shots, respectively, estimated from strong (1 0 1) rutile peak.

The residual stresses in the TiO_2 films have been evaluated by using the X-ray diffraction data. The shifting of diffraction peaks from their respective stress-free data indicates a uniform stress developed normal to the corresponding crystal plane in the film during rapid cooling after transient temperature rise by ion irradiation. Refer to Fig. 3 (film deposited for 75 shots), (1 1 1) rutile peak is shifted to $2\theta = 40.06^\circ$ and strong rutile peak (1 0 1) is shifted to $2\theta = 35.26^\circ$. The shifting of diffraction peaks from their corresponding Powder Diffraction data ((0 0 4) anatase peak at $2\theta = 37.78^\circ$, whereas (1 1 1) and (1 0 1) rutile peaks at $2\theta = 41.22^\circ$ and $2\theta = 36.08^\circ$, respectively) indicates the presence of stresses, reflecting a change in d-spacing of a typical hkl plane. Such stresses have been well reported in the plasma focus-based thin films [34]. In the commonly used Bragg–Brentano method [43], which operates in the θ–2θ scan mode, the residual stress is calculated quantitatively using following expression:

$$\sigma = -\frac{E}{\nu}\left(\frac{d_n - d_0}{d_0}\right)$$

where E, υ, d_n and d_0 are, respectively, the Young's modulus (Pa), Poisson's ratio, d-spacing (Å) of the diffraction plane parallel to the surface of the film under stress and the d-spacing (Å) of the same series of stress-free planes. Substituting the modulus of elasticity of 230 GPa and Poisson's ratio of 0.27 for TiO_2, the residual stress in the as-deposited film, corresponding to strong (1 0 1) rutile peak is found to vary from 13.2 GPa to 22.3 GPa by varying the focus shots from 50 to 200 and is shown in Fig. 5(a). It is observed that increasing number of shots initially increase residual stresses in the thin film, which tend to saturate after 150 shots. The saturation may be due to slight increase in substrate temperature for large number of focus shots that helps in stress relaxation.

The weight ratios of anatase and rutile in the titania were measured quantitatively using the following equation [44]:

$$W_{an} = \left[\frac{1}{1 + 1.265(I_{ru}/I_{an})}\right] \times 100$$

where W_{an} is the weight fraction of the anatase phase, I_{an} and I_{ru} are the intensities of the strongest anatase and the strongest rutile reflections, respectively. Note that the ratio I_{an}/I_{ru} is independent of fluctuations in diffractometer characteristics. For the present case, I_{an} and I_{ru} correspond to the (0 0 4) anatase and (1 0 1) rutile peaks, respectively, when measured for the films as-deposited for various number of ion irradiation shots. A systematic trend showing suppressing effect of ion irradiation (25–200 shots) on the weight fraction of anatase in the mixed phase (titania) is sketched in Fig. 5(b). Thus, ion irradiation-based phase transformation from anatase to rutile is confirmed by the decreasing anatase weight fraction W_{an} in the as-deposited films. W_{an} reduces significantly from 52% for the films as-deposited for 25 shots to 18% for those as-deposited for 200 shots. The smallest W_{an} for the film deposited for 200 shots shows significant phase transformation by the ion irradiation. Annealing temperature has also lead to the anatase to rutile phase change, in addition to the crystallinity improvement of the entire mixed phase of titania. Initially, by annealing the film, W_{an} has been found to increase from 18% for as-grown films for 200 shots to 47% for the same films annealed at 573 K, owing to the overall crystallinity improvement of titania. However, on further increasing the annealing temperature, the phase transformation phenomenon comes into play and W_{an} reduces eventually. W_{an} has been found to reduce from 47% for the film deposited for 200 shots and annealed at 573 K to 18% for the film deposited for the same fluence but annealed at 973 K. The effect of annealing temperature (573–973 K) on the weight fraction of anatase in titania films all deposited for 200 shots is also displayed in Fig. 5(b). Present results adequately report the anatase to rutile phase transformation based on total ion irradiation and/or annealing temperature, and also agree strongly with the Raman spectroscopy investigations. In fact, the amount of ion irradiation plays similar role of thermal excitation of film microstructure, leading to restructuring and phase transformation as that of thermal agitation by annealing.

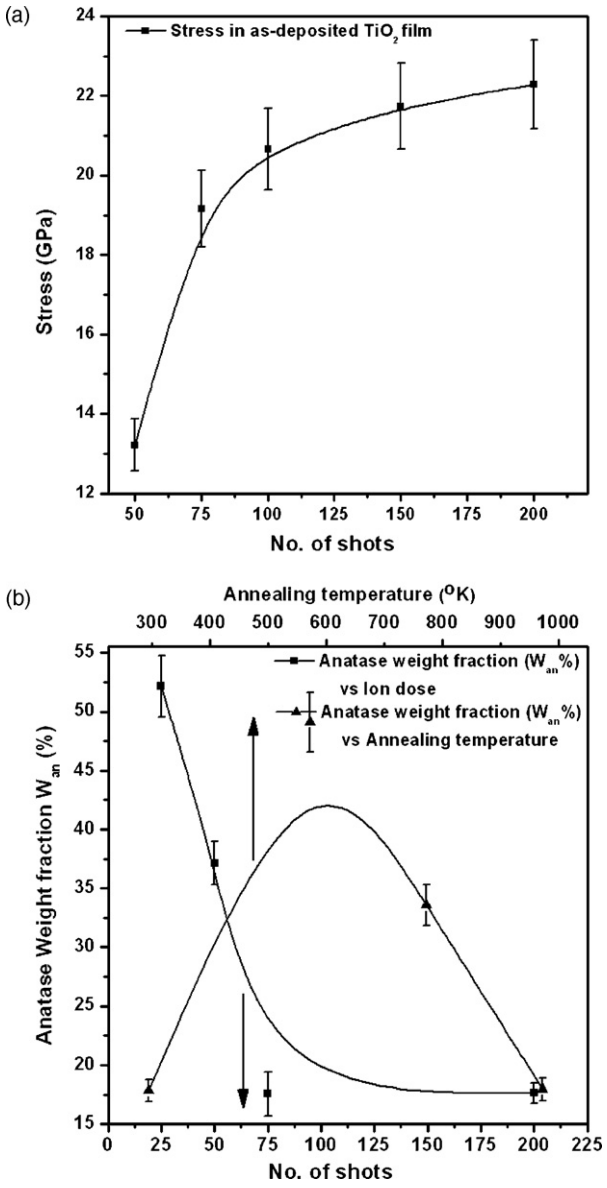

Fig. 5. Variation of (a) stress developed for as-deposited TiO_2 thin films corresponding to (1 0 1) rutile peak, vis-a-vis ion exposure shots, and (b) anatase weight fraction (W_{an}) vis-a-vis ion exposure shots and annealing temperature.

3.2. Chemical state investigations

Raman spectroscopy was used to characterize the chemical structure of the films. Fig. 6 shows Raman spectra of the TiO_2 films as-deposited for different number (25, 50, 75, 100, 150 and 200) of shots. For as-deposited films, a small peak at 142 cm^{-1} and a broad peak centered about 230–260 cm^{-1} indicate the nano-phase titania (TiO_2) film. The Raman lines at 450 cm^{-1} and 610 cm^{-1} clearly appear for films deposited for 150 as well as 200 shots. These peaks correspond to the E_g and A_{1g} modes of the rutile, respectively. The presence of the rutile Raman modes indicates that the high temperature rutile phase was stabilized at room temperature on samples prepared at higher focus deposition shots, i.e. at temperatures much lower than the bulk transformation temperature from the anatase to rutile. Such a conclusion is consistent with the XRD results shown in Figs. 2–4. Films become increasingly rutile for the increasing number of shots.

Fig. 7 shows Raman spectra of the TiO_2 films deposited for multiple number (25, 50, 75, 100, 150 and 200) of shots and annealed at 773 K. After annealing, the emergence of a Raman line at 515 cm^{-1} that can be assigned to the A_{1g} mode of the anatase phase becomes quite evident. Although annealing of the films significantly improves their crytallinity, as is depicted by the more intense Raman modes appearing for both the phases, the effect of annealing at 773 K is more pronounced for anatase rather than for rutile. However, further increasing the annealing temperature to 973 K improves the crystallinity of TiO_2 films, dominantly for the rutile favorably grown for higher number of ion irradiation shots, as shown by the intense peaks corresponding to the E_g and A_{1g} Raman modes of rutile (Fig. 8). Furthermore, it is observed that as the annealing temperature increases, the rutile modes at 450 cm^{-1} and 610 cm^{-1} become stronger while the anatase mode gets weaker. From the Raman investigations, it is revealed that the crystallinity of TiO_2 films can be improved both by the amount of ion irradiation and/or the annealing. The increasing ion irradiation favors the growth of stable rutile phase than that of metastable anatase phase. The annealing of films at low temperature transforms anatase to rutile phase along with the improvement of overall film crystallinity. But, the annealing of films at higher temperature dominantly grows rutile than anatase. The Raman investigations are quite consistent with the XRD results.

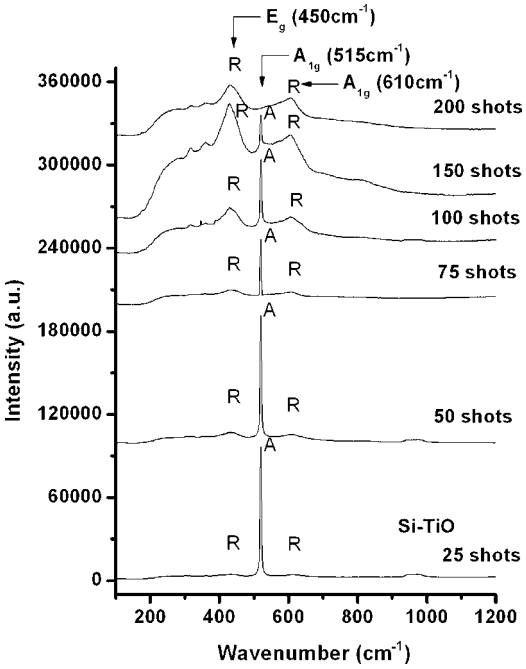

Fig. 7. Raman spectra of TiO_2 thin films deposited for different number of shots, annealed at 773 K.

3.3. Morphology

The effect of increasing ion exposure and annealing temperature on the surface morphology of TiO_2 films deposited on silicon

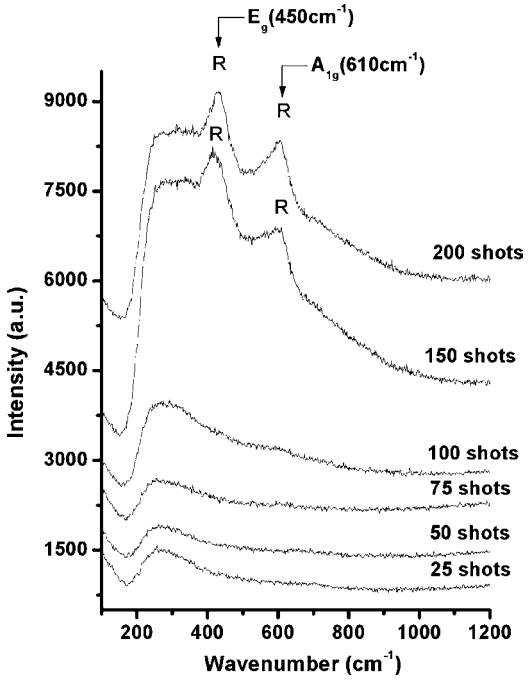

Fig. 6. Raman spectra of the as-deposited TiO_2 thin films for different number of shots.

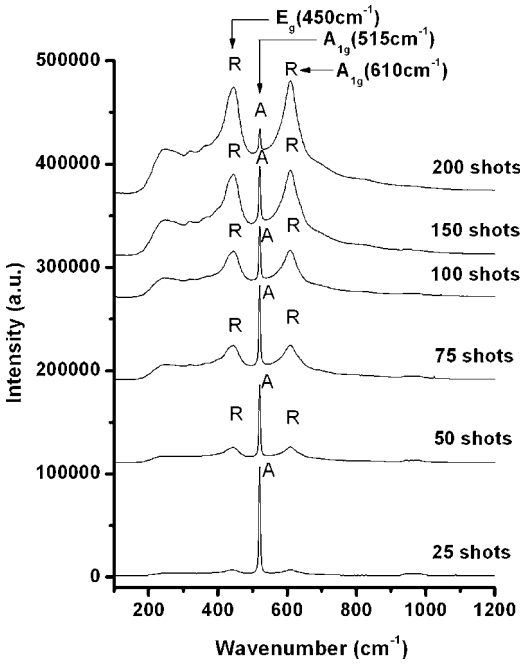

Fig. 8. Raman spectra of TiO_2 thin films deposited for various number of shots, each annealed at 973 K.

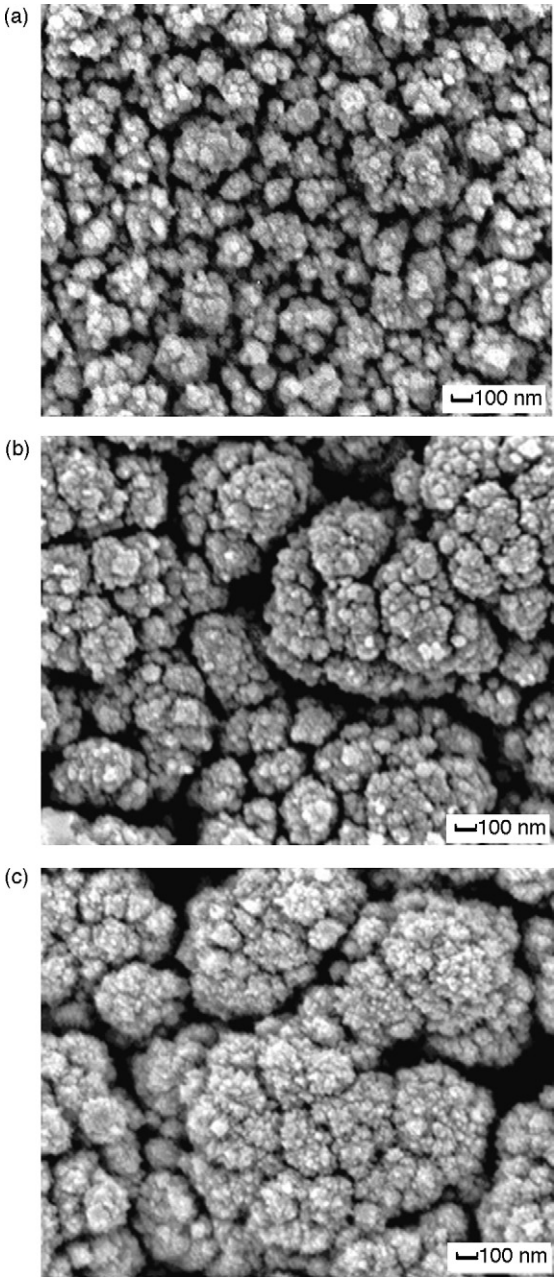

Fig. 9. SEM micrographs of the as-deposited TiO_2 films for (a) 25 shots, (b) 100 shots and (c) 200 shots.

wafers has been investigated by using SEM. Fig. 9 shows SEM micrograph of the films as-deposited for multiple number (25, 100 and 200) of shots. The surface morphology of these films is almost identical. However, agglomeration of grains is observed for higher number of shots. The surface morphology of the film deposited for 25 shots (Fig. 9(a)) shows the presence of individual nano-phase grains of 10–20 nm size and also the agglomerates of grains to form particulates of the sizes of 100–200 nm distributed over the substrate surface. The surfaces of films deposited for 100 shots (Fig. 9(b)) are seen to be composed of much bigger sized particulates of about 300–800 nm size. A close view of the particulates reveals that they are the aggregates of many smaller nano-sized grains or particulates. The surface of the film grown for 200 shots (Fig. 9(c)) exhibits further agglomeration, with the particulate size distribution of a few 100 nm to a few microns.

An increase in the energetic ion irradiation causes more energy being transferred to the film surface leading to greater mobility of nanoparticles and hence resulting in bigger sized agglomerates. This observation also supports our argument of the crucial role being played by the total energy deposited by energetic ions on morphologies of film surfaces. This can be elaborated under the theory of charged clusters (TCCs) [45,46] and the thermal coagulation phenomenon. The DPF has been investigated to be a rich source of ions and/or radicals having multiple charged states [35], such ions nucleate in the gas phase to form charged nucleates of titania (usually TiO^+ and TiO_2^+), which are then deposited on the substrate to grow thin film, as explained earlier. The clusters can grow either by reactions with reactive species in the gas phase or combining with very small uncharged clusters (well explained by the TCC). This also limits the size of a cluster. In our case, the gas phase nucleation has resulted in the cluster size of about 100–200 nm that makes

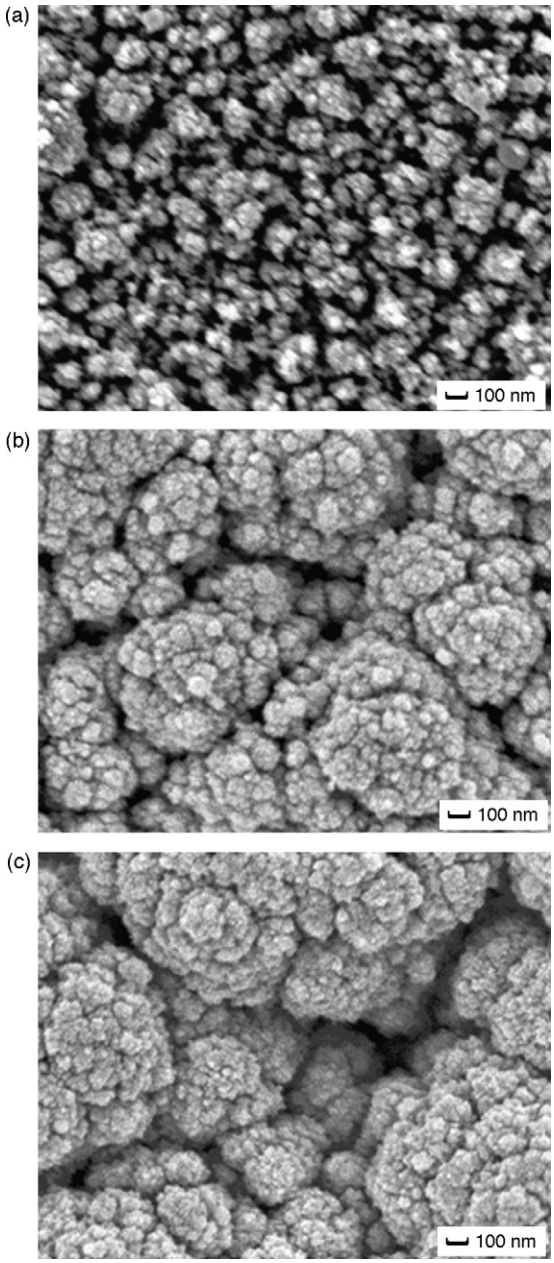

Fig. 10. SEM micrographs of the TiO_2 films annealed at 573 K, deposited for (a) 25 shots, (b) 100 shots and (c) 200 shots.

the basis of titania thin film. The cluster size is improved by further agglomeration owing to the successive ion bombardment (ion irradiation effect) and/or post-deposition annealing (thermal coagulation effect). Films grown at extremely slow rate contain atoms or molecules as growth units, whereas dimers, trimers, tetramers or large clusters are formed at faster growth rates. Since repetitive mode DPF-based thin film deposition is a fast process, the gas phase nuclei making a sufficiently large surface area facilitate the atomic growth preferentially on the clusters in gas phase rather than on the substrate surface. Moreover, the growth of larger clusters on successive ion bombardment by repetitive DPF shots is owing to the surface energy minimization of smaller clusters. The ion-induced collision cascades rapidly increase the total free energy of the film. The transition of metastable anatase phase to stable rutile phase requires the minimization of total free energy that is accomplished by the agglomeration of the nanoparticulates owing to the defects migration and redistribution within the film. This in turns develops larger surfaces, thus minimizing the surface-free energy, a major contribution to the total free energy. This supports the phase transformation of metastable anatase phase to stable rutile phase along with the crystallinity improvement as well.

Fig. 10 shows SEM micrographs of the TiO_2 films deposited for multiple number (25, 100 and 200) of shots to demonstrate the agglomeration effect by annealing at 573 K. It is well known that rapid heating of the films causes fast removal of residues from the material and the resulting TiO_2 films may appear porous. Moreover, such thin crystalline films are likely to be cracked due to the mismatch in the thermal expansion coefficients of the film and the substrate. However, a controlled temperature profile such as annealing in the present investigations, on the other hand, permits the slow release of such residues along with defects migration and a dense non-porous morphology of the film surface is reflected. The increased ion irradiation-based agglomeration of the nucleates is explained by the charged clustering during gas phase nucleation of titania (TCC) and ion-induced thermal coagulation of pre-deposited film by the preceding shots.

SEM micrographs collected for the TiO_2 films deposited for 25, 100 and 200 shots and all annealed at 773 K demonstrate that identical trends of cluster agglomeration have been found when the films deposited for different number of ion irradiation shots are post-annealed at further higher temperature. Higher temperatures favor the formation of larger nano-phase clusters.

4. Conclusions

Successful deposition of crystalline TiO_2 thin films onto silicon substrates at room temperature has been achieved using a repetitive plasma focus device. Films have been deposited using different number of focus deposition shots and have been post-annealed at different temperatures (573 K, 773 K and 973 K). The TiO_2 films are evolved with the anatase phase for lower number of ion exposure shots, which is transformed to the rutile phase along with the crystallinity improvement by increasing the ion exposure shots. The crystallite sizes of the TiO_2 particulates, estimated from typical (1 0 1) diffraction peak of rutile phase as-deposited for 50 and 75 shots, are found to be about 8 nm and 13 nm, respectively. The as-deposited films are found to have residual stresses typically varying from 13.2 GPa to 22.3 GPa for 50 to 200 focus shots, respectively, which saturate at higher number of ion irradiation shots of 150 and 200 shots. Annealing of the titania films has also resulted in anatase to rutile phase transformation along with the improvement of their crystallinity and relaxation of stress level. The oxygen vacancies introduced during the TiO_2 film deposition in the $Ar + O_2$ atmosphere as well as by the annealing of stoichiometric TiO_2 films in the reducing atmosphere of air ambient may help in the phase transformation from anatase to rutile. The weight fractions estimates reveal that W_{an} reduces as the number of ion exposure shots and/or annealing temperature increases, which confirms the anatase to rutile phase transformation. Raman investigations of the TiO_2 films have confirmed the presence of E_g and A_{1g} Raman active modes of rultile phase, which is favorably grown for higher ion exposure shots (150 and 200 shots) and is found to be stabilized at room temperature unlike conventional growth of this phase at higher temperature. Although, ion irradiation and annealing both improve the crystallinity of the TiO_2 films, the effect of ion irradiation is more gratifying for the growth of rutile than that of anatase. The annealing at low temperature transforms the anatase to rutile along with the overall crystallinity improvement of titania. But increasing the annealing temperature favorably grows rutile than anatase. SEM micrographs of the films exhibit the presence of nano-sized grains and their agglomeration by increasing the number of ion exposure shots and/or annealing temperature. The anatase to rutile phase transformation is accompanied by the further agglomerlation of nanoclusters of titania caused by the increasing energetic ion irradiation and/or annealing temperature. A systematic study of microstructure, crystallinity, phase composition and surface morphology of the TiO_2 films, based on ion irradiation and annealing temperature, is reported in order to understand the film deposition by the repetitive plasma focus device, post-deposition annealing and the transformation of anatase to rutile phase qualitatively and quantitatively at the temperature below the transition temperature reported in Powder Diffraction data.

Acknowledgement

The present work is supported by the research grant AcRF grant RP 3/06 RSR, National Institute of Education (NIE), Nanyang Technological University, Singapore.

References

[1] N. Huang, Y.R. Chen, J.M. Luo, J. Yi, R. Lu, J. Xiao, Z.N. Xue, X.H. Liu, J. Biomater. Appl. 8 (1994) 404.
[2] N. Xu, Z. Shi, Y. Fan, J. Dong, J. Shi, C. Hu, Ind. Eng. Chem. Res. 38 (1999) 373.
[3] C.C. Wang, Z. Zhang, J.Y. Ying, Nanostruct. Mater. 9 (1997) 583.
[4] B.S. Richards, J.E. Cotter, C.B. Honsberg, S.R. Wenham, Conference Record of the Twenty-Eighth IEEE Photovoltaic Specialists Conference 2000 (Cat. No. 00CH37036) (2000) 375.
[5] D. Mardare, M. Tascab, M. Delibasa, G.I. Rusu, Appl. Surf. Sci. 156 (2000) 200.
[6] P. Löbl, M. Huppertz, D. Mergel, Thin Solid Films 251 (1994) 72.
[7] K. Vydianathan, G. Nuesca, G. Peterson, E.T. Eisenbraun, A.E. Kaloyeros, J.J. Sullivan, B. Han, J. Mater. Res. 16 (2001) 1838.
[8] W.X. Xu, S. Zhu, X.C. Fu, Appl. Surf. Sci. 136 (1998) 194.
[9] S. Zhang, Y.F. Zhu, D.E. Brodie, Thin Solid Films 213 (1992) 265.
[10] D. Mardare, A. Stancu, Mater. Res. Bull. 35 (2000) 2017.
[11] A. Rothschild, F. Edelman, Y. Komem, F. Cosandey, Sens. Actuators B: Chem. 67 (2000) 282.
[12] S.K. Zheng, T.M. Wang, G. Xiang, C. Wang, Vacuum 62 (2001) 361.
[13] L.L.W. Chow, M.M.F. Yuen, P.C.H. Chan, A.T. Cheung, Sens. Actuators B: Chem. 76 (2001) 310.
[14] K. Okimura, N. Maeda, A. Shibata, Thin Solid Films 281–282 (1996) 427.
[15] M.C. Barnes, S. Kumar, L. Green, N.M. Hwang, A.R. Gerson, Surf. Coat. Technol. 190 (2005) 321.
[16] S. Lee, T.Y. Tou, S.P. Moo, M.A. Eissa, A.V. Gholap, K.W. Kwek, S. Mulyodrono, A.J. Smith, W. Suryadi, Usada M. Zakaullah, Am. J. Phys. 56 (1988) 62.
[17] S. Ahmad, M. Sadiq, S. Hussain, M. Shafiq, M. Zakaullah, A. Waheed, Rev. Sci. Instrum. 77 (2006) 013504–13508.
[18] H. Bhuyan, M. Favre, E. Valderrama, H. Chuaqui, E. Wyndham, J. Phys. D: Appl. Phys. 39 (2006) 3596.
[19] S. Ahmad, S.S. Hussain, M. Sadiq, M. Shafiq, A. Waheed, M. Zakaullah, Plasma Phys. Control Fusion 48 (2006) 745.
[20] S. Lee, P. Lee, G. Zhang, A. Serban, M. Liu, X. Feng, S.V. Springham, C. Selvam, V. Kudryashov, T.K.S. Wong, Sing., J. Phys. 14 (1998) 1.
[21] R.S. Rawat, M.P. Srivastava, S. Tandon, A. Mansingh, Phys. Rev. B 47 (1993) 4858.
[22] R. Sagar, M.P. Srivastava, Phys. Lett. A 183 (1993) 209.
[23] P. Agarwal, S. Annapoorni, M.P. Srivastava, R.S. Rawat, P. Chauhan, Phys. Lett. A 231 (1997) 434.

[24] M.P. Srivastava, S.R. Mohanty, S. Annapoorni, R.S. Rawat, Phys. Lett. A 215 (1996) 63.
[25] R.S. Rawat, P. Arun, A.G. Videshwar, Y.L. Lam, P. Lee, M.H. Liu, S. Lee, A.C.H. Huan, Mater. Res. Bull. 35 (2000) 477.
[26] R.S. Rawat, P. Arun, A.G. Videshwar, P. Lee, S. Lee, J. Appl. Phys. 95 (2004) 7725.
[27] T.K. Borthakur, A. Sahu, S.R. Mohanty, B.B. Nayak, B.S. Acharya, Surf. Eng. 15 (1999) 55.
[28] R. Gupta, M.P. Srivastava, Plasma Sources Sci. Technol. 13 (2004) 371.
[29] C.R. Kant, M.P. Srivastava, R.S. Rawat, Phys. Lett. A 226 (1997) 212.
[30] J. Fink, T.M. Heinzerling, J. Pfluger, B. Scheerer, B. Dichler, P. Koidl, Phys. Rev. B 30 (1984) 4713.
[31] C.R. Kant, M.P. Srivastava, R.S. Rawat, Phys. Lett. A 239 (1998) 109.
[32] R.S. Rawat, P. Lee, T. White, L. Ling, S. Lee, Surf. Coat. Technol. 138 (2001) 159.
[33] R.S. Rawat, W.M. Chew, P. Lee, T. White, S. Lee, Surf. Coat. Technol. 173 (2003) 276.
[34] M. Hassan, A. Qayyum, R. Ahmad, G. Murtaza, M. Zakaullah, J. Phys. D: Appl. Phys. 40 (2007) 769.
[35] K. Takao, T. Honda, I. Kitamura, K. Masugata, Plasma Sources Sci. Technol. 12 (2003) 407.
[36] W. Kies, G. Decker, U. Berntien, Yu.V. Sidelnikov, D.A. Glushkov, K.N. Koshelev, D.M. Simanovskii, S.V. Babashev, Plasma Sources Sci. Technol. 9 (2000) 279.
[37] M.J. Rhee, Appl. Phys. Lett. 37 (10) (1980) 906.
[38] R. Ahmad, M. Hassan, G. Murtaza, J.I. Akhter, A. Qayyum, A. Waheed, M. Zakaullah, Radiat. Effects Defects Solids 161 (2) (2006) 121.
[39] M. Hassan, R.S. Rawat, P. Lee, S.M. Hassan, A. Qayyum, R. Ahmad, G. Murtaza, M. Zakaullah, Appl. Phys. A 90 (2008) 669.
[40] H. Tang, K. Prasad, R. Sanjines, P.E. Schmid, F. Levy, J. Appl. Phys. 75 (4) (1994) 2042.
[41] M. Schuisky, A. Harsta, A. Aidla, K. Kukli, A.A. Kiisler, J. Aarik, J. Electrochem. Soc. 147 (2000) 3319.
[42] R.D. Shannon, J.A. Pask, J. Am. Ceram. Soc. 48 (1965) 391.
[43] B.D. Cullity, S.R. Stock, Elements of X-ray Diffraction, Addison-Wesley Publishing Company, Reading, MA, 1978.
[44] R.A. Spurr, H. Myers, Anal. Chem. 29 (1957) 760.
[45] M.C. Barnes, D.Y. Kim, H.S. Ahn, C.O. Lee, N.M. Hwang, J. Cryst. Growth 213 (2000) 83.
[46] I.D. Jeon, C.J. Park, D.Y. Kim, N.M. Hwang, J. Cryst. Growth 223 (2001) 6.